Optimization of a 50 MHz Frequency Modulated Continuous Wave Radar System for the study of auroral E-region coherent backscatter

A Thesis Submitted to the
College of Graduate Studies and Research
in Partial Fulfillment of the Requirements
for the degree of Master of Science
in the Department of Physics and Engineering Physics
University of Saskatchewan
Saskatoon

By
Gareth William Perry

Permission to Use

In presenting this thesis in partial fulfilment of the requirements for a Postgraduate degree from the University of Saskatchewan, I agree that the Libraries of this University may make it freely available for inspection. I further agree that permission for copying of this thesis in any manner, in whole or in part, for scholarly purposes may be granted by the professor or professors who supervised my thesis work or, in their absence, by the Head of the Department or the Dean of the College in which my thesis work was done. It is understood that any copying or publication or use of this thesis or parts thereof for financial gain shall not be allowed without my written permission. It is also understood that due recognition shall be given to me and to the University of Saskatchewan in any scholarly use which may be made of any material in my thesis.

Requests for permission to copy or to make other use of material in this thesis in whole or part should be addressed to:

Head of the Department of Physics and Engineering Physics
116 Science Place
University of Saskatchewan
Saskatoon, Saskatchewan
Canada
S7N 5E2

Abstract

A 50 MHz Frequency Modulated Continuous Wave (FMCW) radar system, developed at the University of Saskatchewan to provide improved spatial and temporal resolution measurements of auroral E-region plasma processes, introduces ambiguous spectral information, due to spectral ghosting, for scattering events in which multiple radar echoes are detected. This thesis identifies two Linearly Frequency Modulated (LFM) radar waveforms used by the FMCW system as the source of the ghosting. An analysis procedure designed to counteract the spectral ghosting problem is developed but is not an ideal solution, and therefore replacement of the LFM waveforms is recommended.

A detailed investigation of alternative radar waveforms using the Ambiguity Function and Ambiguity Diagram techniques is performed. A frequency coded continuous wave radar waveform based on a composite Costas sequence is proposed as a successor to the LFM waveforms. The composite Costas radar waveform will conserve the spatial and temporal resolutions extended by the LFM waveforms and preclude any spectral ghosting. Implementing the proposed radar waveform and avoiding receiver saturation issues with the mono-static FMCW radar system in which both the transmitting and receiving antenna arrays are simultaneously and continuously active and geographically co-located is also discussed.

In addition to this, two 50 MHz backscatter events are presented in this thesis to demonstrate the effectiveness of the FMCW system, notwithstanding the spectral ghosting complication. The first event from November 21, 2009 is identified as a Type 1 instability and the second from September 13, 2009 is identified as a Type 2 instability which lasted for $\sim$ 16 minutes. Linear plasma fluid theory is used to provide a brief interpretation of both scattering events.

Acknowledgements

I would like to thank my supervisor Dr. Glenn Hussey for providing me with the opportunity to work on this project. His insight, patience and guidance are truly appreciated. I would also like to acknowledge the members of my advisory committee: Dr. Tom Steele, Dr. Kathryn McWilliams, Dr. Adam Bourassa and Dr. Eric Salt. I am grateful for the financial support received from the Natural Sciences and Engineering Research Council of Canada (NSERC), the Canadian Space Agency (CSA) and both the Department of Physics and Engineering Physics and the Institute of Space and Atmospheric Studies (ISAS) at the University of Saskatchewan.

Special thanks to Jan Wiid for his efforts with the FMCW system. Further thanks to Bill Marshall, Brad Krug, Elise Normand, Marian Thorpe, Jeremy Tran and Joel Cooper for all of their help. Thanks to Dennis and Solange Bakker for their regular site check-ups. Also, thanks to whoever shot three bullets through the FMCW radar shed. You added an edge of danger to my project.

Dr. George Sofko deserves thanks for his enlightening conversations, Dr. Jean-Pierre St. Maurice for his candor and to Dr. Pasha Ponomarenko, Dr. Chad Bryant and Dr. Dieter André for their useful discussions. I thank my fellow students, both graduate and undergraduate including Rob and Megan Gillies for their camaraderie as well as John McLeod and Robin Kleiv for their genuine friendship. I would also like to recognize Dr. Derek Harnett for encouraging me to pursue graduate studies and the staff at the University of the Fraser Valley, W.J. Mouat Secondary School and Centennial Park Elementary school in Abbotsford, B.C. for their commitment and hard-work.

To all of my friends in British Columbia and my extended family in England and Canada, I thank you for your love and confidence.

To Mom, Dad, Michael and Quinn. Words cannot describe your love, efforts and patience. To Janelle, my wind, my fire, my sunrise and my sunset.

For Mom, Dad, Michael and Quinn with love.

Contents

List of Tables

List of Figures

List of Abbreviations

AC	Alternating Current
ACF	Autocorrelation Function
AD	Ambiguity Diagram
AF	Ambiguity Function
AWG	Arbitrary Waveform Generator
B	Bandwidth
C_s	Ion-Acoustic Speed
CW	Continuous Wave
dB	Decibel
DC	Direct Current
DDS	Direct Digital Synthesis
FBI	Farley-Buneman Instability
FFT	Fast Fourier Transform
FM	Frequency Modulation
FMCW	Frequency Modulated Continuous Wave
GDI	Gradient Drift Instability
HF	High Frequency
IMF	Interplanetary Magnetic Field
I channel	In phase channel
L	Electron Density Gradient Scale Length
LFM	Linear Frequency Modulated
MRR	Manastash Ridge Radar
PRF	Pulse Repetition Frequency
Q channel	Quadrature phase channel
RAM	Random Access Memory
Rx	Received
SNR	Signal to Noise Ratio
SNR_A	Signal to Noise Ratio Amplitude
SNR_P	Signal to Noise Ratio Power
SuperDARN	Super Dual Auroral Radar Network
T	Waveform Duration
t_b	Pulse Duration
t_{bit}	Bit Length
Tx	Transmitted
UD	Uniqueness Duration
UT	Universal Time
V_D	Velocity Drift
V_{D_e}	Velocity Drift of the Electrons
V_{D_i}	Velocity Drift of the Ions
VHF	Very High Frequency

Chapter 1

Introduction

In this thesis, the optimization of a 50 MHz Frequency Modulated Continuous Wave (FMCW) radar system is presented. The FMCW system was developed at the University of Saskatchewan for the study of auroral E-region coherent backscatter. The radar system employed a novel technique that allowed it to simultaneously provide highly resolved spatial and temporal measurements of auroral processes. A by-product of the technique used was the introduction of ambiguous data in certain auroral backscatter events. This thesis outlines the origin of the ambiguous data and outlines a method of preventing it without degrading the overall performance of the system. Furthermore this thesis provides detailed examples of the capabilities and value of the FMCW system for the study of E-region coherent backscatter in its current configuration.

1.1 The Heliosphere

The heliosphere is the region of galactic space over which the magnetic field of the Sun can influence and interact. The magnetic field of the Sun interacts everywhere within the heliosphere, including with the Earth, via the Solar Wind. The Solar Wind is a high velocity outflow of highly energetic charged particles from the Sun composed of mainly electrons and protons and flows radially outward from the Sun at velocities in the range of 300 to 600 km/s.

The solar wind is a highly conducting plasma with an extremely low coefficient of magnetic diffusivity. This property allows the solar wind to carry the magnetic field

of the Sun, called the Interplanetary Magnetic Field (IMF), throughout the entire heliosphere. The low magnetic diffusivity of the solar wind prevents the magnetic field from evolving once it has been emitted from the Sun and because of this the IMF is sometimes described as being *frozen* into the solar wind [*Baumjohann and Treumann*, 1997].

1.2 The Magnetosphere

The magnetosphere is the volume of space over which the magnetic field of the Earth is dominant. Within the magnetosphere, only the magnetic field of the Earth is present and outside of the magnetosphere, only the IMF carried by the solar wind is present. The IMF is directly incident on the magnetosphere and, as such, interacts with the magnetic field of the Earth. One result of the IMF-magnetosphere interaction is the injection of high energy solar wind particles into the magnetosphere. These can travel down the magnetic field lines of the Earth and interact with the ionosphere of the Earth. This precipitation of particles into the ionosphere can result in collisions with the resident ionospheric particles and molecules, producing a large amount of optical photons known as the aurora.

The movement and interaction of charged particles within the magnetosphere produces numerous currents and electric fields which can couple down to and interact with currents and electrics fields within the ionosphere of the Earth [*Kivelson and Russell*, 1995; *Kelley*, 2009].

1.3 The Ionosphere

The ionosphere is a region of weakly ionized plasma (much less than 1% of gas is ionized) located approximately 80 to 1000 km above the surface of the Earth [*Kivelson and Russell*, 1995; *Kelley*, 2009]. Photoionization of the neutral atmosphere due to incident solar radiation is a major charged particle source for the ionospheric

plasma. The density distribution of various neutral atmospheric constituents, such as N_2 and O_2 creates multiple electron density peaks throughout the ionosphere. Three main electron density peaks are used to divide the ionosphere vertically into three main regions. The D region is located below 90 km. The E region is located between 90 and 150 km, the F region is located above 150 km. The E region has an electron density peak of $n_e = 10^5$ cm^{-3} at $\sim$ 110 km in altitude and the F region has an electron density peak of $n_e = 10^6$ cm^{-3} at $\sim$ 300 km in altitude [*Kivelson and Russell*, 1995]. The E region is of primary interest to this thesis.

1.3.1 E region

The plasma in the ionosphere is considered weakly ionized due to the relatively large collision frequency of the ions with the neutral atmosphere, ν_{in} [*Kelley*, 2009]. In both the E and F regions, the collision frequency of the electrons with the neutrals, ν_{en}, is much less than the gyrofrequency of the electrons, $\nu_{en} \ll \Omega_e$ ($\Omega_e = qB/m_e$ where q is charge, B is the magnetic field and m_e is the mass of the electron), and so the electrons are considered collisionless and magnetized. Note that in the F region both the electrons and ions are considered magnetized ($\nu_{in} \ll \Omega_i$ as well). In the E region, the ions are considered un-magnetized ($\nu_{in} \gg \Omega_i$), as their collision frequency with the ambient neutral atmosphere is much larger than their gyrofrequencies. In the F region the ions and electrons are equally mobile. In the E region, the ions are collisional and stationary with respect to the ambient neutral constituents, and the electrons are collisionless and highly mobile [*Kelley*, 2009].

In the ionosphere, the magnetic field of the Earth, **B**, and an electric field, **E**, are always present. The source of **E** differs for the various regions throughout the ionosphere; however, for the high-latitude auroral E region (which depending on geomagnetic activity, varies between 60° and 75° in geomagnetic latitudes), which is of primary interest for this research, **E** is mapped down from electric fields created from magnetospheric plasma flows [*Kelley*, 2009]. In the northern auroral regions, **B** is $\sim 10°$ from perpendicularity with respect to the surface of the Earth and directed

towards the center of the Earth, and $\mathbf{E}$ is nearly horizontal and directed equatorwards in the local morning hours (dawn) and polewards in the local evening hours (dusk).

The magnetic field of the Earth, $\mathbf{B}$, and the auroral electric field $\mathbf{E}$, combine to create an $\mathbf{E} \times \mathbf{B}$ drift (also referred to as the Hall drift) in the auroral region. The $\mathbf{E} \times \mathbf{B}$ drift is a fundamental drift for charged particles in the presence of an electric and magnetic field [*Baumjohann and Treumann*, 1997; *Chen*, 2006]. The drift velocity caused by the $\mathbf{E} \times \mathbf{B}$ drift, $\mathbf{V_D}$, is independent of charge, meaning both electrons and ions flow in the same direction, with a velocity equal to $\mathbf{V_D} = (\mathbf{E} \times \mathbf{B})/\mathrm{B}^2$. In the F region the electrons and ions flow in the $\mathbf{V_D}$ direction; however, in the E region, only the electrons flow in the $\mathbf{V_D}$ direction. In the E region the ions are highly collisional with the neutral atmosphere and thus are effectively stationary. The ions do drift along $\mathbf{E}$, but this is small compared to the $\mathbf{E} \times \mathbf{B}$ drift. In contrast, the electrons are highly mobile and $\mathbf{E} \times \mathbf{B}$ drifting. In the E region of the ionosphere a large current exists due to the large flow of electrons and is directed opposite of $\mathbf{V_D}$. This E-region current, due to the $\mathbf{E} \times \mathbf{B}$ drift, is referred to as the electrojet and in the auroral region it is called the auroral electrojet current. In the local morning hours (dawn) the electrojet current is directed geographically westward (electrons flowing eastward) while the opposite occurs in the local evening (dusk) hours.

The plasma in the auroral E region is highly dynamic due to the presence of the auroral electrojet. The plasma is subject to plasma instabilities due to the almost ever present density gradients, drifts, and turbulence due to geomagnetic activity. Past radar experiments have measured ionospheric plasma instabilities with wavelengths on the order of $\sim$ 0.1 to $\sim$ 30 m traveling with phase velocities of anywhere between 0 to $\sim$ 1 km/s [*Fejer and Kelley*, 1980; *Schlegel*, 1996]. Of interest to this thesis are auroral E-region instabilities which have a wavelength of $\sim$ 3 m (which corresponds to a 50 MHz radar frequency) with phase velocities in the range of 0 to $\sim$ 1 km/s.

Two primary tools are used for the study of E-region plasma instabilities: rockets and radar. Rockets are *in situ*, meaning they directly measure plasma parameters

and instabilities in the E region. This is a valuable asset; however, rockets can only be present in the E-region for a short amount of time. The second tool for measurement is radar, which uses backscatter techniques to measure plasma processes remotely. There are two categories of radar systems: incoherent scatter and coherent scatter. Incoherent scatter radar uses a Thomson backscattering technique and requires large and complex facilities [*Kelley*, 1989]. There are only a handful of incoherent scatter radar systems located throughout the world. Coherent backscatter radar systems employ Bragg scattering techniques, and compared to their incoherent counterparts, are commonly found throughout the world and require relatively small and basic facilities [*Kelley*, 1989]. Coherent backscatter is the primary focus of this research.

1.4 Coherent Backscatter Radar

Coherent backscattering systems scatter radar waves off of density irregularities attributed to plasma instabilities in the E region. This process is described by a conservation of momentum argument [*Fejer and Kelley*, 1980; *Schlegel*, 1996]:

$$\hbar\mathbf{k_t} = \hbar\mathbf{k_s} + \hbar\mathbf{k_m}, \tag{1.1}$$

where $\hbar = h/2\pi$ and h is Planck's constant, $\mathbf{k_t}$ is the transmitted radar wavevector, $\mathbf{k_s}$ is the scattered wavevector, and $\mathbf{k_m}$ is the wavevector of the plasma wave in the medium. In the case of direct backscatter (where the transmitting (Tx) and receiving (Rx) antennas are co-located) $\mathbf{k_t}$ = -$\mathbf{k_s}$ so:

$$2\mathbf{k_t} = \mathbf{k_m}, \tag{1.2}$$

which is equivalent to

$$\lambda_m = \frac{\lambda_t}{2}, \tag{1.3}$$

where λ_m is the wavelength of the instability in the medium and λ_t is the wavelength of the transmitted radar signal. Equation 1.3 is equivalent to the Bragg scattering

condition [*Schlegel*, 1996] and states an incident radar waveform will coherently backscatter off of density irregularities which have a wavelength that is half that of the detecting radar waveform. In this research, a radar with approximately a 50 MHz carrier frequency, a VHF (Very High Frequency) frequency, is used as a probing tool to investigate the auroral E-region. This equates to a radar wavelength of 6 m, which, according to the Bragg condition (Equation 1.3), corresponds to plasma instabilities with a 3 m wavelength.

1.4.1 Radar Types

Radars used for atmospheric and ionospheric investigations are divided in two categories: pulsed and continuous wave (CW). A pulsed radar system repetitively transmits a radar waveform that is discrete in time, known as a pulse. A CW radar system employs a long continuous radar waveform, which is not discrete in time.

Pulse Radar Systems

A pulsed radar system transmits a discrete and short length radar waveform repetitively. The duration of the discrete pulse determines the range resolution of the radar system [*Skolnik*, 1980]. A pulsed radar system can provide better range resolution by merely shortening the length of its pulse. This is beneficial for E-region measurements as E-region plasma processes have been shown to have structure at small scale lengths and require high spatial resolution for observation. However, E-region processes are also dynamic temporally and thus require a high temporal resolution and velocity resolution. In general, pulsed radar systems do not provide adequate temporal resolution for short time scale studies due the discrete nature (and lack of continuity) of their transmitted waveform. Examples of pulsed radar systems used for E-region observations include the Scandinavian Twin Auroral Radar Experiment (STARE) [*Greenwald et al.*, 1978], the Super Dual Auroral Radar Network (SuperDARN) [*Greenwald et al.*, 1995], and the Cornell University Portable Radar Interferometer (CUPRI) radar [*Sahr et al.*, 1991].

Continuous Wave Radar Systems

A continuous wave (CW) radar system transmits a continuous and un-interrupted radar waveform. The CW waveform is typically transmitted at a constant carrier frequency and therefore does not display any waveform characteristics that could be used to measure a range [*Levanon and Mozeson*, 2004a]. Accordingly, CW radar waveforms with a constant carrier frequency can not provide any range information for a backscatter event. On the other hand, due to their un-interrupted signal, CW radar systems are able to provide excellent temporal and velocity resolutions that are far superior to that of a pulsed radar system. Examples of CW radar system that have been used for E-region observations include the Saskatchewan Auroral Polarimetric Phased Array Ionospheric Radar Experiment (SAPPHIRE) [*Koehler et al.*, 1995] and the Sporadic E Scatter Experiment (SESCAT) [*Haldoupis and Schlegel*, 1993].

A trade-off does exist between spatial and temporal resolutions provided by pulsed and CW radar systems, respectively. For an experiment which requires high spatial resolution, a pulsed system must be used; however, for an experiment which requires high temporal resolution, a CW system must be used. Coherent radar systems used for E-region studies have been unable to provide high spatial and temporal resolutions simultaneously. However, a Frequency Modulated Continuous Wave (FMCW) radar system, developed at the University of Saskatchewan [*Cooper*, 2006], was able to overcome the trade-off and provide both the high spatial and high temporal resolutions simultaneously.

1.4.2 FMCW Radar System

The FMCW radar system was developed at the University of Saskatchewan and is located just outside of Saskatoon, Saskatchewan, Canada. Whereas a basic CW (or pulsed) system transmits a CW (or discrete) waveform at a constant carrier frequency, the FMCW system varies its carrier frequency linearly over a frequency

FMCW radar parameters		
Parameter	Value	Units
Tx frequency	49.420-49.580	MHz
Tx wavelength	6.0466-6.0662	m
Waveforum duration	213	ms
Frequency resolution	4.69	Hz
Maximum range	993	km
Range resolution	970	m
Velocity resolution	14.1	m/s
Beam direction	7.25	$^\circ$ east of geographic north
Beam width	4.25	$^\circ$
Tx power	~ 50	W

Table 1.1: Table of parameters for the FMCW radar. This table is a modified version of one by *Cooper* [2006].

bandwidth. The linear frequency variation enables the system to provide high resolution range information along with high temporal resolution. The FMCW radar system could provide the high spatial resolution of a pulsed system and the high temporal resolution of a CW system simultaneously. Some parameters of the FMCW system are provided in Table 1.1. A diagram showing the field-of-view of the FMCW system is provided in Figure 1.1. The FMCW radar beam was directed slightly east of geographic north [*Hussey*, 1994]; however, as the magnetic contours in Figure 1.1 indicate, the beam was directed west of magnetic north.

The FMCW system was able to provide a range resolution of 970 m with a frequency resolution of 4.69 Hz and a velocity resolution of 14.1 m/s with an integration time of 5 s.

The FMCW system used a Direct Digital Synthesizer (DDS) card [*Analog Devices*, 2009] to produce a Linear Frequency Modulated (LFM) waveform for trans-

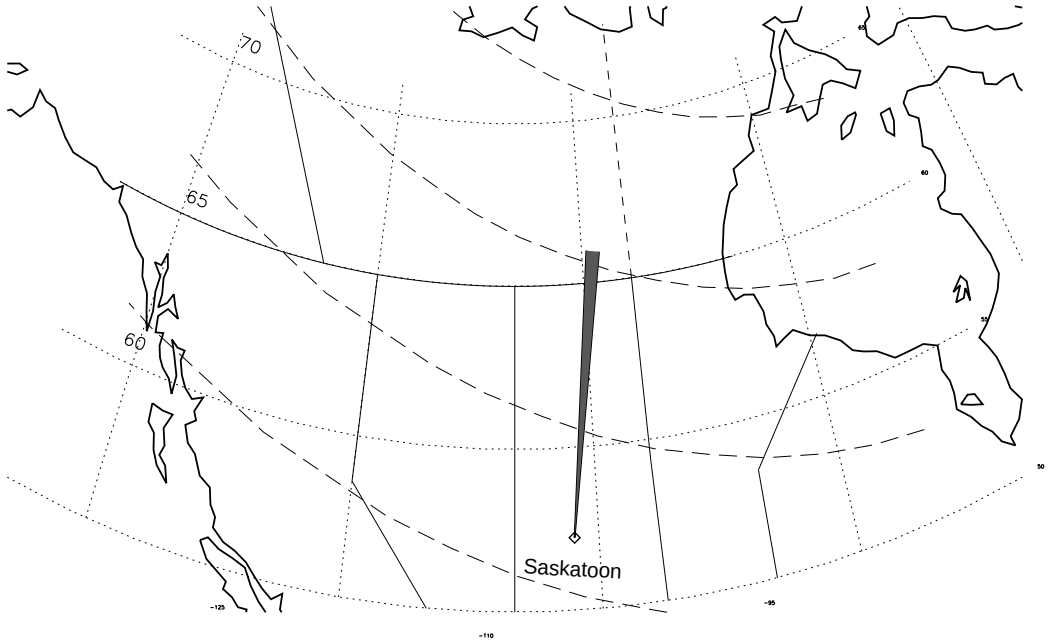

Figure 1.1: FMCW radar field-of-view with magnetic contours of 60°, 65° and 70°.

mitting. The LFM waveform, which is a CW waveform with a linearly varying carrier frequency, was amplified and transmitted from four Yagi antennas [*Cushcraft*, 1991]. In the initial development stages the system transmitted at a power of 1 kW; however, due to hardware complications with the final amplifier stage, which had to be removed, the FMCW began broadcasting at a reduced power of $\sim$ 50 W in June 2008. The backscatter signal was received by an additional four Yagi antennas which were located at the same geographic site as the Tx antennas. Due to the co-location of the Tx and Rx antennas, the FMCW system is considered a mono-static radar system. The entire FMCW radar array consists of 12 Yagi antennas on 15 m masts arranged in a long baseline. The first and last four antennas are Tx and Rx antennas while the middle four antennas are disconnected and used as a buffer to provide isolation between the Tx and Rx antennas.

The FMCW radar system is operated from 00:00 to 12:00 universal time (UT), which is 18:00 to 06:00 local lime (LT), daily. The data are recorded on a computer, compressed and then transmitted to the University of Saskatchewan via remote in-

ternet connection provided by Vecima Networks Inc. of Saskatoon [*Vecima*]. Once at the University of Saskatchewan the data are backed up onto DVD discs and then analyzed.

1.5 Thesis Layout

The FMCW radar system was shown to be effective at providing high spatial and temporal resolution radar measurements for E-region plasma instabilities [*Cooper*, 2006]. However, the auroral E region is highly dynamic and the FMCW system encountered difficulty providing correct range and velocity information for a number of events when multiple plasma instabilities were observed at the same time. When multiple instabilities were observed, additional and irrelevant range and velocity information was produced by the analysis procedures, which was difficult to differentiate from actual radar data. This effect was termed spectral ghosting and radar events in which spectral ghosting occurred were a common occurrence. The purpose of this thesis is to identify the main cause of the spectral ghosting problem and to resolve it. Furthermore, another motivation for this research is to demonstrate the effectiveness of the FMCW system as an auroral E-region coherent backscatter tool, notwithstanding the spectral ghosting difficulty.

Chapter 2 gives an introduction into radar waveform analysis. It introduces techniques used to investigate the resolution properties of radar waveforms. The Ambiguity Function (AF) and Ambiguity Diagram (AD), both of which describe the resolution properties in range and velocity for a given radar waveform, are defined. A square pulse and linear frequency modulated (LFM) waveform are also examined with the AF and AD descriptions. A more detailed description of techniques employed by the FMCW system is provided, and the cause of the spectral ghosting problem, identified as a data association problem, is introduced.

Chapter 3 presents a first solution to the spectral ghosting problem. An analysis technique known as the Peak-Finder Solution is described in detail. Chapter 3

concludes by suggesting that a new radar waveform is required by the FMCW system to avoid the data association, and thus the spectral ghosting, problem.

In Chapter 4, different types of radar waveforms are investigated for replacing the waveform used by the FMCW system. Waveforms based on pulse-repetition frequency (PRF) staggering, phase coding and frequency coding are examined using the AFs and ADs of the respective waveforms. A candidate waveform, based on an ideal frequency hopping sequence known as a composite Costas sequence, is identified as a suitable waveform. The feasibility and requirements for implementing the candidate waveform on the FMCW system are also explored. A result of the waveform research describes a novel concept proposal for a continuously active radar system, which can Tx and Rx the composite Costas waveform using a mono-static radar system.

Chapter 5 presents some radar events observed by the FMCW radar system (as it is currently implemented). The basic E-region plasma instabilities are characterized, and linear plasma fluid theory is used to analyze some auroral E-region radar observations.

Chapter 6 provides a summary of the project and suggestions for future work with the FMCW system. Future work is considered for two possible routes for the FMCW system: one involving the immediate implementation of the new composite Costas radar waveform outlined in Chapter 4 and one without.

Chapter 2

Radar Signals and the FMCW Radar

In this chapter, a description of basic radar signal analysis is given. A radar signal analysis formulation, the Ambiguity Function, is outlined along with its graphical representation, the Ambiguity Diagram. A constant frequency pulse radar waveform and Linear Frequency Modulated (LFM) radar waveform are introduced and examined using the Ambiguity Functions and Diagrams. Furthermore, a detailed description of the FMCW system and signal analysis procedure is provided along with brief explanations of the SuperDARN radar [*Greenwald et al.*, 1995] and the Manastash Ridge Radar [*Lind*, 1999] analysis procedures.

2.1 Matched Filter

The operation of a basic radar system is straight forward: transmit a known signal, receive a reflected signal, and then compare the two signals to determine basic parameters about the radar reflector, or radar target. This process is composed of complicated tasks. Specifically, a method is required for determining whether a Rx signal is a reflected signal, or simply irrelevant random noise. Also, a technique for comparing a Rx signal to a Tx signal, for detecting relevant target information, is needed. As it turns out, both tasks can be accomplished simultaneously with what is known as the *matched filter* technique. A description of this is presented in this and the next section and is based on *Levanon and Mozeson* [2004a].

Signals incident on a radar receiver can be classified into two categories. The first category is *relevant signal*. Relevant signal is any signal which originates from

the Tx antenna, propagates to a radar target, scatters off of a radar target and then propagates back towards the Rx antenna. The second category is noise. Noise is any signal that originates from anywhere but the Tx antenna. Noise is further classified into systematic and random noise and is signal that provides no relevant information for the radar scattering event. A source of systematic noise is the commercial power grid, whereas sky noise from cosmic radiation is a source of random noise [*Cooper*, 2006]. One of the basic tasks of a radar is to separate the relevant signal from the noise signal. To describe this process, a basic definition of a radar signal is first required.

A radar signal $s(t)$ may be defined by [*Levanon and Mozeson*, 2004a]:

$$s(t) = g(t)\cos(\omega_c t + \phi(t)), \tag{2.1}$$

where $g(t)$ is the envelope of the signal, ω_c is the carrier frequency, $\phi(t)$ is the phase and t is time. Various representations of Equation 2.1 exist; however, for the FMCW system, and for modern radars which use digital analysis techniques, a basic signal is given as complex valued,

$$s(t) = \Re\{u(t)\exp(j\omega_c t)\}, \tag{2.2}$$

or

$$s(t) = \frac{1}{2}u(t)\exp(j\omega_c t) + \frac{1}{2}u^*(t)\exp(-j\omega_c t) \tag{2.3}$$

where

$$u(t) = g_c(t) + jg_s(t), \tag{2.4}$$

and

$$g_c(t) = g(t)\cos(\phi(t)), \tag{2.5}$$

$$g_s(t) = g(t)\sin(\phi(t)). \tag{2.6}$$

In the above equations, $u(t)$ is the complex envelope, $u^*(t)$ is the complex conjugate of the complex envelope, j is $\sqrt{-1}$, $g_c(t)$ is the in-phase component and $g_s(t)$ is the quadrature component. The in-phase and quadrature components are referred to as the I and Q components respectively.

Relevant signal and noise are continuously and simultaneously received by a radar system, and so the relevant signal must be detected amongst the noise. The first step in the detection of a relevant signal is filtering. A filter is applied to the Rx signal to suppress the irrelevant noise signal and allow any relevant signal to pass through. A filter that is the most effective at suppressing the noise, and thus maximizing the signal-to-noise-ratio is known as a *matched filter* [*Levanon and Mozeson*, 2004a; *Skolnik*, 1980; *Rihaczek*, 1969]. For a radar system, the impulse response of a matched filter is a modified copy of transmitted radar signal, which is described by [*Levanon and Mozeson*, 2004a],

$$ACF_s(t) = \int_{-\infty}^{\infty} s(\tau)s^*(\tau + t)\, d\tau, \tag{2.7}$$

which is the autocorrelation function (ACF), where $s(\tau)$ is the signal as defined in Equation 2.2 and $s^*(\tau)$ is the complex conjugate. The purpose of the ACF in Equation 2.7 is to evaluate the area under the product of a function, $s(\tau)$, with itself offset by t, $s(\tau + t)$ [*Brigham*, 1988]. The complex conjugate is present in Equation 2.7 due to the requirement that the output of a matched filter must be an amplitude and therefore real valued. The value of the ACF in Equation 2.7 will have a maximum when the area under the product of two functions, $s(\tau)$ and $s(\tau+t)$, is at a maximum. This only occurs at the offset, t, at which the two functions are exactly overlaid. The ACF is used as a signal analysis tool since it is used to determine the amount of temporal offset between two identical signals. This can be applied to radar analysis where the offset between two identical radar signals, t, is a measure of the delay between two signals due to the radar signal propagation and therefore range to a radar target. If there is no target present at a range corresponding to offset t, then Equation 2.7 at that range, ignoring noise, is zero.

In Equation 2.7, $s(t)$ can represent a received radar signal while $s^*(\tau + t)$ can be considered a transmitted radar signal. The Rx signal $s(t)$ is being matched to a copy of the Tx signal $s^*(\tau + t)$, a process described by the ACF in Equation 2.7. Mathematically, the terms could be defined in the opposite manner. Nonetheless, a convention is needed. Equation 2.7 provides an idea of how signal energy is dis-

tributed due to signal processing (described later). A radar scattering event, one in which a radar signal is transmitted, reflected and received, can therefore be described by Equation 2.7. Techniques employed by the FMCW radar system, the SuperDARN radar system and other radar systems can be described by Equation 2.7. Techniques used by the FMCW and SuperDARN radar systems are described in Sections 2.3 and 2.4, respectively.

For this research, all radar signals are considered to be narrow bandpass signals. A narrow bandpass signal is a signal that has the majority of its energy focused within close proximity to the carrier frequency ω_c. If Equation 2.3 is evaluated in Equation 2.7, the narrow bandpass signal assumption allows for terms in the evaluation of Equation 2.7, which correspond to signals whose carrier frequencies are outside the narrow bandwidth, to be neglected. From this, the expression for ACF_s is [*Levanon and Mozeson*, 2004a],

$$ACF_s(t) \approx \Re\{ACF_u(t)\exp(j\omega_c t)\}, \tag{2.8}$$

where

$$ACF_u(t) = \int_{-\infty}^{\infty} u(\tau)u^*(\tau + t)\ d\tau, \tag{2.9}$$

and the definitions of u, t and τ remain unchanged. Equation 2.8 represents the output of the matched filter of a radar system, for the narrow bandpass assumption. Like Equation 2.7, Equation 2.9 describes a radar scattering event. The difference between the two equations is that Equation 2.9 uses the narrow bandpass approximation and Equation 2.7 does not. In Equation 2.9 $u^*(\tau + t)$ may be considered the complex envelope of a Tx radar signal while $u(\tau)$ may represent the complex envelope of a Rx radar signal. Equation 2.8 is relevant to this research and the FMCW system as the matched filter was implemented in hardware in the FMCW radar system. The FMCW system mixed the Rx radar signal with the Tx radar signal in the time domain. This is equivalent to the procedure described in Equation 2.9 in the frequency domain where $u^*(\tau + t)$ is the transmitted FMCW signal and $u(t)$ is the received FMCW signal. Additional details into the implementation of the matched filter technique are described in Section 2.3.

Equation 2.8 indicates that the output of the matched filter is dependent on a time delay t which is equivalent to a propagation delay. Equation 2.9 can be used to calculate the range. However, it is also desirable to measure the radial velocity of a target via the Doppler effect. To account for this, Equation 2.9 is modified [*Levanon and Mozeson*, 2004a],

$$ACF_u(t,\nu) = \int_{-\infty}^{\infty} \exp(j2\pi\nu\tau)\, u(\tau)u^*(\tau+t)d\tau, \tag{2.10}$$

where ν is an arbitrary added frequency component to the complex envelope $u(t)$ (Equation 2.4) to represent a frequency shift due the Doppler effect (recall that $u(t)$ may be considered the received radar signal in a radar scattering event). With this modification, Equation 2.10 now accounts for the propagation delay due to the range of a radar target, t, as well as the Doppler frequency shift due to the radial velocity of the radar target, ν. Both the propagation delay and Doppler frequency shift are represented as a delay mismatch and frequency mismatch with the matched filter, respectively. To align with the traditional labeling of τ as an offset in time and t as time, their roles are reversed and Equation 2.10 is re-written [*Levanon and Mozeson*, 2004a],

$$|\chi(\tau,\nu)| = \left| \int_{-\infty}^{\infty} u(t)u^*(t+\tau)\exp(j2\pi\nu t)dt \right|, \tag{2.11}$$

which is called the Ambiguity Function (AF). The AF is a valuable tool in radar signal analysis and is the focus of the next section.

2.2 Ambiguity Function

The AF, as defined in Equation 2.11, is a valuable tool for radar signal analysis and is dependent on $u(t)$, which is the complex envelope of a radar signal as defined in Equation 2.4. Important radar waveform properties such as range resolution, the ability to resolve separate targets in range, Doppler frequency resolution and the ability to resolve separate targets in velocity space, are all described by $u(t)$ [*Levanon and Mozeson*, 2004a].

In a practical sense, the AF is a description of how far apart, in both range and velocity, any number of radar targets must be separated in order to be resolved by a given radar waveform. Certain waveforms provide better range resolution or velocity resolution than others and the ability of two radar waveforms to detect and measure the same multiple targets with varying range and velocity properties may be different, even if the range and frequency resolutions of both waveforms are equivalent. Provided within the AF, in Equation 2.11, are details of the parameters and performance characteristics of any radar waveform characterized by $u(t)$ and so the specifications and capabilities of any radar waveform can be investigated in detail.

The unit of Equation 2.11 is energy and so the AF is a description of the energy distribution of a radar scattering event both in the delay, τ, and Doppler frequency, ν, domains. The characteristics of a radar waveform described by $u(t)$ may be determined with the AF, which outlines where the energy of a radar event is distributed in delay and Doppler frequency space. Ideally, the energy of a radar event should be focused near areas in delay and Doppler frequency space which correspond to the location of the radar scatterer and not in other areas. The energy in an AF is referred to as clutter, self-clutter, ambiguity or ambiguity volume [*Levanon and Mozeson*, 2004a; *Rihaczek*, 1969].

2.2.1 Ambiguity Function Properties

The AF describes a matched filter response to a signal offset in range (τ) and Doppler frequency shift (ν), corresponding to a radar signal that has been scattered off of a radar target at some distance, corresponding to τ, and with some radial velocity corresponding to ν [*Levanon and Mozeson*, 2004a]. Within the AF is information on the capabilities of a given radar waveform defined by $u(t)$.

Autocorrelation Function

The ACF is recovered from Equation 2.11, if ν is set to $\nu = 0$ [*Levanon and Mozeson*, 2004a; *Rihaczek*, 1969],

$$|\chi(\tau, 0)| = \left| \int_{-\infty}^{\infty} u(t)u^*(t+\tau)dt \right|. \tag{2.12}$$

Here, setting $\nu = 0$ is the matched filter response corresponding to a radar target with some range but no radial velocity. Thus at $\nu = 0$, the AF is a function of the offset, τ, of the received signal matched to a copy of the transmitted signal. The offset τ, at which the AF is maximized, is the propagation delay for the return trip of the radar signal to the radar target, and therefore the range to target can be determined.

The delay resolution of a radar waveform is defined as the first null in Equation 2.12 [*Levanon and Mozeson*, 2004a]. The range resolution is the minimum distance that two radar targets must be separated to be resolved as individual targets by the radar waveform. This is similar to optics where resolution is governed by the clear separation of two objects of equal irradiance [*Hecht*, 2002]. The delay resolution of a radar waveform corresponds to the smallest delay, τ, which satisfies,

$$\left| \int_{-\infty}^{\infty} u(t)u^*(t+\tau)dt \right| = 0. \tag{2.13}$$

The range resolution of a radar system (defined shortly as half the delay resolution) is unique to the properties of the system. The range resolution of the Scandinavian Twin Auroral Radar Experiment (STARE) [*Greenwald et al.*, 1978] radar system was 20 km whereas the range resolution of the FMCW system [*Cooper*, 2006] used in this research was 970 m. The delay resolution of a radar system is controlled by varying properties of the transmitted radar waveform which will be discussed shortly.

Spectrum

If $\tau = 0$ in Equation 2.11,

$$|\chi(0, \nu)| = \left| \int_{-\infty}^{\infty} |u(t)|^2 \exp(j2\pi\nu t)dt \right|, \tag{2.14}$$

which is the magnitude of the Fourier transform, and thus the power spectrum of $|u(t)|^2$ [*Skolnik*, 1980].

The Doppler frequency resolution is the minimum separation of Doppler frequencies two radar targets must have before a radar waveform can resolve two targets as being separate in frequency space. The Doppler frequency resolution of a radar waveform, described by $u(t)$, is the smallest Doppler frequency shift, ν, which satisfies,

$$\left| \int_{-\infty}^{\infty} |u(t)|^2 \exp(j2\pi\nu t) dt \right| = 0. \tag{2.15}$$

Like delay resolution, Doppler frequency resolution is a function of waveform properties which will be discussed shortly. The Doppler velocity resolution is a function of the Doppler frequency resolution. The Doppler velocity resolution for the STARE radar system was 150 m/s [*Lind*, 1999], whereas the Doppler velocity resolution for the FMCW radar system was 14.1 m/s [*Cooper*, 2006].

Maximum Value

The AF is normalized to its maximum value which is located at the origin $|\chi(0,0)|$ [*Levanon and Mozeson*, 2004a; *Skolnik*, 1980; *Rihaczek*, 1969],

$$|\chi(\tau,\nu)| \leq |\chi(0,0)| = 1. \tag{2.16}$$

Conservation of Volume

The conservation of volume is shown as [*Levanon and Mozeson*, 2004a; *Skolnik*, 1980; *Rihaczek*, 1969],

$$\int_{-\infty}^{\infty} \int_{-\infty}^{\infty} |\chi(\tau,\nu)|^2 \, d\tau d\nu = 1. \tag{2.17}$$

This property states that the volume bounded by the AF surface is conserved and therefore energy is conserved. AF volume cannot be created or destroyed. If AF volume is eliminated from one region of delay and Doppler frequency space then it must re-appear elsewhere in delay and Doppler frequency space. Radar waveform design techniques which are discussed further in Chapter 4 seek to re-distribute the

AF volume (and thus energy) in delay and Doppler frequency space in a way that is optimal for the radar waveform applications.

2.2.2 Graphical Representations

The AF, ACF and spectrum of a radar signal can be described both analytically (Equation 2.11) and graphically. The plot of an AF is known as an Ambiguity Diagram (AD). In this thesis, the graphical representations of the AD, ACF and spectrum of all radar waveforms are created using a MATLAB routine provided by *Levanon and Mozeson* [2004a].

To demonstrate the properties of the graphical representations, a square pulse of duration T, with constant carrier frequency, ω_c, and constant amplitude is investigated. A constant frequency square pulse waveform is the most basic waveform and has been used by many radar systems including the Super Dual Auroral Radar Network (SuperDARN) radar system [*Greenwald et al.*, 1995] and the STARE radar system. These systems use complex sequences of constant frequency pulses and not simply a single pulse since the applications of a single pulse are limited for ionospheric research. Using a sequence of single pulses can extend the field-of-view of the radar system compared to using a single pulse without a sequence. Details of this are provided later in Chapter 4. The complex envelope of a square pulse is [*Levanon*, 1988; *Levanon and Mozeson*, 2004a],

$$u(t) = \frac{1}{\sqrt{T}}\text{rect}(\frac{t}{T})\exp(\frac{j2\pi t}{T}), \tag{2.18}$$

which is equivalent to

$$\frac{1}{\sqrt{T}}\text{rect}(\frac{t}{T}) = \begin{cases} 0 & \text{if } t < 0 \text{ or } t > T \\ \frac{1}{2\sqrt{T}} & \text{if } t = 0 \text{ or } t = T \\ \frac{1}{\sqrt{T}} & \text{if } 0 < t < T \end{cases}$$

where t is time and T is the pulse duration. The exponential term in Equation 2.18 is of the form $\exp(j2\pi f_c t)$ where f_c is the carrier frequency of the waveform. The

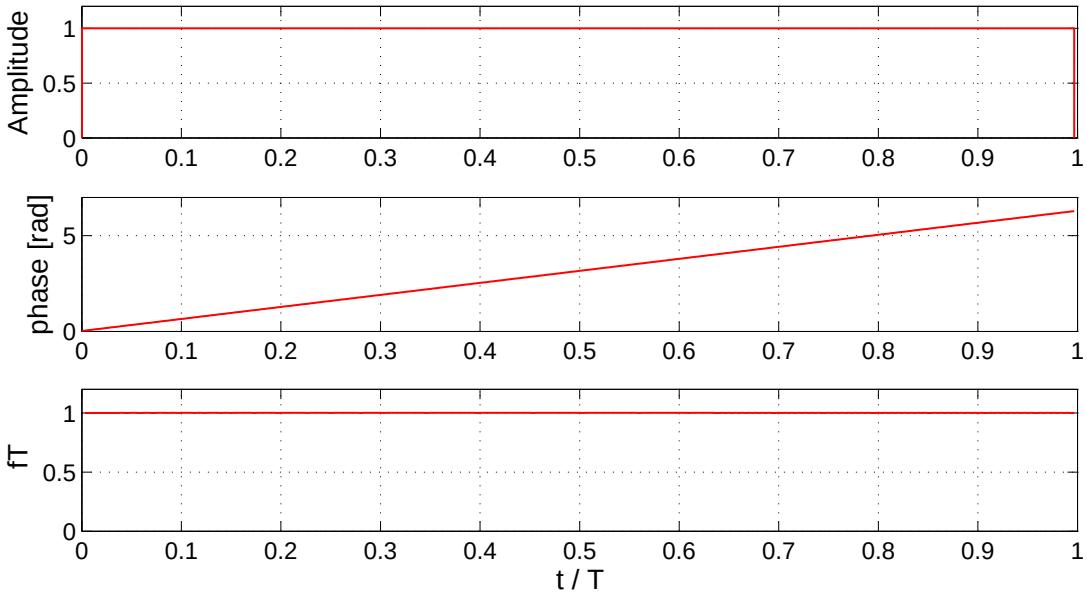

Figure 2.1: The amplitude (top), phase (middle) and frequency (bottom) as a function of t/T for a single constant amplitude pulse with a constant carrier frequency. Here, t is time and T is the waveform duration, which is equivalent to the pulse duration.

frequency of the square pulse described by Equation 2.18 is therefore $f_c = 1/T$. A plot of the amplitude, phase and frequency of the square pulse described in Equation 2.18 as a function of time is shown in Figure 2.1. The AD for a square pulse is plotted in Figure 2.2, along with the ACF and power spectrum in Figure 2.3.

In practice, radar systems do not use radar waveforms that consist of a single constant frequency pulse. Systems such as SuperDARN and STARE transmitted waveforms composed of combinations of constant frequency pulses, known as pulse sequences. Using pulse sequences allows for greater radar capabilities. Details of this are discussed in Chapter 4. Nonetheless investigating a single constant frequency pulse is a good introduction into the properties of radar waveforms.

In Figure 2.1, the vertical axes are in units of the respective parameters. The top plot in Figure 2.1 is a normalized value for amplitude while the middle plot is the phase of the pulse in radians. The vertical axis on the bottom plot represents frequency in units of fT (unitless) where f is the carrier frequency of the signal and

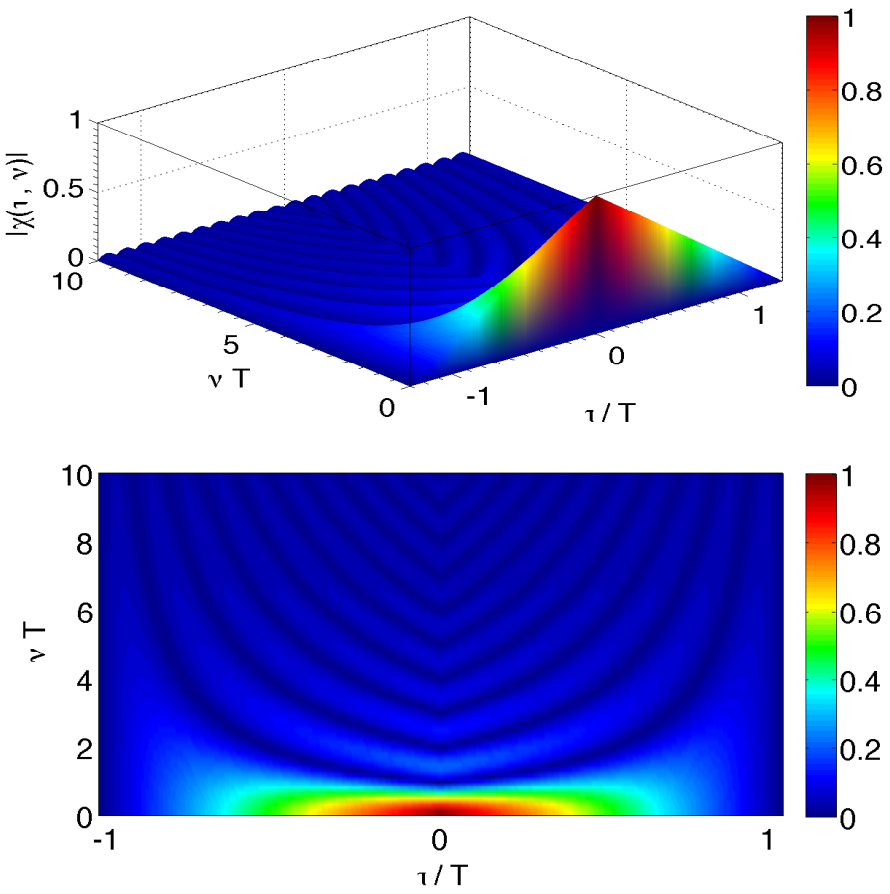

Figure 2.2: The AD for a constant amplitude and frequency square pulse. The bottom plot is an overhead view of the AD. The amplitude, phase and frequency of the pulse are plotted in Figure 2.1.

T is the pulse duration or waveform duration. For all three plots, the horizontal axis is in units of t/T where t is time and T is the waveform duration, which for a single pulse is equivalent to the pulse duration. The axes are equated in this way so that all constant amplitude and frequency square pulses can be described by Figure 2.1.

It is important to distinguish between the pulse duration and waveform duration. For this research, the pulse duration is labeled t_b and the waveform duration is labeled T. The pulse duration is the duration of a single pulse whereas the waveform duration T is the period of the overall radar waveform (which can be constructed of several pulses of duration t_b). In certain cases, such as a single pulse radar waveform, the

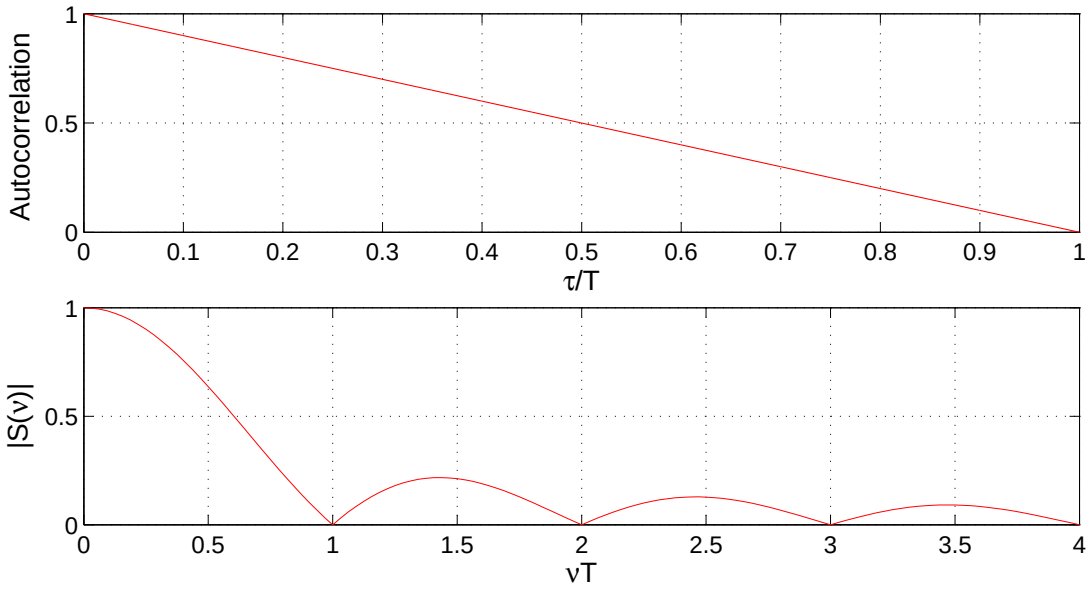

Figure 2.3: The spectrum (bottom) of a single square pulse with constant amplitude and frequency. The spectrum is a plot along the $|\chi(0,\nu)|$ cut of the AD in Figure 2.2. The top plot is the ACF $|\chi(\tau,0)|$.

pulse duration and waveform duration are equivalent.

In Figure 2.1, the amplitude (top plot) and frequency (bottom plot) are constant throughout the duration of the signal whereas the phase of the signal (middle plot) varies linearly. This is due to the linear variation of the phase as a function of time, which is required to describe a constant frequency, as frequency is a derivative of phase with respect to time. In this case, the $\phi(t)$ term in Equation 2.18 ($\exp(j2\pi t/T)$) is changing in order to keep the argument of the cosine term in Equation 2.1 constant while ω_c is constant and t is changing. In this thesis phase is generally not considered as an important parameter except for when it is manipulated in a radar waveform design technique known as phase coding which is discussed in Section 4.3.2.

The AD for the square pulse is plotted in Figure 2.2. An AD is a three-dimensional plot with the τ and ν axes outlining the $\tau-\nu$ plane; commonly referred to as the range-Doppler plane [*Levanon and Mozeson*, 2004a]. The τ axis is in units of τ/T, where τ is the propagation delay mismatch and therefore represents range, and T is the waveform duration. Along the ν axis, the units are νT, where ν is

the frequency mismatch corresponding to the Doppler frequency shift. The vertical axis is the normalized value of the AF. Generally, only two quadrants of an AF are displayed in the AD, due to the symmetry of the AF.

It is important to note that f and ν, τ and t are not equivalent; ν is the frequency mismatch between two signals in a matched filter, whereas f is the carrier frequency of a radar waveform while τ is the delay mismatch between two signals in a matched filter and t is simply time. In this thesis the length of the delay axis will be equivalent to time duration of the plotted radar waveform (the waveform duration, T) unless otherwise noted. The frequency axis length will be plotted to a maximum of ten frequency resolution cells (an arbitrarily chosen value).

An AD is useful since it visually describes the delay and frequency resolution of a radar waveform. The first null along the τ (Equation 2.13) and ν (Equation 2.14) axes, for all ADs correspond to the delay (range) and frequency (Doppler frequency shift) resolution of the plotted waveform, respectively. ADs are also useful in describing the performance of a radar waveform in a multiple radar target environment. Figure 2.2 is the matched filter response for a single radar target. To investigate the performance of the square pulse for multiple targets, one simply superposes copies of the plot in Figure 2.2 on a range-Doppler frequency plane [*Rihaczek*, 1969]. In this situation, targets with different ranges with respect to the radar system are separated along the τ axis while targets with different velocities are separated along the ν axis. Target resolvability, the ability to distinguish two targets separated by range and velocity, is then defined as the ability to distinguish the superposed AD plots [*Rihaczek*, 1969]. This is really a comparison of the energy distribution properties of different radar waveforms. When comparing different radar waveforms, the objective is to discern how the energy (or AD volume) is distributed in the $\tau - \nu$ plane with respect to the delay and frequency resolutions of the radar waveforms that are being compared.

Volume in an AD corresponds to the response of the matched filter due to a mismatch in delay, τ, and Doppler frequency shift, ν [*Levanon*, 1988; *Levanon and*

Mozeson, 2004a; *Rihaczek*, 1969]. In other words, volume in an AD outlines the resolution and energy distribution properties of a radar waveform. In Figure 2.2 the single peak volume centered at $|\chi(0,0)|$ represents the matched filter mismatch-free response to a single radar target. The ideal matched filter response is a Dirac delta spike at the origin, but is un-physical since it describes perfect delay and Doppler frequency resolution properties [*Levanon and Mozeson*, 2004a; *Skolnik*, 1980]. A delta spike at the origin would also violate the maximum AF value property described by Equation 2.16. The maximum value property restricts the height of the delta spike and since AF volume must be conserved according to Equation 2.17 the volume must appear elsewhere in delay and Doppler frequency space. The matched filter response is then altered by Equations 2.16 and 2.17 to what is referred to as the *thumbtack profile* [*Levanon*, 1988; *Levanon and Mozeson*, 2004a; *Rihaczek*, 1969; *Skolnik*, 1980]. In a thumbtack profile, AD volume is focused at the origin in a single spike, resembling a thumbtack and all other ambiguity volume on the range-Doppler plane is suppressed to near zero values. In the ideal Dirac delta spike at the origin, this property is indicative of an absence of aliasing or ambiguity in either the range or Doppler frequency domains. This demonstrates superior target resolution as well as resolvability on the $\tau - \nu$ plane. The thumbtack profile is as close as the ideal Dirac delta profile can be practically achieved. Therefore, a radar waveform which displays a thumbtack AD profile will have well suppressed range or velocity aliasing and should be able to resolve any number of multiple targets in any target configuration (on the $\tau - \nu$ plane) without difficulty.

From Equation 2.13, the first null along the τ axis corresponds to the delay resolution of the square pulse radar waveform. A plot of the AD along the τ axis is the ACF and is given in the top plot in Figure 2.3. Here, the vertical axis is the ACF value and the horizontal axis is in units of τ/T, where τ is the mismatch delay and T is the signal length (which for a single pulse waveform is equivalent to the pulse duration t_b). From the top plot in Figure 2.3, the first null occurs at $\tau = T$. This is referred to as the delay resolution of the waveform. The range resolution, ΔR, of

a constant frequency square pulse radar waveform is proportional to half the delay resolution, T [*Levanon and Mozeson*, 2004a; *Rihaczek*, 1969; *Skolnik*, 1980],

$$\Delta R = \frac{cT}{2}, \tag{2.19}$$

where c is the speed of light and T is the waveform duration. In general, ΔR is half the delay resolution of a radar waveform. Recall that for a single pulse, the pulse duration, t_b and waveform duration, T, are equivalent. The T in Equation 2.19 can be replaced with t_b. This does not hold for more complex waveforms composed of many pulses that are more appropriate for ionospheric studies than the single pulse waveform, however. In those cases the pulse duration, t_b, is much shorter than the waveform duration, T, but the range resolution is still described by the pulse duration t_b and Equation 2.19. For example, the SuperDARN radar system typically uses a pulse sequence comprised of a series of square, constant frequency and amplitude pulses. The waveform duration, T, is many milliseconds; however, each individual pulse duration is ~ 300 μs equating to a 45 km range resolution [*Greenwald et al.*, 1995].

Along the ν axis is the spectrum of the square pulse described by Equation 2.14 and it is plotted in the bottom plot in Figure 2.3. Here, the vertical axis is the normalized value of the power spectrum, denoted S, and the horizontal axis is in units of νT where ν is the Doppler frequency shift and T is the waveform duration. The spectrum forms the absolute value of the *sinc* function. This is expected since, from Equation 2.14, the Fourier transform of the magnitude of a square envelope is the absolute value of the *sinc* function by definition [*Brigham*, 1988]. The frequency resolution of the square pulse radar waveform is defined as the position of the first null along the ν axis (Equation 2.15) [*Levanon and Mozeson*, 2004a]. In Figure 2.3 the first null occurs at $\nu T = 1$, this can also be observed in the bottom plot in Figure 2.2. Thus, the frequency resolution of the square pulse is equivalent to,

$$\Delta f = \frac{1}{T}, \tag{2.20}$$

where Δf is the frequency resolution and T is the pulse duration. For pulse se-

quences, radar waveforms which are composed of several constant frequency pulses of duration t_b, Equation 2.20 still holds where T is the waveform duration of the pulse sequence (and not the pulse duration).

2.2.3 Linear Frequency Modulated Waveform

The Linear Frequency Modulated Waveform (LFM) is of particular interest as it is the waveform that was used by the FMCW radar system. An LFM waveform is constant in amplitude; however, the carrier frequency of the waveform varies linearly with time. The complex envelope of an LFM waveform is [*Levanon and Mozeson*, 2004a],

$$u(t) = \frac{1}{\sqrt{T}}\text{rect}(\frac{t}{T})\exp(j\pi\Gamma t^2), \tag{2.21}$$

which is equivalent to

$$\frac{1}{\sqrt{T}}\text{rect}(\frac{t}{T}) = \begin{cases} 0 & \text{if } t < 0 \text{ or } t > T \\ \frac{1}{2\sqrt{T}} & \text{if } t = 0 \text{ or } t = T \\ \frac{1}{\sqrt{T}} & \text{if } 0 < t < T \end{cases}$$

where t is time and, T is the LFM waveform duration. Γ is a constant equivalent to $\Gamma = \pm B/T$ where B is the bandwidth over which the carrier frequency varies. B is a positive number if the magnitude of the carrier frequency is increasing in time, referred to as an up-sweep, and a negative number if the frequency is decreasing in time, referred to as a down-sweep. The amplitude, frequency and phase as a function of time for an up-sweep LFM waveform are plotted in Figure 2.4. Here, the horizontal axes are a function of t/t_{bit} where t is time and t_{bit} is a bit length. A bit length is simply a small time portion of the overall waveform duration T. In this case of an LFM waveform, $t_{bit} = T/50$, a default value in the programming code provided by *Levanon and Mozeson* [2004a]. This value simply describes how many steps were used to construct the linear frequency variation. In signal generation, the linear frequency modulation is constructed from small steps, resembling a staircase. The digital generation hardware used by the FMCW system constructed an LFM signal

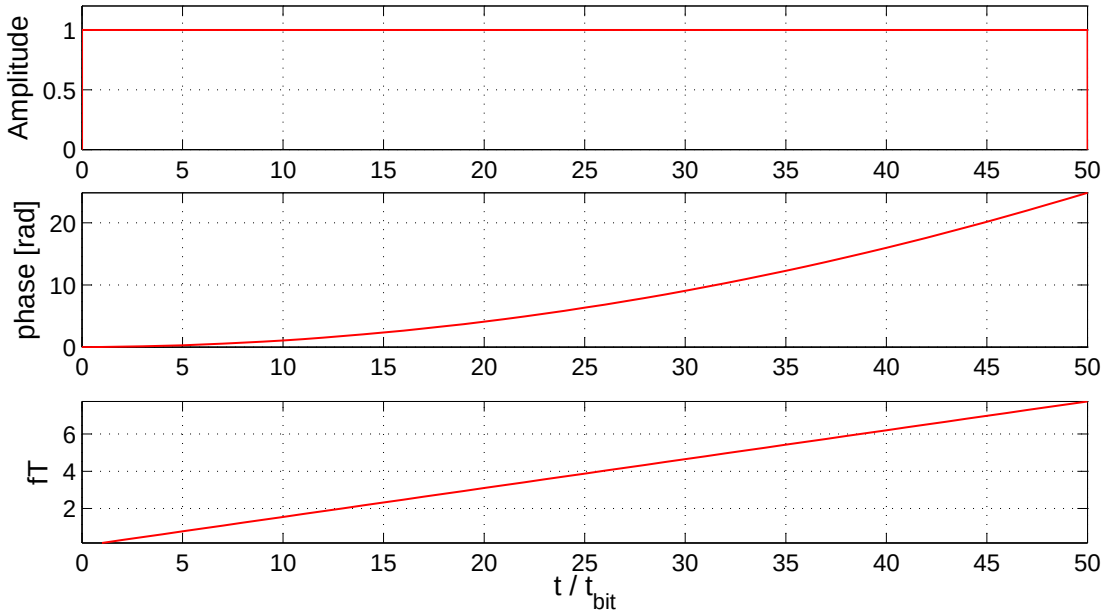

Figure 2.4: The amplitude (top), phase (middle) and frequency (bottom) as a function of t/t_{bit} for an LFM waveform. Here, t is time and t_{bit} is a bit length, a portion of the overall waveform duration T.

from $\sim$ 236,000 steps [*Cooper*, 2006]. The AD of the up-sweep LFM waveform and the corresponding ACF and spectrum are plotted in Figures 2.5 and 2.6, respectively.

One noticeable feature of the LFM ACF, in Figure 2.6, which can also been seen in the LFM AD in Figure 2.5, is the suggestion that the range resolution of an LFM waveform is much less than that of a constant frequency pulse, plotted in Figure 2.3. Both the square pulse and the LFM pulse have equivalent frequency resolutions (the first null along the $|\chi(0,\nu)|$ axis is the same value); however, the range resolution for the LFM pulse (Figure 2.6) is smaller since the location of the first null along the $|\chi(\tau,0)|$ axis is smaller than that of the single pulse (Figure 2.3). This effect is referred to as pulse compression and is a commonly used technique in radar waveform design to increase the range resolution of a radar system; however, it was not used in this research and will not be discussed any further.

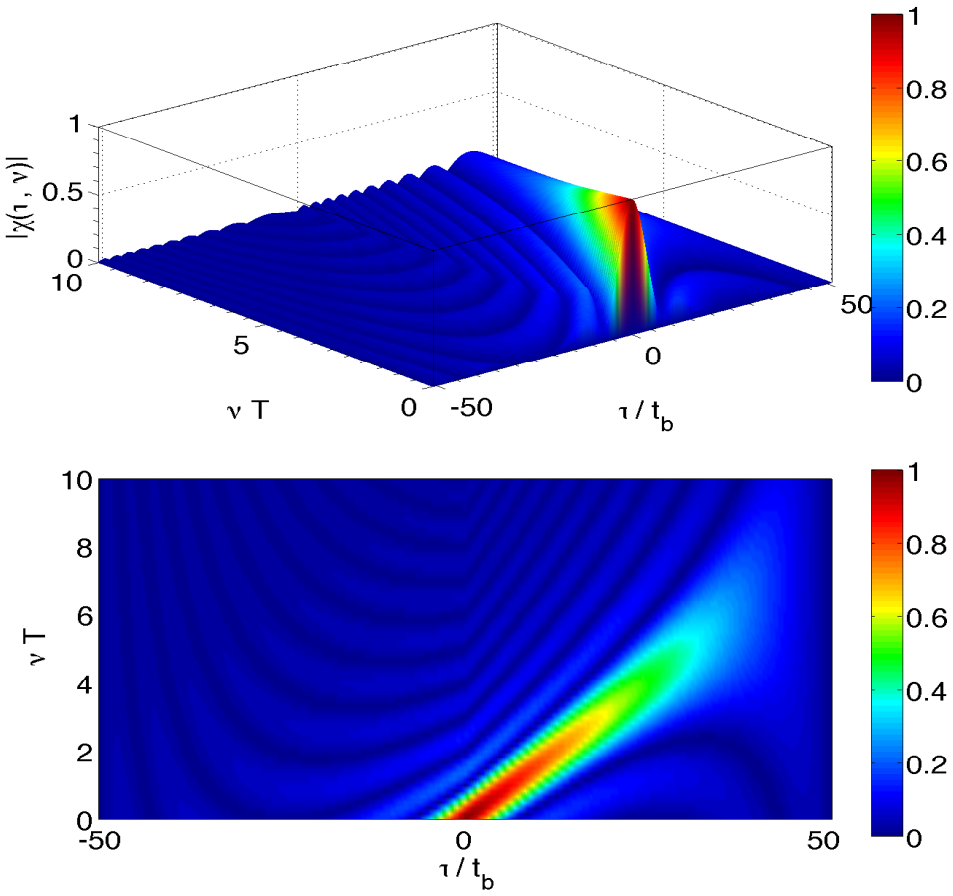

Figure 2.5: The AD for an up-sweep LFM waveform. The bottom plot is an overhead view of the AD. The amplitude, phase and frequency of the pulse are plotted in Figure 2.4. The most prominent feature in the LFM AD is the angled ridge, an indication of range-Doppler coupling.

Range-Doppler Coupling

The variation in carrier frequency has a notable effect on the AD, and therefore the performance of the LFM waveform. An effect known as the the *LFM effect* [*Levanon*, 1988; *Levanon and Mozeson*, 2004a; *Rihaczek*, 1969] is present and is attributed to a coupling of the range and Doppler frequency information in a scattering process. In the case of the FMCW system using the LFM waveform, both range and Doppler frequency information were measured in the frequency domain whereas in a typical pulsed radar system range information is measured in the time domain and Doppler

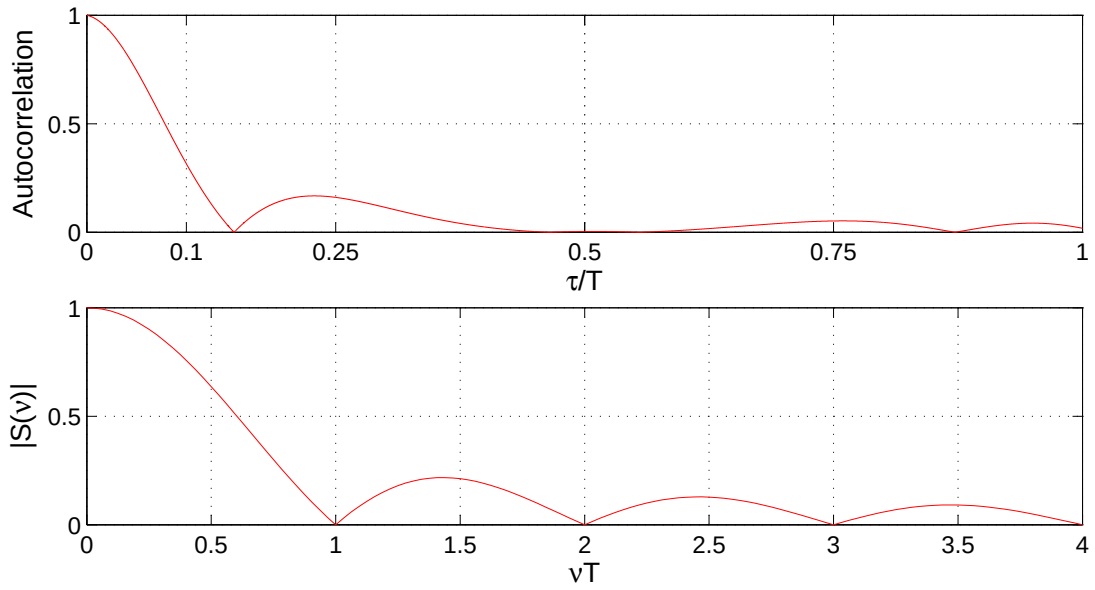

Figure 2.6: The spectrum (bottom) of an up-sweep LFM pulse. The spectrum is a plot along the $|\chi(0,\nu)|$ cut of the AD in Figure 2.5. The top plot is the ACF ($|\chi(\tau,0)|$).

frequency information is measured in the frequency domain. The range-Doppler coupling effect presents itself as an indeterminacy between the range and Doppler frequency information of a radar scatterer. The true range of a radar target with some radial velocity cannot be known entirely since the range information is coupled with the velocity information. The range-Doppler coupling effect produced by an LFM waveform is shown as an angled ridge in the up-sweep LFM AD in Figure 2.5. For a down-sweep LFM waveform, the angled ridge is reflected across the νT axis.

The single square pulse AD in Figure 2.2 does not display an angled ridge and therefore does not exhibit any range-Doppler coupling. Therefore, a range measurement will not be coupled with Doppler frequency information and vice-versa. Furthermore, the absence of an angled ridge in Figure 2.2 is due to the fact that, as stated previously, for a pulsed radar system the range and Doppler frequency information are measured in the time and frequency domain, respectively, whereas for the LFM case both measurements are made in the frequency domain.

The shearing ridge in Figure 2.5 is a graphical representation of the range-Doppler

coupling effect. The ridge in Figure 2.5 is centered at the origin, indicating no mismatch in τ or ν. However, if one moves along the delay axis, corresponding to a range, the sheared ridge volume begins to appear along the Doppler frequency axis. The same occurs if one moves along the ν axis and volume begins to appear along the τ axis. The appearance of ambiguity volume in Doppler frequency shift as a function of delay indicates that a delay offset, corresponding to a target with some range, is equivalent to a Doppler frequency offset, corresponding to a radar target with a radial velocity. The two parameters, range and velocity, complement each other. From the output of the matched filter, range information for a radar target is proportional to radial velocity information for that target [*Rihaczek*, 1969]. This relationship, and the angled ridge footprint on the range-Doppler plane is described by [*Levanon and Mozeson*, 2004a; *Rihaczek*, 1969],

$$\nu + \Gamma\tau = 0, \tag{2.22}$$

where ν is a Doppler frequency shift, $\Gamma = \pm B/T$ and τ is a delay offset. Re-arranging produces,

$$\tau = -\frac{T}{\pm B}\nu. \tag{2.23}$$

Equation 2.23, describes the range-Doppler coupling effect. It shows that a delay τ is coupled to a Doppler frequency shift ν.

A consequence of the range-Doppler effect is range inaccuracy for a radar target. According to Equation 2.23, and supported by Figure 2.5, if a radar target is detected at some range and some radial velocity directed towards the radar, using an up-sweep LFM waveform, the range of the target will be under-estimated by a value of $(T/B)\nu$. Conversely, if a down-sweep LFM waveform is used for the same radar scatter event, implying B is a negative number, the range to the target will be over-estimated by the same magnitude.

The over- and under-estimates of radar target range using the LFM technique is an important result as it provides a technique by which a FMCW system may provide true range and Doppler velocity information for a radar target. If an up-

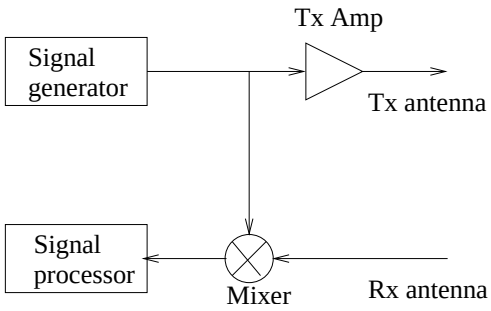

Figure 2.7: A basic block diagram of the FMCW system [*Cooper*, 2006].

sweep and down-sweep LFM waveform are used to detect a radar target they are able to decouple the range and Doppler velocity information.

2.3 The FMCW Radar System

The FMCW radar system, created by *Cooper* [2006], employed an LFM waveform and used the range-Doppler coupling effect to provide accurate range and Doppler frequency information with excellent spatial and temporal resolution. A block diagram showing the basic construction of the FMCW system is provided in Figure 2.7. The basic operation of the FMCW system involved mixing a copy of the transmitted LFM waveform with the received signal. This procedure was performed in real-time and produced a signal with a carrier frequency that was equivalent to the difference between the Tx and Rx signals. The range and Doppler frequency information was retrieved from the difference signal.

The FMCW radar transmitted both an up-sweep and a down-sweep LFM waveform, which were combined to form a triangle waveform as shown in Figure 2.8. The bandwidth of the waveform was B = 154.3 kHz and the waveform duration was T = 426 ms (213 ms for each of the up- and down-sweep LFM).

The FMCW system provided a range resolution of $\Delta R = 970$ m and a frequency resolution of $\Delta f = 4.69$ Hz [*Cooper*, 2006]. The FMCW system was capable of detecting a target between the line-of-sight ranges of 415 to 993 km with a mean Doppler frequency shift of up to 500 Hz in a direction towards or away from the

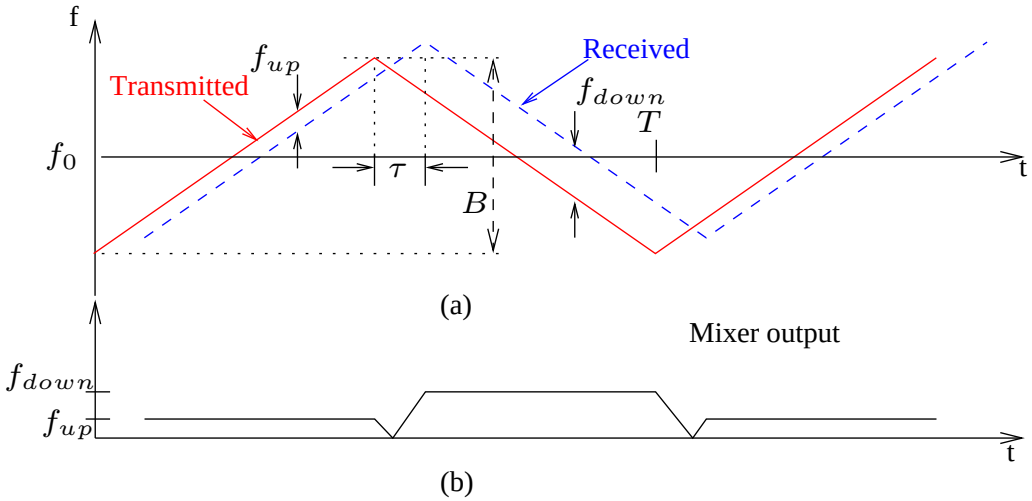

Figure 2.8: The triangle waveform of the FMCW system, (a), composed of an up-sweep and down-sweep LFM along with the output of the the mixer (b). B is the bandwidth of the waveform, T is the waveform duration, f_0 is a reference frequency, τ is the delay between the Tx (red) and Rx (blue) waveforms, f_{up} is the difference frequency between the Tx and Rx up-sweep LFM and f_{down} is the difference frequency for the down-sweep LFM. In (b) the output of the mixer, equivalent to the matched filter, has a carrier frequency equivalent to f_{up} and f_{down} [*Cooper*, 2006].

radar.

For the FMCW system, the process of measuring the range and radial velocity of a detected radar target began at the Tx side of the system. Here, an up-sweep LFM waveform was transmitted. The transmitted signal propagated to the E region, backscattered off a plasma instability and returned to the radar system to be received. As shown in Figure 2.7, the received signal was then mixed with a copy of the up-sweep LFM transmitted signal.

It is important to note that in the mixing process the received signal was mixed with a real time copy of the transmitted signal. The Rx signal that was received was being mixed with the Tx signal that was being transmitted. This portion of the radar system was a matched filter as described in Section 2.1: the copy of the transmitted signal was the impulse response of the matched filter through which the received signal was being filtered [*Skolnik*, 1980; *Eaves and Reedy*, 1987]. The carrier frequency of the transmitted signal was changing linearly, throughout T, and so the

carrier frequency of the received signal was different than that of the transmitted signal. The Tx and Rx signals were therefore mismatched due to a propagation delay. At this point the Doppler frequency shift imposed on the Rx signal, which is much smaller but still measurable as compared to the frequency corresponding to the range measurement, has not been accounted for but will be immediately below.

After the mixing process, the Rx signal was digitized and Fourier transformed. A moving average, noise reduction procedure and an amplitude SNR (labeled SNR_A) calculation were performed on the Fourier transformed mixed signal. The entire process, from signal Tx to the SNR_A calculation was repeated for a down-sweep LFM immediately after the up-sweep. A plot of the SNR_A as a function of frequency is shown in Figure 2.9 for a radar scatter event from 9:54:18 UT on November 21, 2009. The vertical axis corresponds to the value of the amplitude SNR_A and the horizontal axis is in units of frequency, Hz. The top panel in Figure 2.9 is from the up-sweep LFM radar waveform and the middle panel is from the down-sweep LFM waveform. The bottom panel shows the convolution of the top two panels as a function of range.

Signal to Noise Ratio Amplitude Calculation

In the Signal to Noise Ratio amplitude calculation (SNR_A) performed in the FMCW data analysis procedure, the strength of a signal is mathematically compared to the expected strength of the noise of the system. The SNR_A calculation performed by the FMCW analysis is,

$$SNR_A = \frac{Signal - Noise}{Noise}, \tag{2.24}$$

where $Signal$ is a received signal and $Noise$ is the expected amount of random and irrelevant signal, or noise, inherent to and detected by the FMCW system. In Equation 2.24, the variable $Noise$ was determined by sampling a radar Rx signal at frequencies where E region scatter signal is not expected [*Cooper*, 2006].

For the FMCW system, E-region scatter was typically observed in a difference frequency range of 2000 to 4800 Hz corresponding to a range of 415 km to 993 km

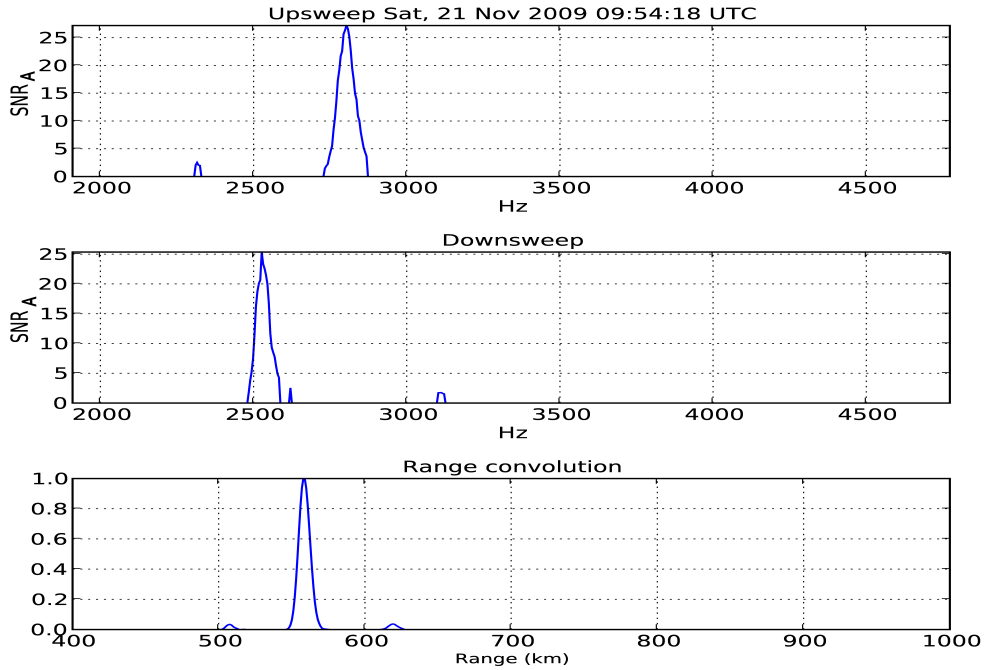

Figure 2.9: An SNR_A spectrum for a scattering event from 9:54:18 UT November 21, 2009.

(according to Equation 2.25 which will be explained shortly) [*Cooper*, 2006]. No relevant signal was expected outside of the 2800 Hz bandwidth, thus any frequencies which were close to, but not within the bandwidth were suitable to sample for the determination of $Noise$. For the FMCW system, *Cooper* [2006] chose the frequency range of 1500 to 2000 Hz to provide a value for $Noise$.

The post-reception procedure, including the SNR_A calculation, was repeated ten times for each sweep and gave the FMCW system an integration (temporal resolution) time of $\sim$ 5 s. Assuming that the plasma process that the radar signal was measuring did not vary significantly throughout the integration time, the frequency at which the spectral peak in the top panel is centered at is different from the spectral peak in the middle panel. This difference is due to the range-Doppler coupling effect established in Equation 2.23. The peak spectral frequency in the top panel corresponds to an under-estimation (up-sweep) of the radar target range while the

spectral peak in the middle panel corresponds to an over-estimation (down-sweep) of the target range. Figure 2.9 appears to contradict the previous statements; however, in this case the radar echo displays a velocity directed away from the radar system. Following from Equation 2.23, the separation of the peaks is dependent on the radial velocity of the scatterer.

With this information the true range of the radar target can be calculated from the mean of the over- and under-estimations of the target range. The mean range calculation is [*Eaves and Reedy*, 1987; *Cooper*, 2006],

$$R = \frac{f_{up} + f_{down}}{2} \frac{cT}{4B}, \tag{2.25}$$

where R is the range to the radar target, f_{up} is the center frequency of the peak in the up-sweep spectral SNR_A, and f_{down} is the center frequency in the down-sweep SNR_A and the definitions of c, T and B have not changed.

The Doppler frequency shift of the radar target is simply the frequency difference between the spectral peak in the up-sweep and down-sweep SNR_A [*Eaves and Reedy*, 1987; *Cooper*, 2006],

$$\nu = \frac{f_{down} - f_{up}}{2}. \tag{2.26}$$

Inspection of Equations 2.25 and 2.26 show a sum and difference formulation of the independent up- and down-sweep measurements used to obtain range and Doppler frequency shift. In the time domain a sum and difference operation is a multiplication process and according to the time-convolution theorem, this is equivalent to a convolution in the frequency domain [*Brigham*, 1988]. The convolution process is described graphically in Figure 2.10.

FMCW Convolution Procedure

During the convolution process described by Figure 2.10, the spectral peak in the up-sweep spectral SNR_A was shifted to the left in steps equivalent to the range resolution of the FMCW system. In (a), the up- and down-sweep SNR_As were multiplied. Since the spectral peaks did not have any common area their product

was zero, as shown in the plot on the right hand side. In (b), the respective peaks were shifted and multiplied once again; however, no overlap between the two existed and thus the value of the convolution remained at zero. Finally, in (c) the spectral peaks coincided and thus their product produced a peak as shown on the right. The peak corresponds to the median of the up- and down-sweep SNR_A peak frequencies and thus the range of the radar target.

A plot of the entire convolution process, referred to as a range-Doppler map, is subsequently produced from the convolution process. A range-Doppler map for the scattering event at 9:54:18 UT on November 21, 2009 is plotted in Figure 2.11. The horizontal axis on the range-Doppler map shows the Doppler frequency information of the radar target while the vertical axis gives the range information of the radar target. The peak SNR power (SNR_P) of the scattering event is shown in the top right corner of the map. A color bar on the right hand side of the map is used to display the SNR_P spectral spread of the scattering event.

2.3.1 Data Association

The previous description provided details of the operation of the FMCW system when a single radar target is detected. The FMCW radar system has been shown to be highly effective for single scattering events and it can also be effective for multiple scattering events, but case by case intervention is needed [*Cooper*, 2006], as spectral ghosts are typically present when multiple scattering events occur. There is a fundamental problem in pattern recognition and signal analysis theory known as a data association problem [*Petsios et al.*, 2008; *Hugot et al.*, 2006]. A data association problem can occur when data from independent sources, measuring an identical process, are compared with one another. Generally, if the object or process being measured is simple and basic, assumptions can be made about the independent measurements and they can therefore be easily correlated. However, as the measured process becomes more complex, assumptions originally made for a less complicated system may no longer be valid. Consequently, the invalid assumptions may produce

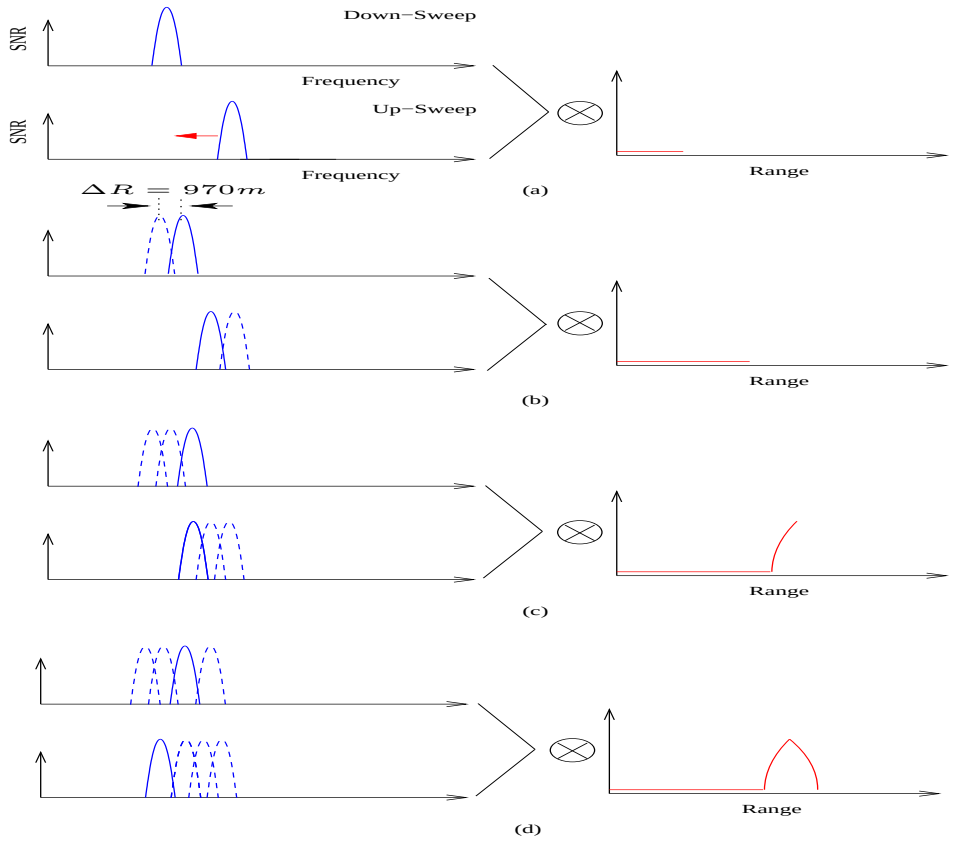

Figure 2.10: A diagram demonstrating the convolution process involved in the FMCW analysis procedure. Steps (a) to (d) show the shifting and multiplying process. ΔR is the range resolution of the FMCW system, and the magnitude of the incremental steps in the convolution.

unwanted and ambiguous information.

The triangular waveform technique used by the FMCW radar system can exhibit a data association problem. The use of a triangle radar waveform, composed of an up-sweep and down-sweep LFM waveform, produces two independent measurements of a radar echo. The first independent measurement produces the up-sweep spectral SNR_A and the second is the down-sweep spectral SNR_A. If a single radar target is only present in a measured radar event, a valid assumption is made that the spectral peak in the up-sweep SNR_A is directly associated with the spectral peak in the down-sweep SNR_A. There is only a single possible spectral peak in one SNR_A that a peak in another SNR_A can be associated with. However, if multiple radar targets are present in a scattering event, as seen in Figure 2.12, the assumption made in the

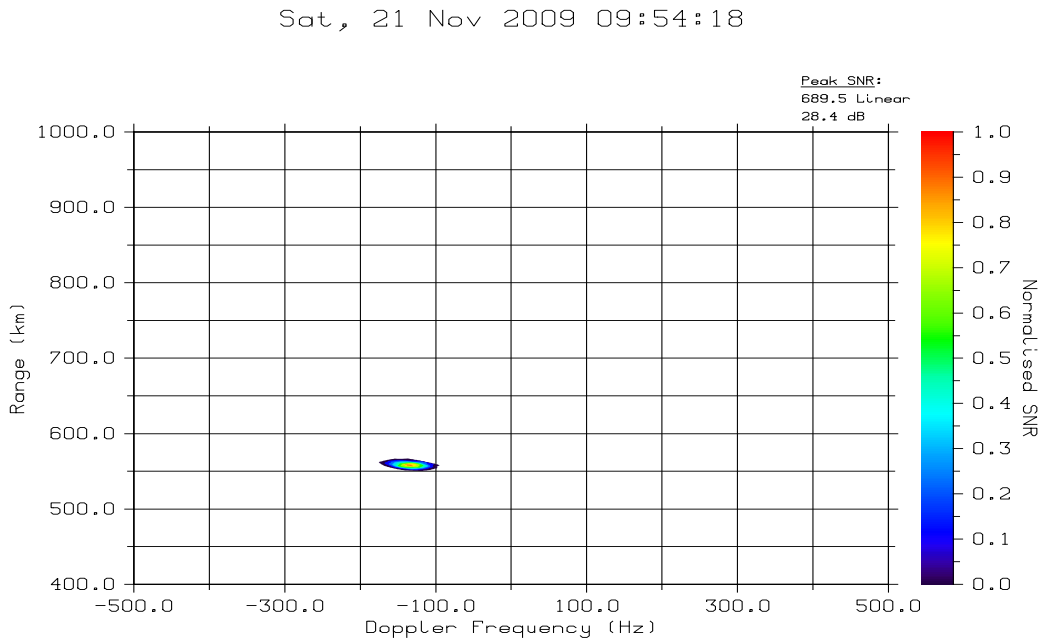

Figure 2.11: A range-Doppler map from 9:54:18 UT on November 21, 2009. The radar target was at a range of ~ 551 km with a mean Doppler frequency shift centered at ~ -130 Hz, indicating motion away from the radar. The peak power of the target was 28.4 dB.

single target case can no longer be made with certainty, as the spectral peaks in the up- and down-swept SNR_As could be associated with the non-corresponding peaks (cross-convolution terms) when correlating SNR_A spectra. These cross-convolution terms were referred to as spectral ghost targets in the FMCW system analysis by *Cooper* [2006].

Spectral Ghosting

When multiple targets are detected by the FMCW system in a radar scattering event, multiple spectral peaks are present in the respective up- and down-sweep spectral SNR_As. This is demonstrated in Figure 2.12 where the spectral SNR_As of a scattering event from 7:16:51 UT on November 25, 2009 are displayed. Two spectral peaks are present in each of the up- and down-sweep spectral SNR_As. As a result of the convolution between the up- and down-sweep SNR_As, additional cross-convolution

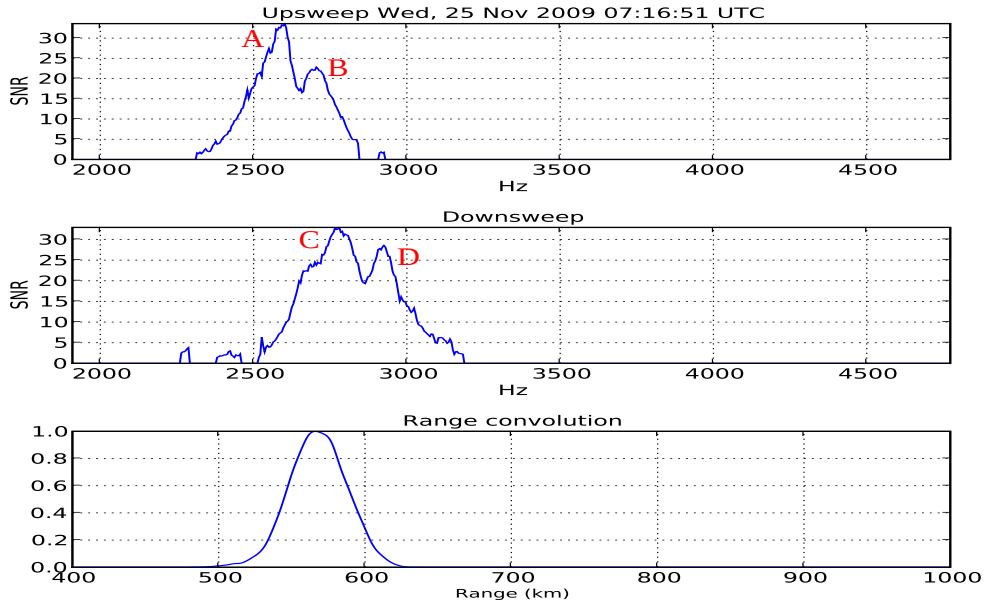

Figure 2.12: The spectral up- and down-sweep SNR_As for a radar scatter event from November 25, 2009 at 7:16:51 UT in which two radar targets were present. The spectral peaks of the targets are labeled A and B for the up-sweep SNR_A and C and D for the down-sweep SNR_A. The corresponding range-Doppler map is plotted in Figure 2.13.

spectral peaks and therefore radar ghost targets appeared in the range-Doppler map as demonstrated in Figure 2.13. The range-Doppler map shows the presence of four radar targets for the event although the individual spectral SNR_As would suggest only two targets by their double peaks. Two of the radar targets in Figure 2.13 were not associated with the scattering process and are spectral ghosts. For basic multiple targets cases, such as that shown in Figure 2.13, the spectral ghost targets are easily identifiable and can be removed manually. This process would be cumbersome to automate, however. In more complex multiple target cases the ghost targets are not identifiable at all and thus can not be removed from the data manually let alone by an automated process.

Going through the convolution process in detail in Figure 2.12, peak A in the up-sweep SNR_A is only associated with either peak C or D in the down-sweep SNR_A. In the convolution process, both spectral SNR_As were convolved with each other,

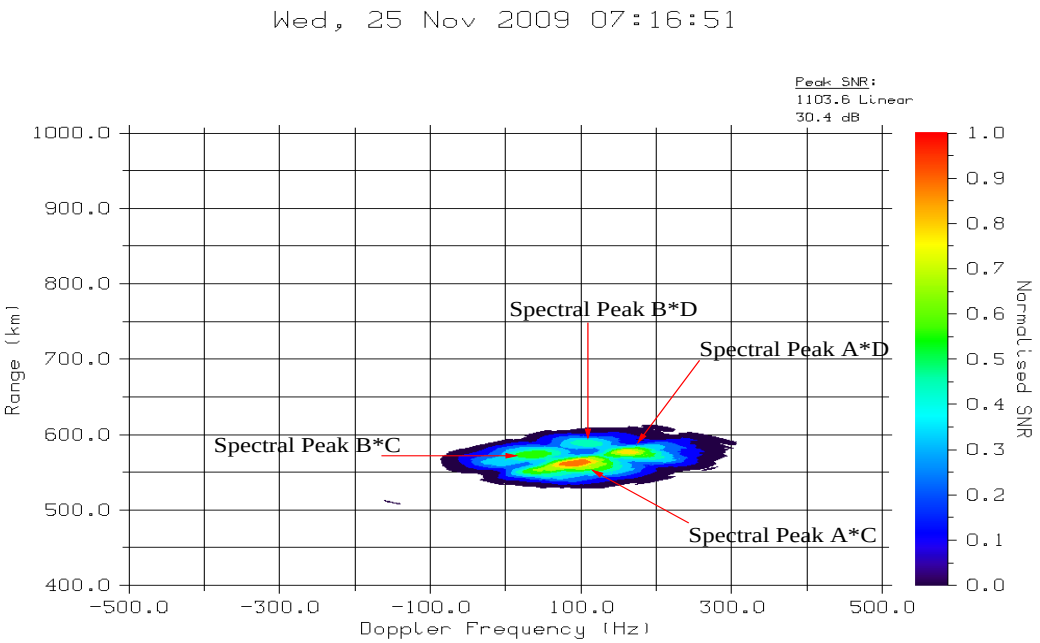

Figure 2.13: A range-Doppler map from 7:16:51 UT on November 25, 2009. This range-Doppler map was created from the SNR_A spectrum in Figure 2.12. Here four possible radar targets were heading towards the radar. The targets are at a range of $\sim$ 555 km with a mean Doppler frequency shift of $\sim$ 90 Hz (product AC from Figure 2.12), $\sim$ 565 km with a mean Doppler frequency shift of $\sim$ 35 Hz (product BC), at a range of $\sim$ 570 km with a mean Doppler frequency shift of $\sim$ 165 Hz (product AD) and $\sim$ 582 km with a mean Doppler frequency shift of $\sim$ 110 Hz (product BD).

as demonstrated in Figure 2.10 for single a peaked spectrum, and thus peak A was convolved with peak C and D. Similarly, Peak B was convolved with peaks C and D as well. This convolution produced four peaks in the range-Doppler map (Figure 2.13) from the four products, two of which are spectral peaks not associated with one another and considered cross-convolution terms. Since the peaks that produced the cross-convolution terms are not associated with one another, they give ghost radar target information appearing on the range-Doppler map.

A solution to the data association problem, and therefore to the spectral ghosting problem, is to avoid any association between multiple independent measurements. Unfortunately, since the FMCW system relied on using two LFM radar waveforms to retrieve range and Doppler frequency information, data association was unavoidable

and thus spectral ghosting was as well. There are radar systems that are capable of measuring E-region processes that avoid data association problems, but each system offers advantages and dis-advantages for use in auroral E region radar experiments. The following is a discussion about the data analysis techniques used by two systems in particular, the Manastash Ridge Radar (MRR) system [*Lind*, 1999] and the SuperDARN radar system. A comparison of the strengths and weaknesses between these systems and the FMCW system for auroral E region radar instrumentation is also made.

2.4 Other Radar Systems

Two other radars of interest are the Super Dual Auroral Radar Network (SuperDARN) radar system [*Greenwald et al.*, 1995] and the Manastash Ridge Radar system (MRR) [*Lind*, 1999]. SuperDARN is a radar network with individual, and similarly operated, radar systems located throughout the northern and southern hemispheres. The MRR system is a passive radar system located outside of Seattle, Washington in the United States.

Both systems use different techniques to provide range and Doppler velocity information for coherent ionospheric backscatter. Even though the waveforms and specifications of both radar systems are vastly different from each other, as well as from the FMCW system, neither the SuperDARN nor the MRR system are vulnerable to a data association problem; however, each system is susceptible to other difficulties unique to their implemented radar waveforms. Both systems avoid data association problems due to the radar waveforms and analysis techniques they both employ. If the waveforms and analysis techniques are compared to those of the FMCW system in the context of the AF and AD tools outlined in this chapter, a solution to the FMCW data association problem can be developed. The waveform and analysis techniques of the SuperDARN and MRR systems are now described. A comparison of the FMCW, MRR, STARE and SuperDARN radar systems is given

	FMCW	MRR	SuperDARN	STARE
Waveform	LFM	Non-Linear FM	Square Pulse	Square Pulse
ΔR (km)	0.970	0.600	45	20
Δv (m/s)	14.1	1.5	N/A	150
Δt (s)	5	1	~ 10	20
T (s)	0.213	N/A	varies (~ 0.1)	varies (~ 0.1)
Tx/Rx	Mono-static	Bi-static	Mono-static	Mono-static
Data Association	Yes	No	No	No

Table 2.1: A comparison of the FMCW, MRR, SuperDARN and STARE radar systems. This table is a modified version of one by *Lind* [1999]. The velocity information of the SuperDARN system is derived from a fitting process and thus does not have a resolution as defined in this section. The MRR system is CW and therefore has an infinite waveform duration, T.

in Table 2.1.

2.4.1 SuperDARN Radar System

The SuperDARN system is a pulsed radar system. The system transmits a sequence of short and discrete pulses at a constant carrier frequency, instead of a long continuous wave signal with a linearly varying carrier frequency of the FMCW system. An example of a pattern of square, constant frequency and amplitude pulse sequence used by the SuperDARN system is provided in Figure 4.1 in Chapter 4.

In general, a SuperDARN system transmits a sequence of discrete pulses, of duration t_b, over a waveform duration, T. The pulse duration, t_b is several orders of magnitude less than the total signal length, T, and the number of pulses transmitted during T is typically less than ten [*Baker*, 2003]. Therefore, the transmitters of the system are inactive for a large portion of T. As the SuperDARN radars are mono-static systems, the Tx and Rx systems are co-located. To avoid overloading the Rx system, the transmitters must be inactive when the Rx system is active. While the transmitters are inactive, the Rx system is active and receiving backscatter signal

from the ionosphere [*Greenwald et al.*, 1995].

A time series of the Rx signal is constructed. However, since the receivers are active for the vast majority of T (they are de-activated while a transmission is occurring), and T is much greater than the round-trip time for a radar signal to the scattering region, the time series will be composed of signal received from all line-of-sight ranges during T causing the time series to have a total lack of coherency. To re-construct any relevant information, the Rx time series is correlated with a copy of the Tx pulse sequence, in increments of range resolution [*Baker*, 2003]. This method of filtering the pulse sequence through the Rx time series is a matched filter technique similar to that employed by the FMCW system. However, the FMCW system performed this task in real-time as the backscatter signal was being received.

If a radar target is present at some range, R, then the incremental filtering process will produce a signal with constant relative phase at the increment that corresponds to the range R. Similar to the process in the FMCW system and all matched filter procedures, the coherent signal output can describe the range and Doppler frequency information of the radar echo.

It is important to highlight some drawbacks of the SuperDARN system. As shown in Table 2.1, the SuperDARN radar system has a relatively large range resolution, on the order of $\sim$ 45 km (see Section 2.2.2). Auroral E-region processes have a high spatial variability requiring a finer spatial resolution than the SuperDARN system can provide. However, it must be noted that the SuperDARN system is designed to make F-region measurements where a $\sim$ 45 km range resolution is more acceptable. Furthermore, the SuperDARN radar technique assumes single-peaked spectra (a better assumption for F-region scatter); that is, unlike the FMCW radar system, it assumes only single radar scatterers are present. This is another disadvantage for auroral E region study since multiple spectra are fairly common due to the highly dynamic nature of the plasma processes involved.

The process used by the SuperDARN system is an effective method of providing the range and Doppler frequency information for a radar target. The FMCW system

requires a comparison between two independent data sets, the up- and down-sweep spectral SNR_As, to provide range and Doppler frequency information. The SuperDARN system only requires a single data set, the Rx time series. Data association problems will not occur with the SuperDARN system since associations between multiple data-sets are not required. This is a valuable insight, and the SuperDARN system provides a basic framework for an overall technique that will prevent data association problems encountered by the FMCW system. In the next section another similar technique, involving a CW radar system, instead of a pulsed system, is discussed.

2.4.2 Manastash Ridge Radar System

The Manastash Ridge Radar (MRR) system is a passive, non-linear CW radar system. The MRR is classified as passive since it does not have a specialized dedicated transmitter, instead it receives backscattered signal which is transmitted by a FM radio station that is not geographically local to the Rx system [*Lind*, 1999]. The MRR system is capable of providing extremely high temporal and spatial resolution E-region radar observations, as highlighted in Table 2.1. In a matched filter procedure similar to that used by the SuperDARN system, a copy of the transmitted FM radio station signal is correlated with a time series of the received backscatter signal [*Meyer*, 2003].

The Rx portion of the MRR system has two components, as illustrated in Figure 2.14. The first is a Rx antenna located adjacent to the FM radio station transmitter. Here, the Rx antenna records a copy of the transmitted FM radio signal. The second portion of the Rx system, which receives ionospheric backscatter, is located away from the transmitter location, on the other side of a mountain range. The mountain range provides the required isolation between the Tx and the Rx systems. From the two receivers two time series are created. One time series is the replica of the transmitted FM radio station signal, and the second is a time series of the received backscatter signal.

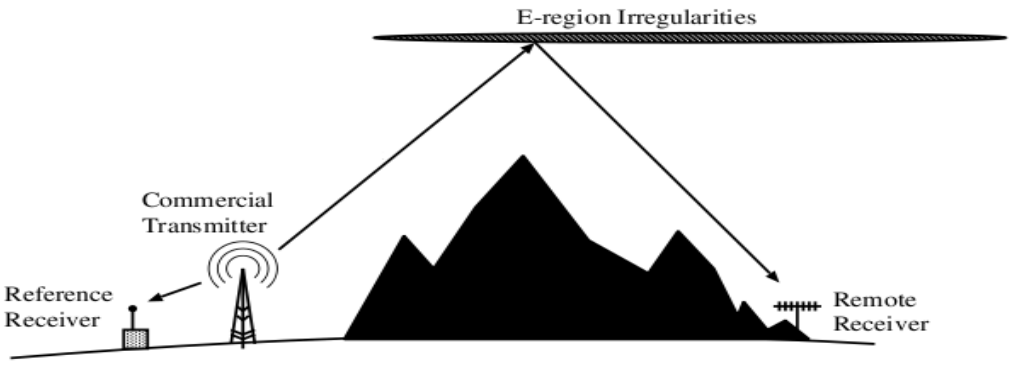

Figure 2.14: A graphic of the MRR radar system setup. The two components of the MRR Rx system are located on opposite sides of a mountain range [*Lind*, 1999].

Whereas the Tx signal of the SuperDARN radar system is a constant frequency pulse sequence, the Tx signal of the MRR radar system is a highly non-linear CW signal. The non-linearity of the MRR waveform is due to the fact that the FM radio station transmits a highly non-linear FM signal. In a process that is nearly identical to the technique employed by the SuperDARN radar system, a copy of the MRR Tx signal is matched to a copy of the Rx signal, in steps of the range resolution. A Doppler spectrum is constructed at each range step by comparing the Rx signal to a copy of the Tx signal at each range in the field-of-view of the MRR system.

Along with the technique used by the SuperDARN system, the signal analysis procedure employed by the MRR radar system is of importance to the FMCW data association problem. The MRR procedure avoids the data association problem since, like the SuperDARN procedure, all of the pertinent information is gathered from a single data set. More importantly though, the MRR technique is for a CW system. Unlike the SuperDARN system, the MRR provides a temporal and spatial resolution similar to that of the FMCW system. This is a result of the use of a CW waveform, which allows for high temporal resolution, rather than a pulsed waveform, which cannot provide a comparable temporal resolution. The MRR signal analysis procedure is an effective and data association free technique appropriate for a CW based radar system, like the FMCW system.

It is important to note that the MRR system possesses one significant drawback, however. The requirement for significant Tx and Rx isolation is unavoidable [*Lind*, 1999]. Very few geographic locations are both close enough to the northern auroral zone and possess natural isolation features like the MRR system. A technique that satisfies the requirement for the Tx and Rx isolation, without the use of natural geographic isolation barriers, has been developed in this work and is presented in Chapter 4.

Both the MRR and SuperDARN radar systems employ techniques which avoid a data association problem. If these techniques are employed with the FMCW system the spectral ghosting may be avoided. The MRR and SuperDARN each offer strengths and weaknesses based on the radar waveform that they employ. In general, pulsed radar systems cannot offer the temporal resolution of a CW system yet CW systems cannot offer the range resolution of a pulsed system and therefore large trade-offs between both types of systems exist. The MRR radar system offers both high spatial and temporal resolution; however, the geographic requirements of the system are un-appealing. Techniques from both a pulsed system, like the SuperDARN radar system, and a CW system, like the MRR system, have been investigated for implementation with the FMCW system. More specifically, focus is placed on how a radar waveform can be designed to offer the range and Doppler frequency resolutions required for auroral E-region study with the FMCW system while avoiding a data association problem. This is the subject of Chapter 4.

Nonetheless, the present FMCW system has proven to be a valuable tool for auroral E-region radar backscatter studies. Some solutions do exist to recognize and deal with the spectral ghosting issue. An analysis technique, established for this research to resolve spectral ghost targets from backscatter information is presented in the next chapter.

Chapter 3

Analysis Technique Modifications for the FMCW System

This chapter describes two techniques that were proposed to solve the spectral ghosting problem encountered by the FMCW system. The first technique, the two-bandwidth sweep solution developed by *Cooper* [2006], is re-introduced and discussed. The second technique, the peak-finder solution, was developed for this research as a replacement for the two-bandwidth technique. A comparison between both techniques follows and, in addition, a modification to the Signal-to-Noise Ratio amplitude calculation (SNR_A) has been implemented for the FMCW analysis.

3.1 Two-Bandwidth Sweep Solution

In an effort to resolve the spectral ghosting problem, *Cooper* [2006] created an alternate waveform for the FMCW system referred to as the two-bandwidth, or two-BW, sweep. The two-BW sweep is a double triangle radar waveform wherein the second triangle sweep transmitted over a bandwidth that is half the size of the first triangle sweep. This is illustrated in Figure 3.1.

The purpose of using two triangle waveforms with two different bandwidths is to establish multiple independent measurements of the same scattering event. The range resolution, ΔR, of the FMCW system is a function of the triangle waveform bandwidth B. If the frequency sum term Equation 2.25 is taken to be the frequency resolution of the system, Δf, then

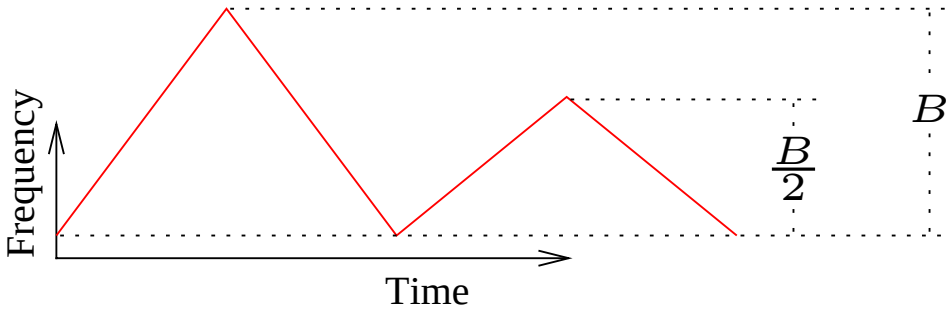

Figure 3.1: The double triangle waveform of the two-BW sweep technique. The bandwidth of the second waveform, $B/2$, is half the magnitude of the first waveform B [*Cooper*, 2006].

$$\Delta R = \Delta f \frac{cT}{4B}. \tag{3.1}$$

Two independent measurements are made if the bandwidth, and thus the range resolution, is changed between the two triangle waveforms. Both measurements are considered independent since a scattering event is measured twice, once with a high range resolution waveform and once again with a lower range resolution waveform. When the spectra from the two bandwidths are compared, any artificial and ambiguous information, in the form of spectral ghosting, may be identified and eliminated.

Spectral ghosting, described in Section 2.3.1, occurs when multiple targets are present in a scattering event and the convolution process produces cross-convolution values in the FMCW analysis. The relation of range and Doppler frequency shift in the frequency domain (LFM technique), as given by Equation 2.23 ($\tau = -\nu T/\pm B$) expresses the over-/under-range estimation. If T is constant in Equation 2.23, then the range estimation from the up- and down-sweep LFM waveforms is a function of B, and thus the cross-convolution terms also depend on B. For the two-BW sweep technique, B was halved for the second triangle sweep and so, from Equation 2.23, the over-/under-estimation of the range to the target was doubled. Since the over-/under-estimation of range was altered, the cross-convolution terms were also altered, but the range information corresponding to the real radar targets remained the same. As a result, the range information corresponding to the spectral ghost targets was

different for the full-bandwidth and half-bandwidth triangle waveforms as illustrated in Figure 3.2.

The effect of varying B is illustrated in Figure 3.2 where a diagram depicts a multiple radar target event as measured by two LFM waveforms with bandwidth B (top) and $B/2$ (bottom) respectively. The vertical and horizontal axes represent arbitrary amplitudes and frequency, respectively. Notice that the mean ranges of target 1 (blue) and 2 (red) do not vary when the bandwidth changes from B to $B/2$. However, the mean ranges of the spectral ghost targets, corresponding to the cross-convolution of target 2 and 1 (brown) and target 1 and 2 (green) respectively, do change when the bandwidth changes. The different mean values for the spectral ghost targets indicates different range values for the ghost targets (cross-convolution terms) when measured with the full-bandwidth and half-bandwidth waveforms.

The most important effect of changing B, as illustrated in Figure 3.2, is the variation of the mean frequency values. The mean values of the associated spectra, corresponding to the range for the real radar targets, are identical for the two triangle waveforms. However, for the unassociated spectra, which produce the cross-convolution values and thus the spectral ghosts, the mean values differ between the two triangle waveforms. This indicates that the range values for the real radar targets are the same for the triangle waveforms with bandwidth B and $B/2$, but the range values for the spectral ghost targets are different for both triangle waveforms. This discrepancy is the basis of the two-BW sweep technique. *Cooper* [2006] created an analysis technique which compared the spectra from both the triangle waveforms. The analysis eliminated any spectral signal that was not consistently present at a given range when both the full- and half-bandwidth waveform spectra were compared.

3.1.1 Two-BW Sweep Performance

For a variety of multiple radar target conditions, the two-BW sweep technique was successful at resolving and eliminating spectral ghost targets. These cases involved

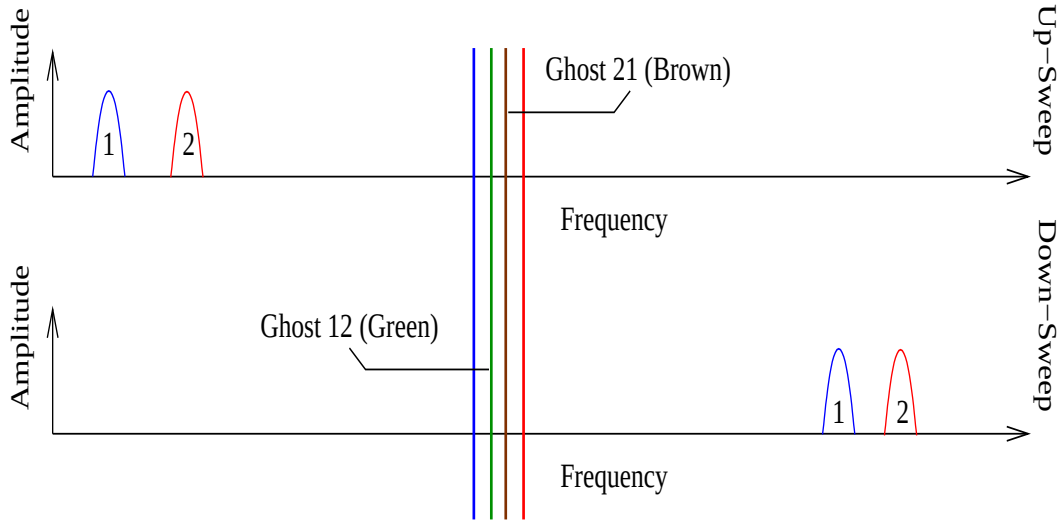

(a)

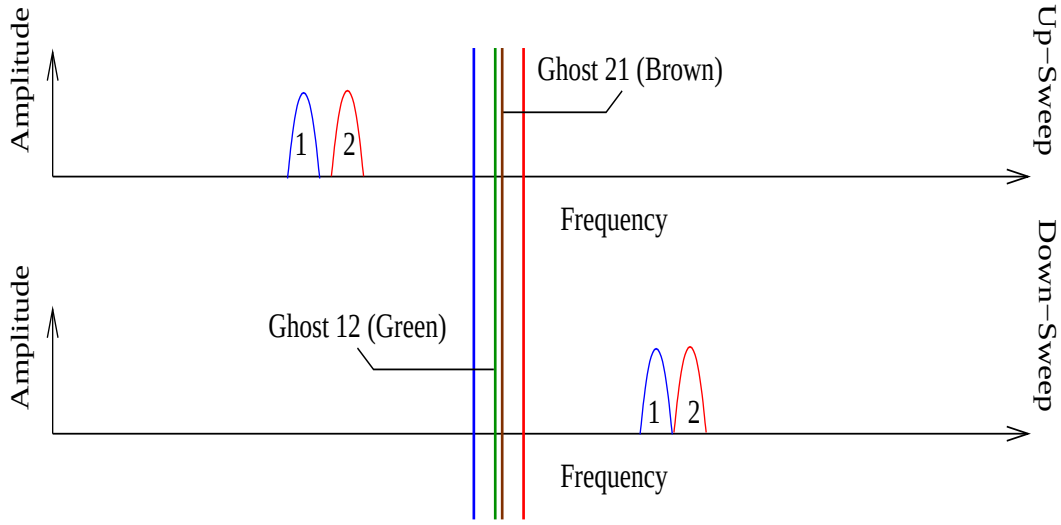

(b)

Figure 3.2: A diagram depicting a multiple target scattering event as seen with an LFM waveform with bandwidth (a) B and (b) $B/2$. The blue (red) line is the mean frequency, and thus range, of target 1 (2). The green (brown) line is the range of target 1 (2) in the up-sweep and target 2 (1) in the down-sweep; both are ghost ranges.

multiple scatter events where the radar targets were separated by distances and Doppler velocities equivalent to separations of $\sim$ 500 Hz in the frequency domain. For the two-BW method to work consistently well, any set of radar targets needed to be separated by at least $\sim$ 500 Hz in the corresponding SNR_A spectra. This frequency is equivalent to $\sim$ 100 km in range for a target with no Doppler frequency shift or $\sim$ 72 km with a Doppler frequency shift of 150 Hz (the majority of E-region backscatter at 50 MHz have Doppler frequency shifts with magnitudes of $\sim$ 150 Hz or less, see Section 5.1). For the FMCW radar system, multiple scatter events with their multiple spectra similar to those shown in Figures 3.3 and 3.4 were common. Although these multiple radar target conditions were often met, for the majority the range separation between the targets was rarely more than 100 km. In these close separation multiple scatter configurations (less than $\sim$ 500 Hz peak separation in the corresponding SNR_A spectra), the two-BW technique had difficulty eliminating spectral ghost targets.

Two-BW Sweep Limitations

The two-BW sweep technique encounters difficulty in eliminating spectral ghost targets for target conditions in which spectral SNR_A peaks were situated within $\sim$ 500 Hz. This can be attributed to the properties of the spectra involved in the analysis. In general, the majority of spectra from E-region plasma processes are spread over several frequency resolution cells [*Haldoupis et al.*, 2003], and therefore for the FMCW system several range and Doppler frequency resolution cells. When two or more targets with small SNR_A peak separation were present, their spectra overlapped. Due to the overlap, the two-BW analysis was unable to detect any change between the full- and half-bandwidth waveforms since the overlapped spectra was consistent between both sweeps. As a result, spectral ghosting failed to be identified and eliminated. This is shown in Figure 3.3 and 3.4. Here, two figures depict the same radar scatter event, from 10:56:27 UT on August 18, 2008, in which two radar targets were present and closely separated in frequency space.

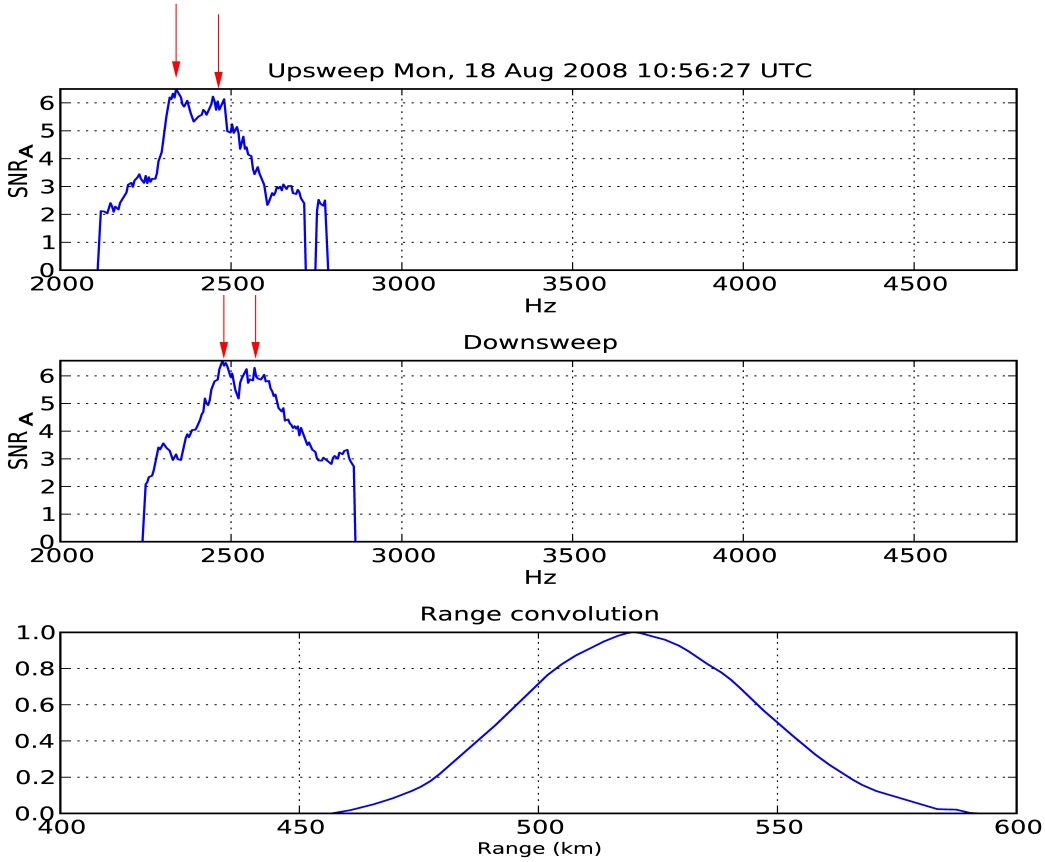

Figure 3.3: An SNR_A spectrum for the up- and down-sweep LFM with bandwidth, B, for a radar scatter event from 10:56:27 UT on August 18, 2008. The two highlighted SNR_A spectral peaks in both the up- and down-sweep spectra indicate two radar targets.

The SNR_A spectra in Figure 3.3 were produced using the full-bandwidth waveform in the two-BW sweep. The vertical axis is the SNR_A amplitude and the horizontal axis is the frequency in Hz. The third panel is a range convolution of the two spectra. These particular SNR_A spectra feature two closely separated radar targets with overlapping spectra, which are indicated by the red arrows in Figure 3.3. The overlapping spectra prevents the range convolution in Figure 3.3 from indicating the presence of multiple radar targets. In fact, the peak in the range convolution corresponds with the spectral ghost targets and neither of the real radar targets (the real and ghost targets are identified manually, which is discussed shortly). This spectral SNR_A is very typical of the multiple scatterer events observed with the FMCW

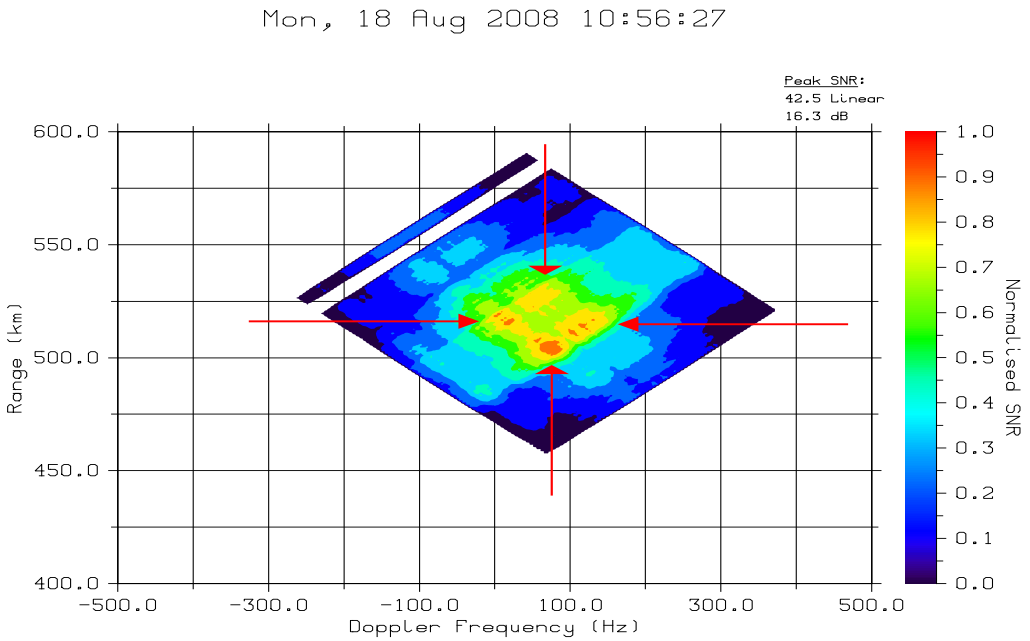

(a)

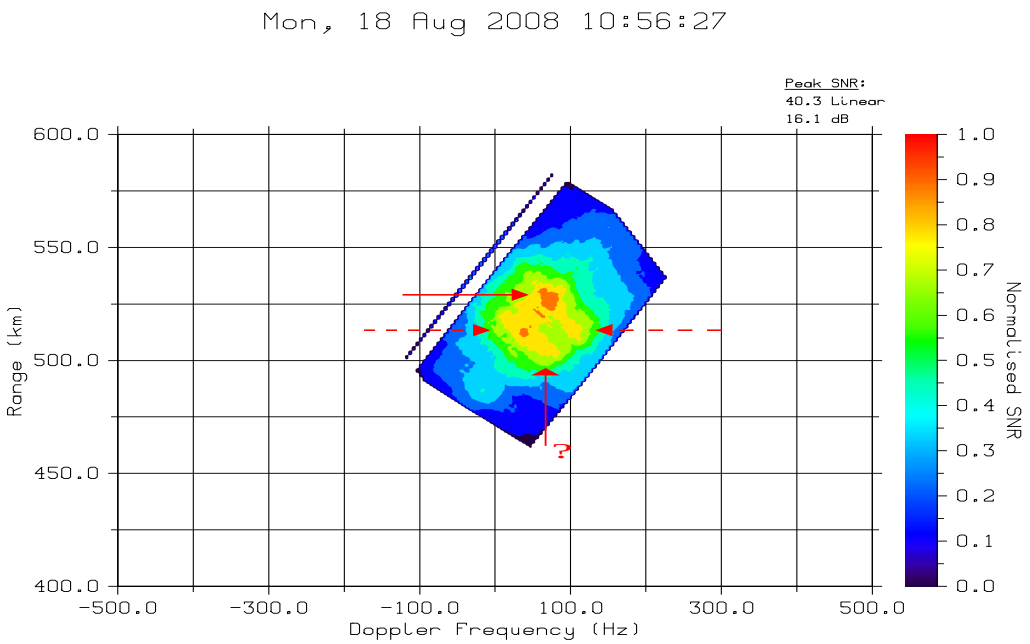

(b)

Figure 3.4: Range-Doppler maps from 10:56:27 UT on August 18, 2008. The map in (a) was created from the SNR_A spectra in Figure 3.3. The map in (b) was a product of the two-BW sweep technique.

system. From these spectra, the range-Doppler map is provided in Figure 3.4a. In the range-Doppler map there is clear evidence of spectral ghosting since four radar targets are (may be) present, even though the SNR_A spectra suggested two radar targets. The real and spectral ghost targets can be identified manually by comparing features of the up- and down-sweep SNR_A spectra. This technique is not practical since 12 SNR_A spectra (5 second resolution) are produced for every minute of received coherent backscatter signal and so the number of spectra can quickly overwhelm the analyst. All of the real and spectral ghost targets were identified manually in this thesis. Two ghost targets are found at a range of $\sim$ 515 km with Doppler frequencies centered at $\sim$ 10 Hz and $\sim$ 120 Hz respectively. A real radar target is located at a range of $\sim$ 505 km with a mean Doppler frequency shift of $\sim$ 80 Hz and a second weaker real target is located at a range of $\sim$ 525 km with a mean Doppler frequency shift of $\sim$ 70 Hz.

With certain radar target conditions, such as that displayed in Figure 3.4a, the spectral ghost targets can easily be identified. In Figure 3.4a the shape of the four possible radar targets creates a diamond shape. In the majority of cases with diamond shaped target conditions the left-most and right-most radar targets turn out to be the spectral ghosts since they do not correspond to expected auroral E-region echoes (further discussed in Section 5.1) and therefore are easily identifiable. However, countless other target conditions are possible and have been observed in which the spectral ghost targets are not so easily identified. The more difficult target conditions preventing the identification of spectral ghost targets make up a majority of multiple target radar events.

Figure 3.4a can be used to assess any spectral ghost elimination technique. The range-Doppler map in Figure 3.4a may be considered an imperfect map; that is, it includes all of the real radar targets as well as all of the spectral ghost targets due to cross-convolution. The success of any spectral ghost elimination technique can be based on the degree to which the ghost targets are eliminated from the undeveloped map.

The two-BW sweep technique was implemented for this event and a range-Doppler map showing the results of the two-BW process is provided in Figure 3.4b. Inspection of this map reveals that the close proximity of the spectral peaks in the SNR_A prevented the two-BW sweep technique from fully resolving the real radar targets and eliminating the spectral ghost targets. The dashed red arrows in Figure 3.4b indicate the locations of the ghost targets from Figure 3.4a. One can see that at these locations the spectral ghosting has not been completely eliminated (as the range-Doppler map still has some SNR power there), but they were suppressed however. Furthermore, an additional peak due to further spectral ghosting has been introduced in Figure 3.4b near $\sim$ 520 km in range and $\sim$ 30 Hz in Doppler frequency shift. In these radar target conditions the two-BW technique was unable to completely eliminate spectral ghosting and likely introduced data indicative of non-physical structure.

The two-BW was able to correctly identify the real radar target located at the $\sim$ 525 km range; however, it showed difficulty in identifying the second real radar target at the $\sim$ 505 km range. The location of the second real radar target in Figure 3.4b is indicated by a red arrow labeled with a question mark. The two-BW technique spread out the spectral peak associated with the second real radar target and as a result it is far more difficult to identify in Figure 3.4b than in Figure 3.4a. It may be argued that the second real radar target in Figure 3.4b would be un-identifiable unless one had knowledge of its whereabouts *a priori*. This is further evidence of the smoothing and suppressing due to the two-BW technique as in Figure 3.4a the real radar target at this range has the largest SNR power value whereas in Figure 3.4b it did not.

A more general and prominent drawback of the two-BW sweep technique is illustrated by examining the SNR_A spectra of the half-bandwidth triangle waveform from the 10:56:27 UT on August 18, 2008 event which is plotted in Figure 3.5. The two-BW sweep technique was contingent on both independent measurements, one from each triangle waveform, measuring the same radar targets under the same scattering

conditions. More specifically, the assumption that the first triangle waveform, with bandwidth B, was measuring the exact same target as the second triangle waveform with bandwidth $B/2$ was made. This should produce identical SNR_A spectra for both the full- and half-bandwidth triangle waveforms. One would expect that the two indicated SNR_A peaks in Figure 3.3 to be clearly identifiable in Figure 3.5, but this is not the case. Since the half-bandwidth SNR_A has half the range resolution (less resolvability, see Equation 3.1) the peaks in the corresponding SNR_A are pushed together causing the spectral peak associated with the second real radar target in Figure 3.4b to be severely suppressed and masked. The secondary peak is identified with a dashed red arrow labeled with a question mark in Figure 3.5. Once again, as with the case in Figure 3.4b, it would be difficult to identify the suppressed peak in Figure 3.5 without knowing its location from the corresponding full-bandwidth sweep observations.

The discrepancy between the two SNR_As in Figures 3.3 and 3.5 is the largest disadvantage for the two-BW sweep technique. It can be argued that this difficulty is the result of a data association problem (see Section 2.3.1) since the two-BW technique relies on the assumption that both the half- and full-bandwidth SNR_As had similar spectral features when they may not. This is due to the halving of the range resolution when switching from the full-bandwidth waveform to the half-bandwidth waveform (Equation 3.1). Due to this the spectral characteristics of the half-bandwidth observations were smoothed or smeared-out compared to the more detailed full-bandwidth ones. As a result, it was difficult to associate spectral features (i.e. the two spectral SNR_A peaks) in Figure 3.3 with those, or lack thereof, in Figure 3.5.

The two-BW sweep technique is an elegant and good first attempt at resolving the spectral ghosting problem. Unfortunately, the two-BW technique breaks down when it encounters certain radar target conditions. An alternative approach to the two-BW sweep technique, called the peak-finder technique, was developed to resolve this and is now described.

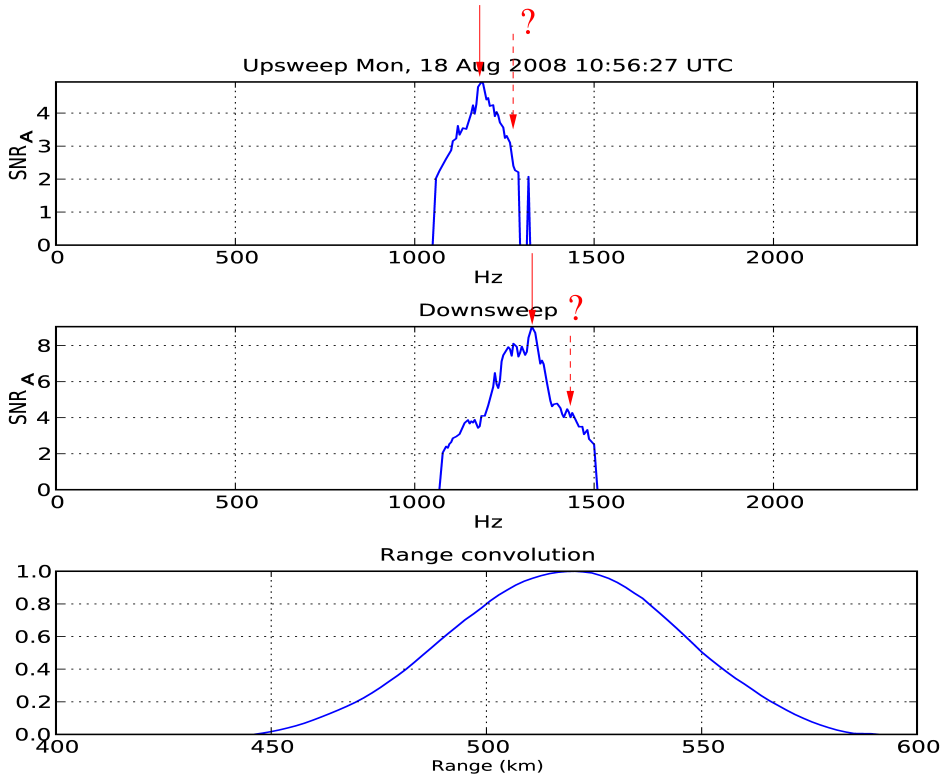

Figure 3.5: SNR_A spectra for the up- and down-sweep triangle waveform with half-bandwidth, $B/2$, for a radar scatter event from 10:56:27 UT on August 18, 2008.

3.2 Peak-Finder Solution

An alternate method designed to replace the two-BW sweep technique as a solution to eliminate spectral ghosting was developed for the FMCW system. As discussed in Section 3.1.1, the two-BW sweep technique encounters difficulty with certain multiple radar target configurations, most notably ones in which multiple radar targets were separated by less than $\sim$ 500 Hz in frequency space. A technique which can resolve spectral ghosting for any multiple target configuration is desired. The peak-finder technique was designed to identify real radar targets and eliminate spectral ghost targets. The purpose of creating the technique is not to offer any insight into the properties of the radar target or scattering event, but to simply separate real radar targets from spectral ghost targets for a given radar scattering event. As op-

posed to the two-BW sweep technique, the peak-finder technique does not require an additional triangle waveform to identify spectral ghosting. The peak-finder technique does not involve any alteration to the radar waveform, it is purely an analysis technique.

Spectral ghosting arises when the process of convolving multiple spectral SNR_A peaks, representing multiple radar targets, produces cross-convolution terms. Ghosting only appears when multiple radar targets are present in a scattering event. Since spectral ghosting is related to the cross-convolution terms, eliminating the cross-convolution terms will avoid the ghosts. The cross-convolution terms can be excluded from the convolution process if each spectral SNR_A peak is isolated and convolved separately from any other peak which may be present in the same spectrum.

The peak-finder technique consists of three main steps: spectral peak identification, noise associated peak reduction, and peak convolution.

3.2.1 Spectral Peak Identification

To isolate a spectral SNR_A peak, an identification process was first established. A peak is a discernible feature of a SNR_A spectrum and is characterized by a local maxima and width. For the FMCW system, radar echoes produced a variety of SNR_A spectral peaks, which, in general, were anywhere from a few tens of hertz to several hundred hertz in frequency width. A method of identifying a peak with all possible spectral widths was established. This was accomplished by use of a threshold condition in the SNR_A spectral analysis process.

For the FMCW system analysis, a peak, or local maximum, was considered to be an individual peak as long as the spectrum associated with it, in the immediate vicinity, remained within a certain percentage of the magnitude value of the peak. Many threshold percentages for the FMCW were tested for a variety of SNR_A spectra observed by the FMCW system. If a threshold value was too low, the analysis program included additional and unwanted spectral peaks. This would occur if a spectrum contained overlapping peaks where the valley separating the peaks was

higher than the threshold value. If the spectral threshold was too high, on the other hand, the peaks in the corresponding range-Doppler were very small and hard to distinguish. A threshold that struck a balance between these two extremes was determined by using various threshold values in the analysis for single and multiple spectral peaks corresponding to a variety of multiple radar target configurations. The threshold which identified individual SNR_A spectral peaks, of all widths, with the greatest success, was 75%. This was determined by visual inspection. A value lower than 75% tended to produce ghost targets and any higher suppressed spectral information (such as the approximate spectral width of the SNR_A peak). Thus a peak and any surrounding spectrum that was within 25% of the magnitude of the peak, was considered to be a single spectral peak.

3.2.2 Noise Associated Peak Reduction

Some SNR_A peaks had spectral widths as narrow as a few tens of Hz. These peaks were typically associated with meteor trail echoes [*Cooper*, 2006]. However, random and sporadic noise typically produced SNR_A spectral peaks with smaller widths, which could approach those of meteor trail echo widths. Due to the similarities of the two spectral peaks, a method of separating meteor trail echoes from random noise was developed. For the FMCW system, a meteor trail echo was considered an ideal echo due to its narrow and focused spectrum. From this, an assumption was made that any peak can be considered noise if its spectral width is narrower than what has been typically observed with meteor trail echoes. An analysis routine, called the de-spiking routine, which performed this task was created for the FMCW analysis procedure. Once a spectral peak was identified using the method described in Section 3.2.1, a conditional test was once again performed on the spectral peak. If the width of the spectral peak was narrower than that associated with a meteor trail, then the spectral peak was eliminated. From FMCW observations, the width of a spectral peak associated with a meteor trail was determined to be 20 Hz, an empirically derived value from inspecting several meteor echo events.

3.2.3 Peak-Finder Algorithm

With the method of SNR_A spectral peak detection established, the process of creating analysis free of spectral ghosting is outlined. The process of decoupling the range and Doppler frequency information in the SNR_A spectrum was the same for the peak-finder technique as it was for the procedure implemented by *Cooper* [2006]: a convolution between the up- and down-sweep spectral SNR_A was performed (see Section 2.3). The peak-finder technique has one main difference in that individual peaks are isolated before the convolution process so as to remove the cross-convolution terms.

The algorithm for the peak-finder analysis technique is outlined in Figure 3.6 and the convolution stage is illustrated in Figure 3.7. Using the conditions outlined in Section 3.2.1, peaks are identified in both the up- and down-sweep SNR_A spectra. The peak of the greatest magnitude, or *top* peak, is then isolated in both the up- and down-sweep spectra. Except for the portion of the respective up- and down-sweep spectra where the top peaks were located, all other spectra are set to zero.

The next step in the peak-finder algorithm is the convolution. This is a replica of the process undertaken by the FMCW analysis described in Section 2.3. The solitary peak from the up-sweep SNR_A spectrum is convolved with the solitary peak from the down-sweep SNR_A spectrum, as illustrated in Figure 3.7b. As before, the range and Doppler frequency information of the radar target are determined, but now there is no cross-convolution terms to create ghost targets. At this point the current top peak is removed from the original de-spiked spectrum, and the entire process, beginning with the spectral peak identification, was repeated as illustrated in Figure 3.6. For every iteration of the algorithm, the next lowest peak, as determined by the peak detection method, is isolated.

An important assumption is made in the peak-finder procedure. In the first step, the act of isolating the top peak in both the up- and down-sweep spectral SNR_As automatically associates each peak with one another. Thus, it was assumed that

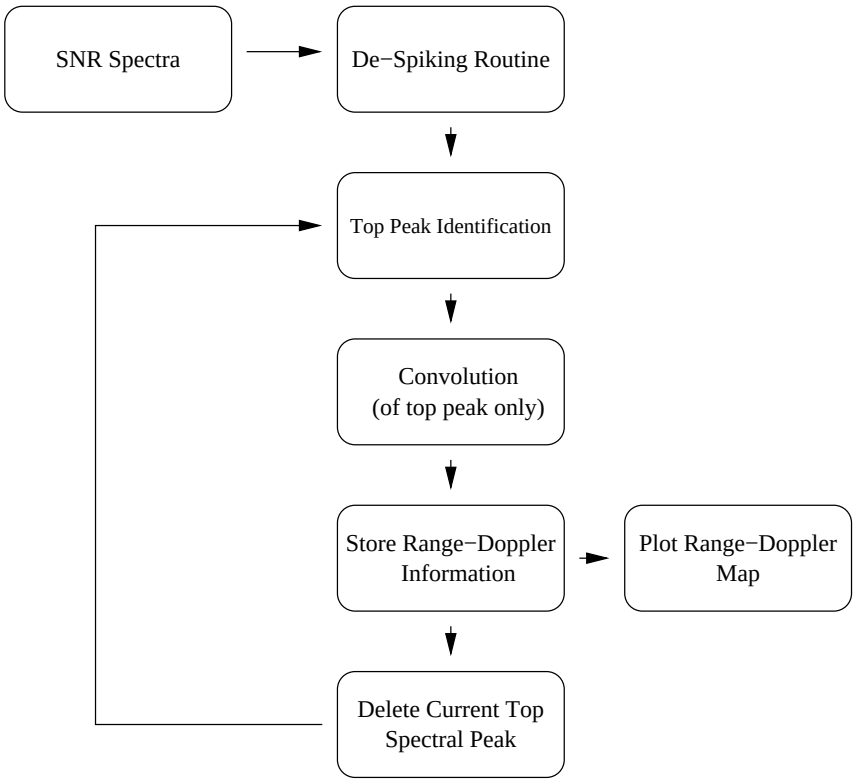

Figure 3.6: A flowchart showing the steps of the peak-finder algorithm.

the radar scatterer producing the top peak in the up-sweep SNR_A spectrum is the identical scatterer producing the top peak in the down-sweep SNR_A spectrum.

From observations provided by *Cooper* [2006] and observations performed for this research, this assumption remained valid in most scatter events; however, it is not ideal. The assumption is rendered invalid for the FMCW analysis and peak-finder procedure in cases where a different number of SNR_A peaks appeared in the up-sweep spectral SNR_A when compared to the down-sweep SNR_A. Although uncommon, special cases such as this gives difficulty to the FMCW analysis and peak-finder procedure and as a result produced minor spectral-ghosting. Nevertheless, the peak-finder solution provided a marked improvement in eliminating spectral ghosting when compared to the two-BW sweep technique.

The effectiveness of the peak-finder technique is illustrated in Figure 3.8 when compared to Figure 3.4a where the range-Doppler maps of the same radar scattering event from August 18, 2008 are plotted. The range-Doppler map in Figure 3.4a

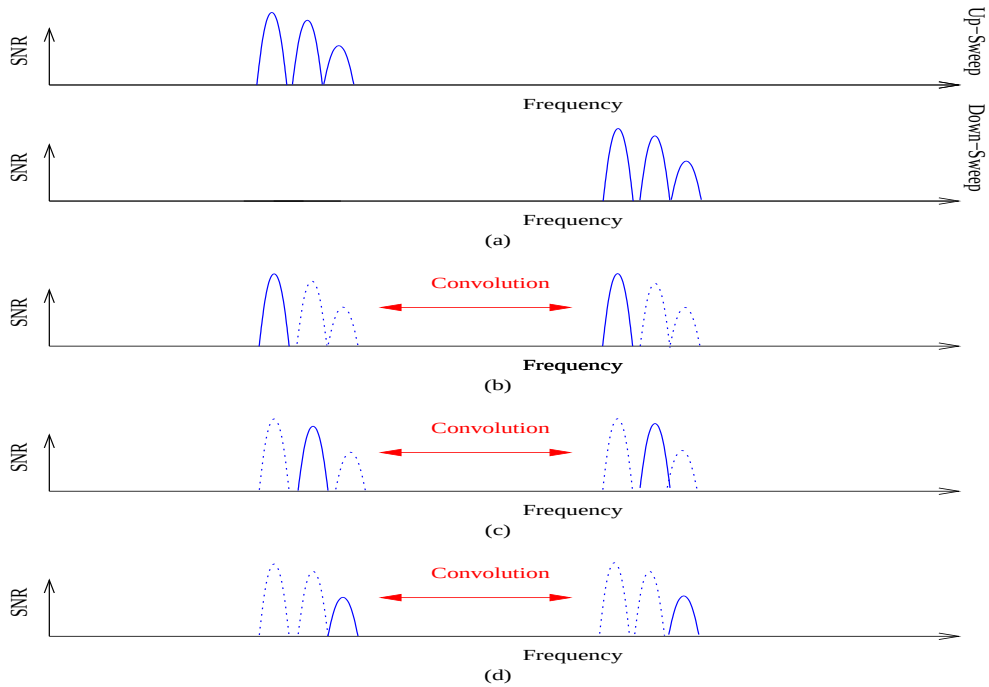

Figure 3.7: A diagram showing the order in which the top peaks are convolved in the peak-finder algorithm. In (a), the original SNR_A spectrum for the up- and down-sweep portions of the LFM waveform for three radar targets. In (b), the first convolution convolves the top SNR_A peak in each of the up- and down-sweep SNR_A spectra. All other SNR_A peaks are suppressed. In (c) the second largest SNR_A peaks are convolved with all other peaks suppressed. In (d) the smallest SNR_A peaks are convolved with all other SNR_A peaks suppressed.

indicated the possibility of four radar targets. Inspecting the SNR_A spectra in Figure 3.3 revealed that only two radar targets were present, however. As discussed in Section 3.1.1 and shown in Figure 3.4, the two-BW sweep technique failed to distinguish the real radar targets properly. The peak-finder technique was applied to the same radar scattering event and is shown in Figure 3.8. The two spectral ghost targets present in Figure 3.4 were eliminated by the peak-finder technique. The range-Doppler map in Figure 3.8 shows two radar targets at ranges and Doppler frequency shifts that were equivalent to the two real radar targets in Figure 3.4. The additional thin strip of spectra to the left of the two radar targets in Figure 3.8 is again a spectral ghosting issue, but it is easily identifiable as such. This suggests that the peak-finder technique is susceptible to error; however, it is an evidential

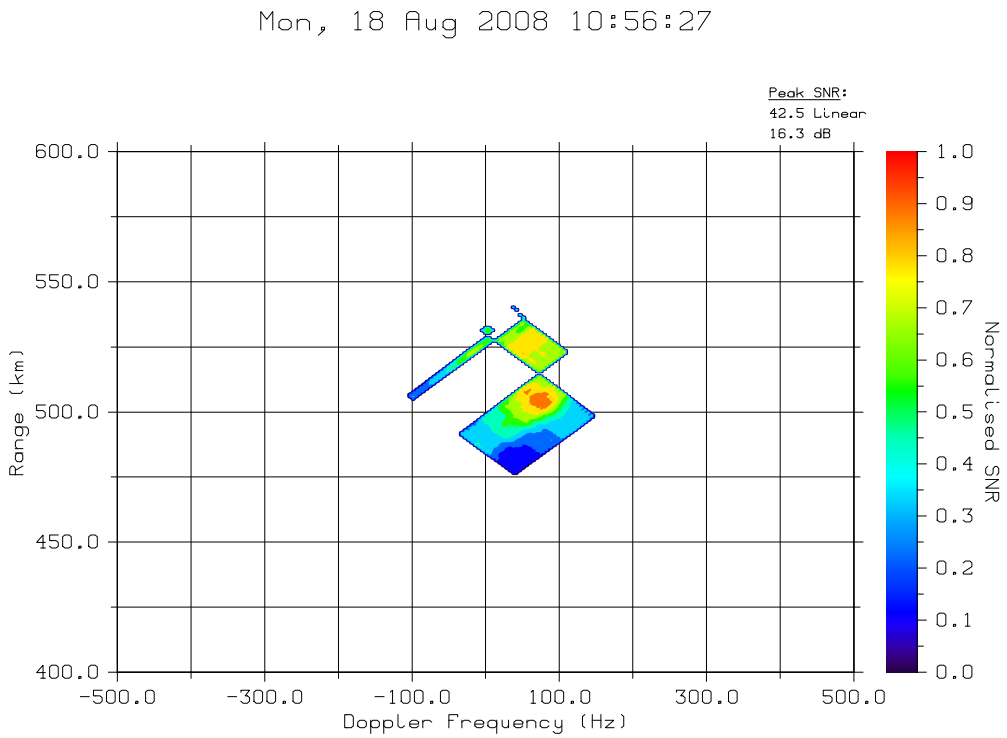

Figure 3.8: A range-Doppler map of a radar scattering event from 10:56:27 UT on August 18, 2008. This range-Doppler map was created from the SNR_A spectra in Figure 3.3 using the peak-finder technique.

improvement over the two-BW technique.

The configuration of multiple radar targets in Figure 3.4a and the effectiveness of the peak-finder technique was regularly observed with the FMCW system, but was not predominant. Although the peak-finder solution was a marked improvement on the two-BW sweep technique, as it was able to distinguish real and ghost radar targets where the two-BW technique could not, it was not robust enough to be consistent for all multiple-target radar events. For this, a more-complex radar analysis program beyond the peak-finder technique presented here is needed. Nonetheless, this current improvement allows for even more data analysis. Furthermore, as will be outlined in Chapter 4, such an analysis technique is not necessary or the best approach to solving this problem as other techniques, such as more advanced waveform techniques, may be employed to avoid spectral ghosting completely.

3.3 Refined SNR_A Calculation

Recall from Section 2.3 that the value of the variable $Noise$ in Equation 2.24 was sampled from a portion of the bandwidth in which no E-region radar signal was expected. Further inspection of data processed using the value of $Noise$ revealed that an additional portion of bandwidth could be used to provide a more representative value of $Noise$. From observation, relevant FMCW scatter occurred in a smaller bandwidth than the 2000 to 4800 Hz range chosen by *Cooper* [2006]. The majority of the measured SNR_A spectra for radar targets detected by the FMCW system rarely had peaks located higher than 4500 Hz, even though the bandwidth allowed for ranges up to 4800 Hz. A more representative sampling of ambient noise across the entire bandwidth is possible if sampling is performed outside of the original bandwidth chosen by *Cooper* [2006].

The FMCW system experienced both systematic and random noise. Sources of systematic noise were the commercial power grid and 1/f, or flicker, noise originating from electrical components in the radar system [*Cooper*, 2006; *Eaves and Reedy*, 1987]. The random noise encountered by the FMCW system was predominately due to sky-noise. In general, noise encountered by the FMCW system was dominated by systematic noise in the frequency range of 0 to 1000 Hz.

Occasionally variations in the systematic noise caused the noise levels to become significant near 1500 Hz — the frequency range used to determine $Noise$, although it would fall-off significantly by 2000 Hz. This may give an over-estimation of $Noise$ (see Section 2.3 and Equation 2.24), culminating in the suppression of backscatter signal. It was determined therefore that modifying the value of $Noise$ by sampling in the range of 4550 to 4800 Hz, in addition to a portion of the frequency range used by *Cooper* [2006] (1750 to 2000 Hz), may provide a more representative value of noise since that range is less prone to noise-induced signal fluctuations and more capable of counteracting radar signal suppression due to the over-estimation of $Noise$. The sampling range of $Noise$ was changed to the ranges of 1750 to 2000 Hz, as well as

4550 to 4800 Hz.

Even though the 4550 to 4800 Hz range experiences less noisy signal, it is a frequency range where E-region radar signal is expected and which equates to a range of 921 to 993 km (assuming an echo with no Doppler frequency shift); however, E-region signal was rarely measured above 4500 Hz and so it is safe to assume that an over-estimation of $Noise$ due to an E-region backscatter signal would rarely occur. It is important to note that due to a recent relative increase in geomagnetic activity there does seem to be an increase in radar echoes being detected with frequency ranges in excess of 4000 Hz.

A comparison of data analyzed using both values of $Noise$ showed a remarkable improvement in the detection capabilities of the FMCW system with the modified value of $Noise$. In some scattering events analysis using the modified value of $Noise$ was able to detect radar echoes tens of minutes before the analysis using the former version of $Noise$ could. There were also several instances where the analysis using the improved value of $Noise$ detected additional radar echoes in scattering events where the old value of $Noise$ could not. Overall, the effectiveness of modifying the frequency range used to sample for $Noise$ provided improvement on the detection capabilities of the FMCW system.

Summary

The analysis techniques presented in Sections 3.2 and 3.3 provide a measurable improvement to the FMCW system. The ability of the FMCW analysis to detect and eliminate spectral ghosting was improved with the peak-finder technique. Furthermore, the value of $Noise$ in the SNR_A calculation in Equation 2.24 was modified. A direct result of this is the improvement of the FMCW system detection capability.

It is imperative to note that with these solutions the FMCW system is an improved system, and it is still an effective and valuable tool for E-region coherent backscatter study; however, the solutions to the problems discussed, although rea-

sonably satisfactory, are not ideal. In the case of the peak-finder technique, it is not fool-proof, as it does not address the overall data association problem attributed to the cause of spectral ghosting (see Section 2.3.1). It only presented an improved technique of working around it. More elaborate analysis techniques may be applied to resolve the data association problem, but ultimately they may not be successful or even possible.

The best approach to solving the spectral ghosting problem is to employ more advanced radar waveform techniques, which allow for the range and Doppler frequency information to be extracted from a single data-set thereby avoiding a data association problem. Over the history of E-region radar studies, many different radar waveforms have been used with varying degrees of success. An alternate waveform for use by the FMCW system for the investigation of E-region plasma processes was investigated for this project, and it is presented in the next chapter.

Chapter 4

Waveform Solutions

This chapter presents some options that may be used to replace the LFM waveform transmitted by the FMCW radar system. A large variety of radar waveforms exist; however, not all are suited for the same application [*Rihaczek*, 1969]. Radar waveforms are customized to the application to which they are applied. Parameters such as range resolution, Doppler velocity resolution and hardware capabilities must be considered when choosing an appropriate waveform for any radar system and application. In this chapter four parameters are presented and discussed in detail to outline the selection of an appropriate radar waveform for the FMCW radar system. In addition, a novel concept design of a continuously active radar system is given.

4.1 Continuous Wave and Pulsed Radars

A radar system is either a Continuous Wave (CW) system or a pulsed system. A CW radar system is defined as a system that transmits a radar waveform that is continuous, meaning the waveform duration, T, is infinite. A pulsed radar system, on the other hand, transmits a discrete radar waveform with a relatively short duration, typically referred to as a pulse. Examples of a CW and a pulsed radar system are the SAPPHIRE [*Koehler et al.*, 1997; *Ortlepp*, 1994] and the SuperDARN [*Greenwald et al.*, 1995] radar systems respectively. Both the SAPPHIRE and the SuperDARN radar systems have been developed and utilized at the University of Saskatchewan. The FMCW system is considered a CW system, and some hardware from the now discontinued SAPPHIRE radar system were used in the construction of the FMCW

system [*Cooper*, 2006].

Both the discrete pulse and CW radar waveform offer unique parameter characteristics, which are desirable to E-region radar research applications. A pulsed radar waveform offers precise control of range resolution. The discrete length of a Tx pulse allows for the round-trip time interval between transmission and reception to be definitively measured. Modifications to the pulse duration are relatively simple, and they allow for a conveniently modified range resolution. If a high range resolution radar system is desired, a pulsed system is exclusively used. The nature of the pulsed system causes a restriction on temporal resolution, however. With a finite amount of time between pulses, a pulsed system may not be able to resolve characteristics of the scattering region that vary quickly in time (as is typically observed in the E region), since the discrete sampling by the pulses may be unable to resolve the changes. This can be a disadvantage for studying E-region scattering and plasma processes.

A pure CW system provides constant illumination (constant sampling) of the scattering region resulting in excellent temporal resolution. This is due to the lengthy waveform duration, which can be described as an infinite pulse duration. However, the large pulse duration degrades the ability of a CW system to provide comparable range resolution to that of a pulsed system. In fact, a pure CW system transmitting at a constant carrier frequency is unable to provide any range information, since the absence of any individual change acting as a timing mark in either the time or frequency domain prevents any measurement of a time duration. The differences between the spatial and temporal resolution of a discrete and CW radar waveform highlight a trade-off that is frequently encountered when comparing pulsed and CW systems: either excellent spatial or excellent temporal resolutions are provided, but not both. There are exceptions to this, of course, including the FMCW system by *Cooper* [2006].

Both pulsed and CW radar waveforms will be investigated since each waveform offers spatial and temporal resolutions that are desirable for E-region studies. Cur-

rently, the FMCW radar system uses a CW waveform in the form of the LFM waveform; however, as outlined in Chapter 2, the FMCW system uses the triangular LFM technique which has inherent to it a data association problem when multiple radar targets are present. As mentioned at the end of the last chapter, analysis techniques to resolve the data association problem are challenging, but a change in the waveform can be much more practical. A pure CW waveform is not suitable for the FMCW system either. As pointed out by *Cooper* [2006], the mono-static set-up and the lack of Tx and Rx isolation in the FMCW radar system prevents a pure CW waveform from being employed. The same justification is used to temporarily rule out a non-linear CW style waveform, similar to that used by *Lind* [1999] for the MRR system (see Section 2.4.2). In that case a mountain range was required to provide the appropriate isolation between the Tx and Rx hardware. We therefore now focus on pulsed radar waveforms.

4.2 Pulse Waveform Parameters

A pulse radar waveform is characterized by a number of unique parameters. Those relevant to this work include: pulse duration t_b, pulse repetition frequency (PRF), uniqueness duration (UD) and waveform duration T. These parameters dictate the overall characteristics and performance for any pulse radar system; however, these parameters are irrelevant without considering what the application of the radar system actually is. Aspects such as scattering region properties as well as expected range and Doppler velocities must be taken into account when selecting a radar waveform [*Rihaczek*, 1969]. As such, theoretical parameter specifications are frequently adjusted to accommodate the environment under which the waveform is implemented. The pulse parameters discussed in the subsequent sections, which are required to create a pulsed radar waveform with similar capabilities to the FMCW waveform, are summarized in Table 4.1. Table 4.1 also summarizes the Valensole radar system which is a pulsed HF radar system used for multi-wavelength E-region studies

Parameter	FMCW Waveform	Composite Costas Waveform	Valensole Radar
t_b	—	20 μs	145 μs
T	213 ms	200 ms	15 ms
PRF	—	—	66.6 Hz
UD	213 ms	200 ms	15 ms
ΔR	970 m	3 km	22 km
Δv	14.1 m/s	15 m/s	8.7 m/s
R_{alias}	31,950 km	30,000 km	2250 km
f_{alias}	—	—	$\pm$ 33.3 Hz

Table 4.1: A summary of the FMCW radar range and frequency resolution along with the range and frequency alias properties and the parameters of the FMCW waveform and the candidate Composite Costas Waveform presented in Section 4.4.1. The properties of a traditional pulse radar waveform used by the Valensole HF radar system is shown as well [*Six et al.*, 1996].

[*Six et al.*, 1996]. Details with respect to these pulse parameters will be discussed throughout this chapter.

4.2.1 Pulse Duration

Pulse duration, t_b, is the duration of a pulse transmission. For a pulsed system t_b is of significant importance as it is directly related to the range resolution of the system. For a constant frequency pulse the range resolution ΔR (co-located Tx and Rx) is determined by (Equation 2.19)

$$\Delta R = \frac{ct_b}{2}, \tag{4.1}$$

where c is the speed of light and t_b is the pulse duration.

E-region processes are spatially dynamic and a radar waveform with high (good) range resolution is desirable. From Equation 4.1, it is evident that the pulse duration for a pulse waveform, must be on the order of $t_b = 6.5$ μs to provide a range resolution

of ΔR = 975 m, which is essentially equivalent to the 970 m of the FMCW system [*Cooper*, 2006]. With respect to radar hardware capabilities (which is discussed in Section 4.5), a 3 km range resolution may be more readily implemented by a pulsed system. In this case, a pulse duration of $t_b = 20$ μs would be required. A waveform with this range resolution is labeled as *Composite Costas Waveform* in Table 4.1.

4.2.2 Waveform Duration

Waveform duration, T, is the total length of the radar waveform and is typically the length of time over which the Rx radar signal is sampled. T is primarily determined by the digitization hardware of the radar system. In fact, the only condition on T is that it must be greater than or equal to the uniqueness duration of the radar waveform, which will be discussed shortly. In the case of the FMCW system, T is a product of the inverse of the sampling frequency and the number of samples required for the Fast Fourier Transform (FFT) performed in the analysis procedure. The FMCW waveform duration T is determined by the sampling frequency of 9600 Hz [*Cooper*, 2006], and the use of 2048 samples for the FFT and so T = 2048/9600 = 213 ms. Furthermore, for the FMCW system

$$\Delta f = \frac{1}{T}, \tag{4.2}$$

where Δf is the frequency resolution of the radar signal and T is the waveform duration for an up- or down-sweep. This is equivalent to the AF definition of frequency resolution in Equation 2.20. For the FMCW radar system, T = 213 ms and accordingly the frequency resolution of the FMCW radar system is 4.69 Hz [*Cooper*, 2006].

4.2.3 Pulse Repetition Frequency

Pulse repetition frequency (PRF) is the number of pulses transmitted per second in a radar waveform. A waveform with a PRF of 500 Hz equates to a system that transmits a pulse every 2 ms. PRF is an important pulsed system parameter since

every pulse radar system has encountered velocity aliasing due to the PRF of the radar waveform used.

Velocity Aliasing

If the PRF of the waveform is equivalent to the velocity of a radar target then the respective spectral peaks will be co-located in frequency space and therefore the peak corresponding to the radar target will be masked. This is one form of velocity alias known as a *blind speed* [*Skolnik*, 1990].

Another velocity alias linked to the PRF of the radar waveform occurs if the Doppler frequency shift of the radar target exceeds the PRF of the radar system. This second alias occurs due to the periodicity of the frequency spectrum. The spectral peaks from the PRF and a given Doppler frequency shift will repeat in frequency space with a periodicity. A Doppler frequency shift that is less than the PRF will be unambiguous since the PRF is constant and well known; however, if a Doppler frequency shift and a corresponding peak in frequency space is larger than the PRF it is then not clear as to whether the corresponding frequency is simply greater than the PRF or less than the PRF but has re-appeared due to the periodicity of the frequency spectrum.

The two velocity aliases described can be avoided as long as the PRF of the radar system has at least twice the magnitude of an expected Doppler frequency shift [*Skolnik*, 1990]. For the 50 MHz system, plasma instabilities in the E region were observed to produce Doppler frequencies as large as $\pm$ 300 Hz [*Cooper*, 2006]. With a CW waveform, the FMCW system was able to avoid velocity aliasing altogether since a CW waveform does not have a PRF; however, for a pulsed system the PRF is required to be 600 Hz at the very least to avoid a velocity alias. This would correspond to having no more than 1.66 ms separating consecutively transmitted pulses. The maximum alias-free Doppler frequency shift is labeled as f_{alias} in Table 4.1.

4.2.4 Uniqueness Duration

Uniqueness Duration (UD) is the length of time over which a radar waveform is considered completely unique. For example, the UD for the LFM waveform used by the FMCW system was 213 ms as that was the amount of time that elapsed for a single-sweep triangle waveform to sweep over bandwidth B. The UD for the Manastash Ridge Radar system (see Section 2.4.2) was at least 10 μs since the carrier frequency, f_c, of the CW signal varied in a highly non-linear fashion such that it was considered unique for any duration longer than 10 μs [*Lind*, 1999]. The UD parameter is important to a radar system since it determines the range aliasing properties of a radar waveform. It is important to note that the UD and T parameters are not equivalent even though they can have the same value.

Range Aliasing

The FMCW system has a field-of-view of 415 to 993 km in line-of-sight range [*Cooper*, 2006]. The long UD of the FMCW LFM waveform allowed for all radar echoes observed in this range to be alias free. A range alias is an ambiguity in the distance to a radar target and occurs due to the repetitiveness of a radar waveform. A range alias occurs if the round-trip time of the radar signal to a target is longer than the UD of the Tx radar waveform. If this occurs, the apparent delay for the round-trip time to the radar target will appear shorter than the actual delay, by a time equivalent to the UD, due to the periodicity of the radar waveform. This is equivalent to the statement that since a sinusoid is periodic $\exp(j\omega t) = \exp(j\omega t + 2\pi m)$ where $\mathrm{j} = \sqrt{-1}$, ω is some angular frequency, t is time and m is an integer. Since the round-trip propagation time for a target distance of 993 km is much less than the 213 ms UD, the FMCW system was range alias free for that distance. Note that the alias free range for the FMCW system could be up to 31,950 km as stated in Table 4.1, but the sampling bandwidth of the FMCW system of 9600 Hz (see Section 4.2.2) limits it to 993 km as stated in Table 1.1 and Section 2.3. In one operating mode,

the Valensole HF radar system [*Six et al.*, 1996] transmitted a radar waveform that had a UD of 15 ms which prevented range aliasing from occurring before 2250 km. The round-trip range over which a radar signal is alias free is given as,

$$R_{alias} = \frac{c\ \mathrm{UD}}{2}, \tag{4.3}$$

where R_{alias} is the alias free range and UD is the uniqueness duration of the signal [*Skolnik*, 1980]. To maintain the alias free range capability of the FMCW system, Equation 4.3 suggests that a pulsed radar waveform must be unique over a period of at least 6.66 ms to prevent range aliasing before a range of R = 993 km. There are different methods and techniques available that can construct unique pulsed radar waveforms over an arbitrary period of time allowing for a desired UD to be achieved. All of these techniques involve some form of varying of a specific waveform parameter in a unique or non-linear fashion over the duration of the signal. These techniques are discussed in Section 4.3.

4.3 Unique Pulse Radar Waveforms

Section 4.2 established a couple of scenarios for the basic waveform parameters required to create some pulse waveforms with resolution properties similar to the FMCW system and therefore useful for E-region studies. Values for pulse duration t_b, waveform duration T, PRF and UD were established; however, how the parameters are implemented together to create a radar waveform with a UD of at least 6.66 ms needs to be determined. In Section 2.2 it was shown that every radar waveform has a corresponding AF and AD, that describe the performance characteristics of the waveform. Using the AF and AD, complex radar waveforms which compliment the requirements outlined in Table 4.1 can therefore now be created with the use of well established waveform design techniques. The goal is to create a radar waveform with range and Doppler frequency resolutions suitable for E-region radar observations (equivalent to those of the FMCW system if possible) that displays good target resolution. Ideally, we wish to create a unique pulse waveform that will

display a thumbtack AD profile.

A method to quantitatively describe how well a given radar waveform approaches the thumbtack AD profile is provided by quantifying the amount of AD volume placed at the origin compared to the total volume within the total AD region. Here, the total AD region is defined to be within the waveform duration along the delay axis, τ/t_b, and the first 10 frequency resolution cells along the frequency axis, $\nu N t_b$. A property of the AD is that all of the possible delay ambiguity volume (that which appears along the delay axis) for a given waveform will appear within this defined region along the delay axis. Theoretically ambiguity along the frequency axis is not as restricted since any Doppler frequency shift is possible; however, for the waveforms presented, a negligible amount of ambiguity appears outside of the 10 cells along the frequency ($\nu N t_b$) axis.

A thumbtack profile is one in which as much AD volume is placed at the origin $|\chi(0,0)|$ as physically possible (see Section 2.2.1). The ideal AD profile is a Dirac delta function, but this would be un-physical and therefore not all of AD volume can be placed at the origin and some of it must spread out in the range-Doppler plane. In practical terms most of the AD volume is outside the thumbtack profile, but the thumbtack is significantly more pronounced than anything else in the range-Doppler plane. The higher the ratio of AD volume at the origin for a given radar waveform compared to the volume within the defined region near the origin, the more effective the radar waveform is at providing a thumbtack-like AD profile. This ratio is denoted $\chi_{\%}$ and is defined as the ratio of the AD volume at the origin to the total AD volume within the full delay axis and 10 frequency resolution cells (the same area which is plotted in the majority of ADs in this thesis).

Three techniques which can be used to create unique pulse waveforms are: PRF staggering, phase coding and frequency coding [*Levanon and Mozeson*, 2004a; *Rihaczek*, 1969]. PRF staggering departs from the constant PRF of classic pulse waveforms. Phase coding involves varying the pulse-to-pulse phase of the waveform based on a pre-determined sequence. Frequency coding is similar to phase coding; however,

carrier frequency is the parameter which is changed from pulse-to-pulse. Although these techniques serve a common purpose, not all are suitable for application with the FMCW radar system: all three techniques require modifications to the FMCW system hardware. Each technique will be discussed in the context of the observation of E-region plasma processes and implementation with the FMCW system.

4.3.1 PRF Staggering

The PRF is a parameter that describes the amount of pulse transmissions per second and determines the velocity aliasing properties of a pulse radar waveform. Typically, the PRF of a radar sequence is a constant value. *Rihaczek* [1969] points out; however, the PRF need not be a constant value and may be staggered to create a unique pulse sequence, which can be used to combat range aliasing. This is clear if one recalls that range aliasing is a function of the UD, as discussed in Section 4.2.4. If the PRF is constant, range aliasing will occur according to Equation 4.3; however, if the PRF becomes more variable, the waveform UD increases, and the alias free range for the waveform increases as well. Even though this technique can extend the alias free range (R_{alias}) of a radar waveform, it will not affect the velocity aliasing properties of the waveform. It was discussed in Section 4.2.3 that the PRF of a radar waveform determines the velocity aliasing properties of the waveform. The value of the PRF at any one time must still be taken into account with regard to PRF staggering and velocity aliasing.

An example of the implementation of a PRF staggering technique is provided by the SuperDARN radar system [*Greenwald et al.*, 1983, 1995]. A multi-pulse sequence used by the SuperDARN system produced an alias-free target range on the order of 3000 km. A pulsed system with a constant PRF could only achieve an equivalent alias free range by transmitting a pulse every 20 ms. This value corresponds to a PRF of 50 Hz which indicates that the system will encounter aliasing for any Doppler frequencies above $\pm$ 25 Hz. This low alias value is too low for auroral E-region plasma observations. The seven-pulse sequence implemented by *Greenwald et al.* [1983] is

Figure 4.1: The seven-pulse staggered PRF sequence used by *Greenwald et al.* [1983]. The vertical axis is the amplitude of the Tx signal and the horizontal axis is the time axis in units of the waveform pulse duration t_b. In this case, T = $480t_b$.

given in Figure 4.1. The vertical axis in Figure 4.1 is the amplitude of the Tx signal while the horizontal axis is the time axis in units of t_b (pulse duration). A pulsed system using the sequence in Figure 4.1 will Tx seven pulses in 48 ms [*Greenwald et al.*, 1983].

Even though the PRF staggering technique is a viable and proven solution, by itself it is not ideal for use with the FMCW radar system. An advantage of using the LFM technique was that transmitting over a bandwidth of frequencies inherently helped reduce noise effects [*Stove*, 1992]. Sporadic noise was usually restricted to a few frequencies and thus would only affect a negligible portion of the bandwidth over which the FMCW system operated. The PRF staggering technique involves a constant carrier frequency transmission. This would degrade the capability of the pulsed waveform to combat noise.

The inability to provide a constant target illumination is another drawback of the

staggered PRF technique. The pulse pattern used by *Greenwald et al.* [1983] transmitted seven, $t_b = 100$ μs, pulses over a period of T = 48 ms. The amplitude diagram in Figure 4.1 clearly shows that the time between pulses (or samples) provided by the seven-pulse sequence, and any waveform with a staggered PRF, is much more than that of the LFM waveform, where a target is constantly illuminated (sampled). This indicates that the temporal resolution for the staggered PRF technique is not as good as the LFM or any CW technique. Although useful for some applications, the PRF staggering technique is not optimal to replace the FMCW LFM waveform for auroral E-region observations.

4.3.2 Phase Coding

Phase coding is a technique used to form a unique pulse waveform by sequencing the phase of each individual pulse. Phase, $\phi(t)$ in Equation 2.1, is a pulse parameter which can be arbitrarily adjusted. Much like how the PRF can be altered to create a unique pulse pattern, the same is achieved with the phase of each individual pulse. This process is referred to as phase coding. Even though an infinite combination of phase coded signals can be realized theoretically, certain specific sequences or combinations have been developed that provide near-ideal sequences. The term near-ideal implies a sequence which generates an AD approaching a thumbtack profile shape and therefore provides good range and Doppler frequency resolution and an absence of range and velocity aliasing.

A *Barker* [1953] code is a binary phase code; that is, a Barker code alternates between two phases separated by $\phi = \pi$. A 13-pulse Barker code, along with its AD, is shown in Figures 4.2 and 4.3 respectively. It is important to note that the units of the AD Doppler frequency axis change for a multiple pulse sequence. Instead of νT, the Doppler frequency axis is changed to $\nu N t_b$ where N is the number of pulses in the sequence. From Figure 4.3, the spike at the origin, with lower peaks in close proximity, indicates that Barker codes are relatively effective at creating a unique waveform. From Figure 4.3 some ridging, similar to that seen in the AD for the LFM

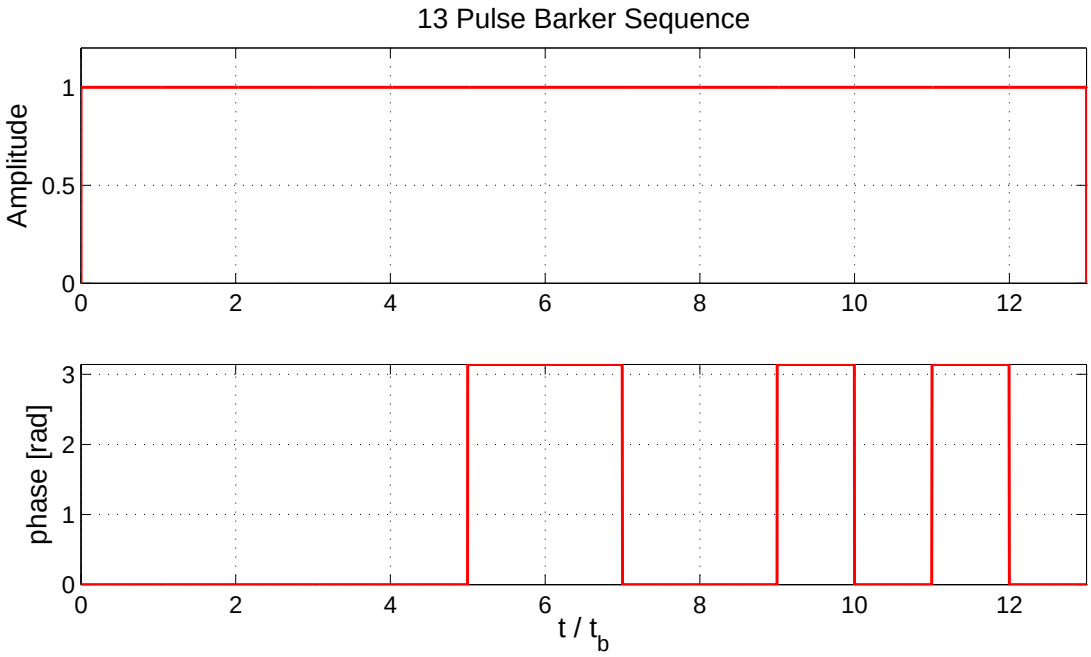

Figure 4.2: A 13 pulse Barker code sequence. The top diagram is the amplitude of the Tx signal as a function of pulse duration t_b. The bottom diagram is the phase of the radar signal as a function of pulse duration.

waveform, is present. The height and close bunching of the ridges and peaks near the origin indicate that a Barker coded waveform may have difficulty with aliasing at lower Doppler velocities and low range separation between radar targets. The ratio measure of AD volume at the origin was calculated for the Barker sequence as $\chi_{\%} = 0.055$ %. This is a low $\chi_{\%}$ value compared to other waveforms discussed shortly. This indicates that the AD does not approximate a thumbtack profile very well.

Barker codes are limited. The longest unique Barker code is 13 pulses in length, which limits the ability to create long and unique pulse sequences. A variation of the Barker code, known as the Frank [*Frank and Zadoff*, 1962] code, is considered a polyphase code as it varies the pulse-to-pulse phase of a radar waveform over multiples of $\phi = k\frac{\pi}{2}$, where k is an integer. Polyphase codes offer a greater pulse sequence variety and have been, and continue to be, implemented in some radar systems including the European Incoherent Scatter Radar (EISCAT) Svalbard radar (ESR)

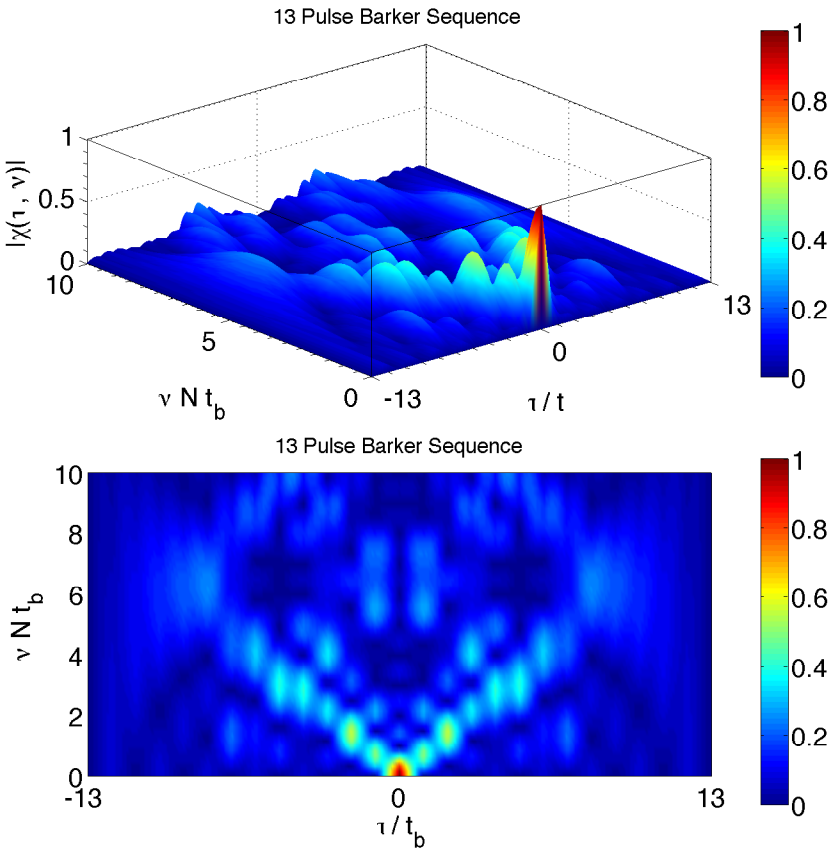

Figure 4.3: The AD for a 13-pulse Barker code sequence. The top AD indicates a dominant spike at the origin while the bottom AD, showing an overhead view confirms this. In close proximity to the peak are moderately high spikes and peaks forming an angled ridge out from the origin. This ridging indicates some possible range and Doppler velocity ambiguities.

system [*Wannberg et al.*, 1997]. With the improved variety provided by polyphase codes, multiple codes can be put together to create long phase coded sequences. The ESR system used this technique and with it was able to provide highly resolved spatial and Doppler velocity measurements that were comparable to the FMCW system [*Wannberg et al.*, 1997].

Phase coding is a valid method of creating a unique radar waveform for E-region backscatter study. Early on in this research, frequency coding (a technique that will be discussed shortly) was chosen as a method for constructing unique radar pulse sequences rather than phase coding. This does not indicate an inferiority in the phase coding technique. Future research into phase coding for E-region observations

is encouraged, but is not considered further in this thesis.

4.3.3 Frequency Coding

The carrier frequency ω_c in Equation 2.1 is another parameter that can be varied from pulse to pulse to create a unique radar waveform sequence. Like phase coding, varying carrier frequencies of the individual pulses is referred to as frequency coding. Frequency coding is a popular and flexible waveform technique and is demonstrated in Figure 4.4 where the frequencies of sequential pulses are varied in a linear fashion. The bottom plot in Figure 4.4 illustrates the frequency evolution of the radar signal. The vertical axis in the bottom figure in Figure 4.4 has normalized units of frequency fNt_b, where f is the frequency, N is the number of pulses in the waveform and t_b is the pulse duration. The corresponding AD in Figure 4.5 shows peaking diagonal ridges similar to the LFM waveform ridge as shown in Figure 2.5. The AD in Figure 4.5 points to range-Doppler coupling, which was encountered with the LFM waveform. This is not surprising, however, since the two waveforms are similar in that they both employ a linear carrier frequency variation.

By definition, frequency coding creates a radar waveform that is transmitted over a bandwidth which gives the radar system a resistance to sporadic noise. This is one marked improvement over other radar waveforms that only Tx at a constant carrier frequency. The capability of a frequency coded signal to reject noise increases as the number of frequency pulses and the variety of frequencies transmitted increases [*Levanon and Mozeson*, 2004a].

Binary Matrix

An effective way to describe a frequency coded waveform is by describing the coding sequence using a binary matrix [*Levanon*, 1988; *Levanon and Mozeson*, 2004a]. An example of a binary matrix is provided in Figure 4.6. A binary matrix is a square matrix wherein each column represents a waveform pulse duration, t_b, and each

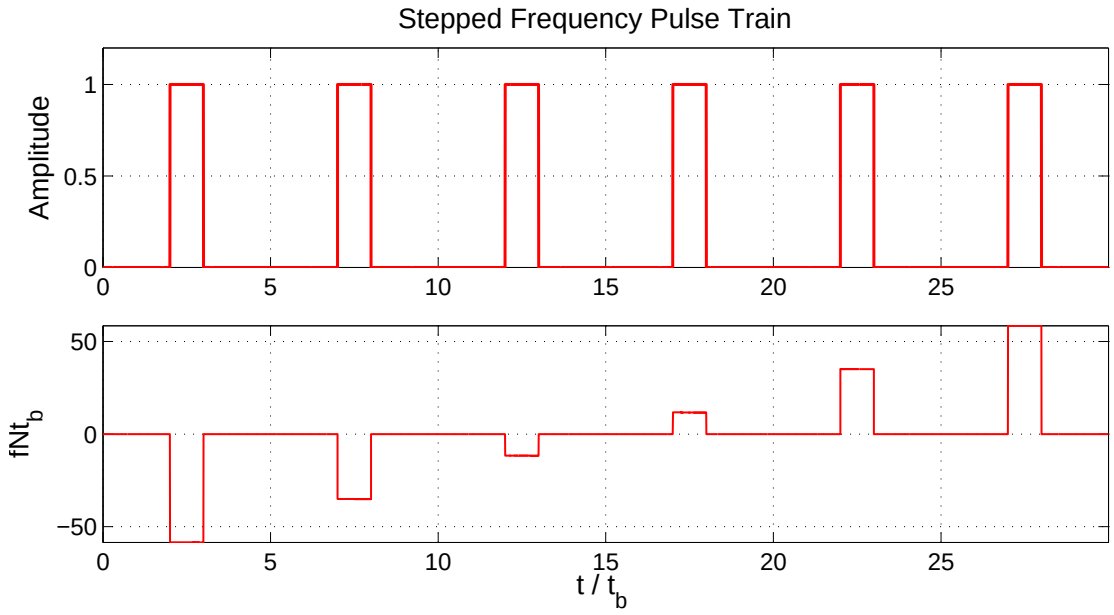

Figure 4.4: A linear frequency coded pulse sequence. The top plot indicates the amplitude of the radar signal as a function of pulse duration t_b. The bottom plot is of the waveform frequency as a function of pulse duration as well.

row represents a precise carrier frequency, f_c, at which a pulse is transmitted. A Tx radar pulse is shown as a red-bar, as illustrated in Figure 4.6, and a Rx radar pulse is shown as a blue-bar. *Levanon* [1988]; *Levanon and Mozeson* [2004a] comment that an approximation to the AD for a frequency coded sequence is made if a binary matrix is over-laid with a copy of itself. To represent a radar echo event, a blue-bar binary matrix is laid over a red-bar binary matrix as shown on the right in Figure 4.6. To represent a time delay (range to target) and a Doppler frequency shift, the over-laid matrices are simply offset from one another along the time and frequency axes. In Figure 4.6 the two Tx-Rx binary matrices, representing a linearly coded waveform, are over-laid and offset by one row and one column value. This describes a time delay and Doppler frequency shift equivalent to t_b and Δf, respectively. Points at which two bars coincide are referred to as coincidence points and represent an AF value (or volume in the AD). The right diagram in Figure 4.6 shows six coincidence points along the main diagonal of the over-laid matrices. This indicates six closely spaced (six consecutive adjacent rows and columns which have coincidence points)

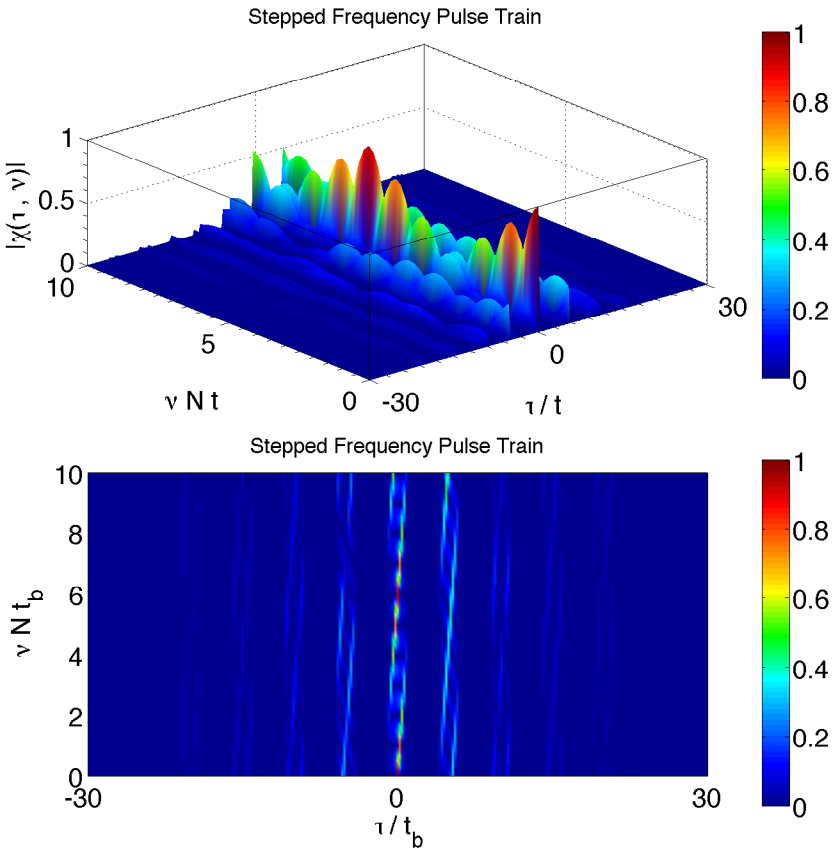

Figure 4.5: The AD for a linear frequency coded pulse sequence. The large diagonal ridges in both the normal view and over-head view (bottom) show similarities to the AD of the LFM waveform in Figure 2.1.

correlation values, or six closely spaced peaks in the AD diagram. As the number of matrix entries increases, they will better approximate a FMCW signal and thus the appearance of a diagonal ridge, such as that featured in an LFM waveform in Figures 2.5 and 4.5, is expected [*Levanon*, 1988; *Levanon and Mozeson*, 2004a]. The $\chi_{\%}$ value of the linear frequency coded pulse waveform is relatively high at $\chi_{\%} = 0.390$ % which indicates that its corresponding AD approaches a thumbtack profile. Here it is important to inspect Figure 4.5 when considering the $\chi_{\%}$ value. Although the $\chi_{\%}$ value is relatively high, it only describes how well AD volume is placed about the origin and does not detail how the volume is spread out on the range-Doppler plane in regions other than near the origin. In Figure 4.5 near $\nu N t_b = 6$, there are Doppler frequency aliases with magnitudes that are nearly

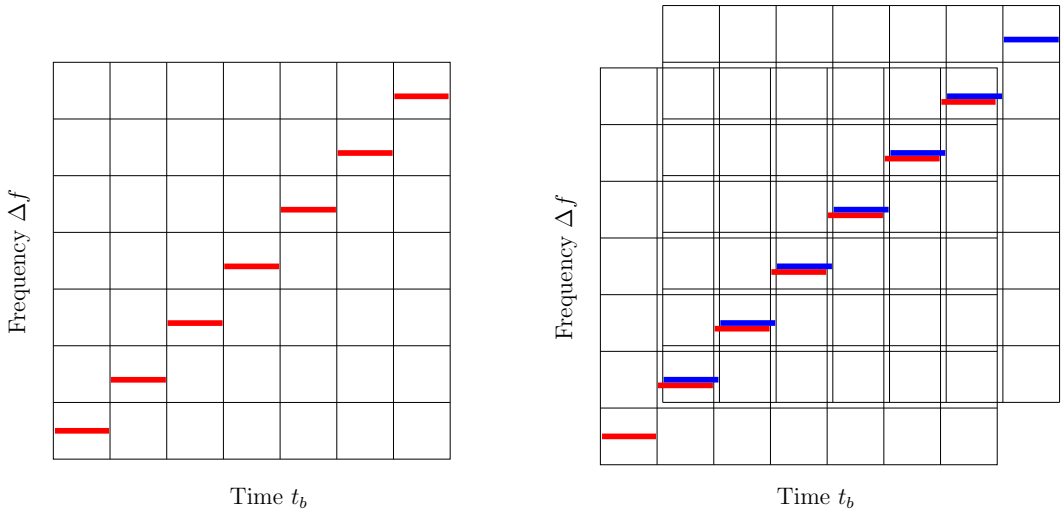

Figure 4.6: A binary matrix for an linear frequency coded waveform. The row and column entries of the matrix coincide with the discrete frequency and duration of an individual pulse. A Tx signal is represented by a red-bar (left) and a blue-bar denotes a Rx radar signal. A Tx and Rx matrix are over-laid and offset to represent a radar echo event (right).

equivalent to the AF values at $|\chi(0,0)|$. This is discussed further in Section 4.4.1.

As with phase coding, a large number of frequency coded sequences are possible and, idealized frequency coded sequences designed to produce a thumbtack AD profile exist. In an effort to disassociate the coincidence points in Figure 4.6, the order of the sequence can be changed and once again over-laid with a shifted copy of itself, as in Figure 4.7. With the altered sequence fewer coincidence points exist. A trend develops: as the sequence in Figure 4.6 becomes more non-linear as demonstrated in Figure 4.7, fewer coincidence points occur. It is expected that as a sequence becomes highly non-linear the number of coincidence points will minimize to one and the AD of the corresponding frequency coded waveform will approach the thumbtack profile indicating an ideal sequence.

The shifts in Figure 4.7 show only a few offsets, and a sequence producing a single coincidence point for a matrix offset does not guarantee an equivalent result for all other offsets, in general. *Costas* [1984] investigated the properties of frequency coded sequences and developed a class of sequences, known as Costas sequences, that produce only a single coincidence point for all possible binary matrix offsets.

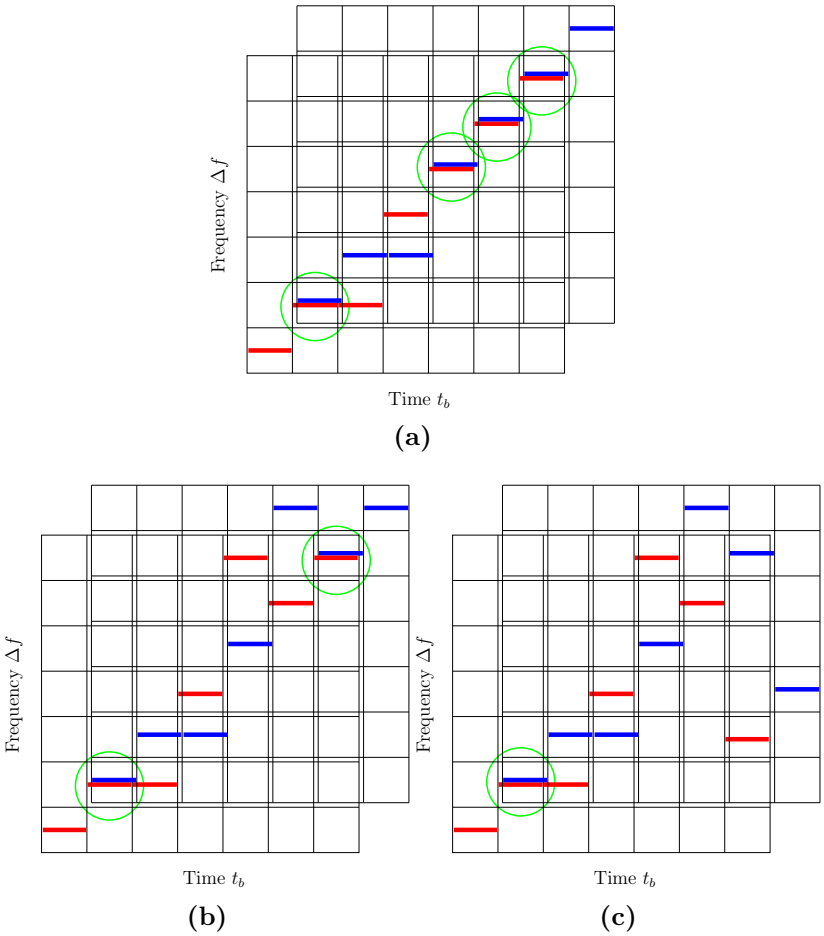

Figure 4.7: A sequence of three binary matrices demonstrating the transformation of the linear signal in Figure 4.6 to a non-linear one. The combinations in (a) and (b) have four and two coincidence points while the variation in (c) has a single coincidence point, as shown by the green circles.

Frequency coded waveforms derived from Costas sequences are known as Costas Waveforms or Costas Coded Waveforms.

4.4 Costas Waveforms

The ability of a Costas sequence to create a unique waveform may be demonstrated with the use of binary matrices. When a binary matrix representing a Costas sequence is over-laid with copy of itself and offset by any non-trivial value at most only a single coincidence point occurs. This is the definition of a Costas sequence

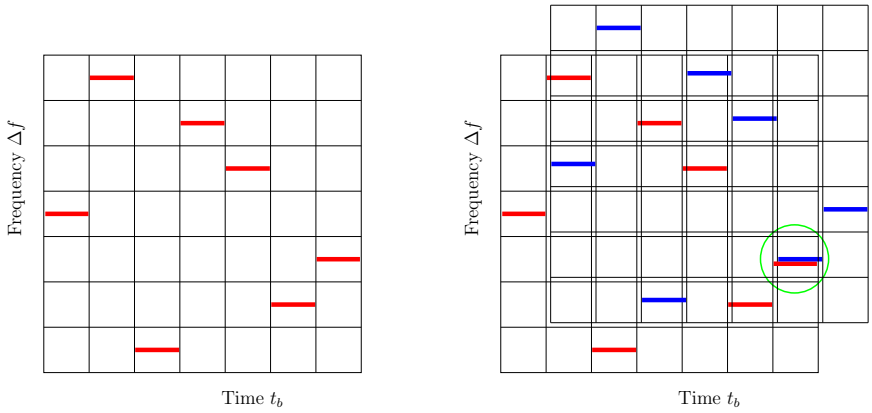

Figure 4.8: A binary matrix representing a 7^{th} order Costas sequence (left). A radar echo event for the same Costas sequence (right). Notice the single coincidence point and the amount the red and blue bars are dispersed as compared to the single coincidence point in Figure 4.7c.

[*Levanon*, 1988; *Levanon and Mozeson*, 2004a]. A seventh-order Costas sequence with the corresponding binary matrix is shown in Figures 4.8 and 4.9.

The Costas sequence is useful since a single coincidence point for over-laid binary matrices corresponds to a single isolated correlation value, which is approximated by a spike or a thumbtack profile in the AD. The property that at most one coincidence point occurs for any non-trivial shift along t_b or Δf indicates that each coincidence point is represented by a unique shift in t_b and Δf. Extrapolating this to a radar event, each range and Doppler frequency cell is uniquely represented, and therefore a radar waveform based on a Costas sequence is alias free in both range (t_b) and Doppler frequency shift (Δf).

Figure 4.9 presents the frequency evolution for the 7^{th} order Costas sequence as a function of time. The corresponding Costas ACF and AD are given in Figure 4.10 and 4.11 respectively. The well isolated peak at the origin in both Figures 4.10 and 4.11 indicates the ability of the Costas sequence to provide a waveform with a thumbtack AD profile. Note in Figure 4.10 the first *side-lobe* of the ACF (not to be confused with antenna radiation pattern side-lobe terminology) is down ~ 15 dB, which corresponds to an AD value of ~ 0.18 in Figure 4.11. Furthermore, in Figure 4.11 there are no ridges throughout the entire range-Doppler plane, and any ambiguity volume is well

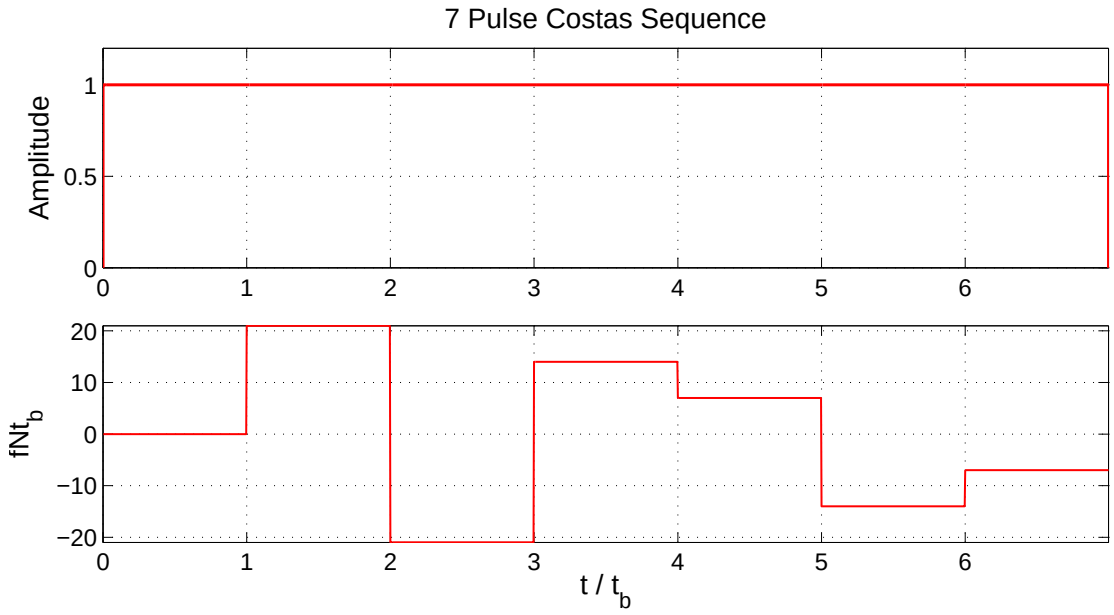

Figure 4.9: An amplitude diagram (top) and frequency evolution diagram (bottom) for a 7^{th} order Costas sequence.

suppressed when compared to Figures 4.3 and 4.5. This is quantitatively supported by the higher value of $\chi_{\%} = 0.081$ % compared to the Barker code. The absence of any ridging or peaks anywhere near the spike at the origin indicates an immunity to range and Doppler velocity aliasing.

A Costas sequence is dependent on the spacing between the Tx frequencies. As mentioned earlier, the rows of a binary matrix represent the discrete Tx frequencies. For a Costas sequence to maintain its AD properties, it is imperative that the frequency spacing is described by

$$\Delta f = \frac{1}{t_b}, \tag{4.4}$$

where Δf is the frequency spacing and t_b is the pulse duration. If Equation 4.4 is not met, the AD diagram for the associated waveform will not display a thumbtack profile. In fact, any large variation in frequency spacing will result in an accumulation of ambiguity volume in close proximity to the thumbtack profile, resulting in a susceptibility to range and Doppler velocity aliasing [*Levanon and Mozeson*, 2004b].

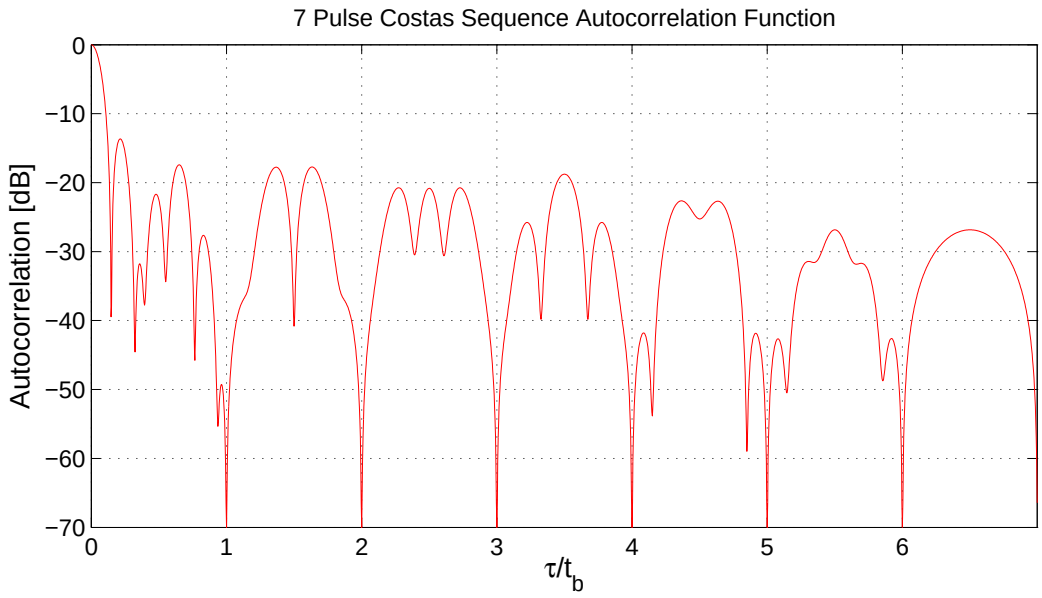

Figure 4.10: The ACF for a seventh-order Costas sequence.

Costas Sequence Research

For a binary matrix of order M, there are M! different unique sequences possible; however, not all sequences are Costas [*Levanon and Mozeson*, 2004a]. Recall that the definition of a Costas sequence is one which, when represented as a binary matrix, produces at most one coincidence point for all non-trivial offsets from its initial position [*Levanon and Mozeson*, 2004a]. There are 7! = 5040, unique combinations of frequency-hopped sequences for a binary matrix of 7^{th} order, but only 200 of these unique sequences are Costas by definition [*Levanon and Mozeson*, 2004a]. Research is on-going into determining all possible Costas sequences. The search for Costas sequences was performed manually by *Costas* [1984] for orders $M \leq 12$. Since then, the search for Costas sequences has become an area of research for discrete mathematics and computational methods. Currently, all possible Costas sequences up to order M = 27 are known and some, but not all, sequences up to order M = 300 are known [*Drakakis et al.*, 2008; *Rickard et al.*, 2006; *Drakakis*, 2006; *Golomb and Taylor*, 1984].

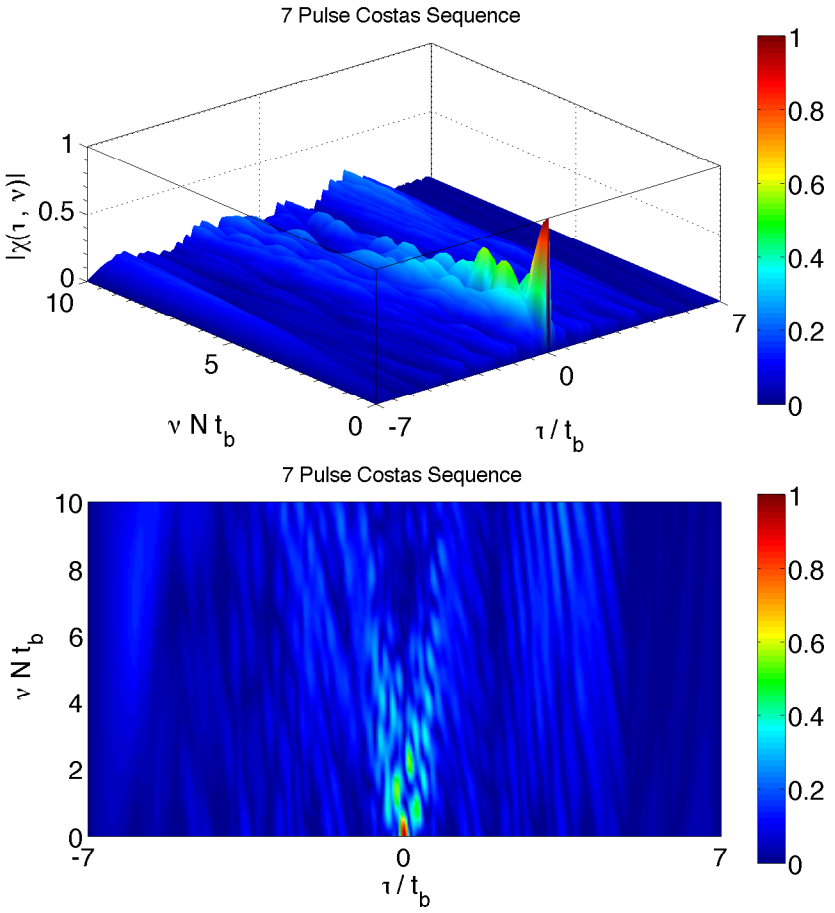

Figure 4.11: The AD for a 7^{th} order Costas sequence. The top AD shows a well isolated spike at the origin with no large ambiguity peaks in close proximity. The over-head view (bottom) further indicates the isolation of the spike.

In-depth research into Costas sequences has indicated an upper limit on the number of unique Costas sequences as the order M increases [*Levanon and Mozeson*, 2004a]. In addition to this, there is uncertainty as to whether or not Costas sequences exist for all M [*Drakakis*, 2006]. This becomes evident if the number of Costas arrays is plotted against the Costas order. This is provided in Figure A.1 in the appendices.

This result is of particular relevance to this research. The UD condition established in Section 4.2.4 requires the construction of a pulsed waveform that is unique over a length of time of at least 6.66 ms. Even though the UD condition is 6.66 ms, according to Equation 4.2 the waveform duration T must be longer than the UD in

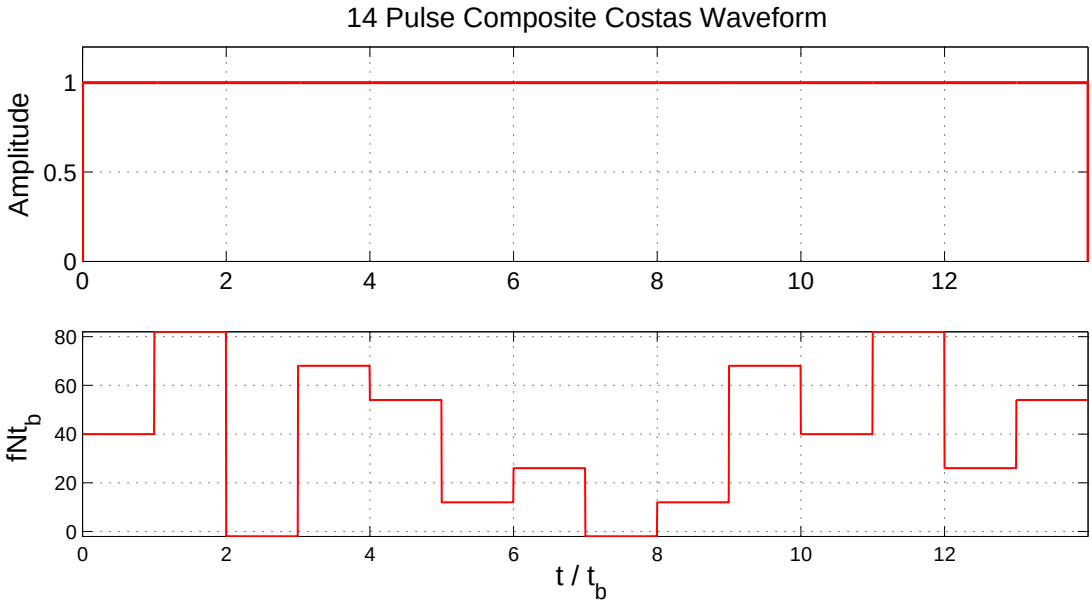

Figure 4.12: An amplitude diagram (top) and frequency evolution diagram (bottom) for a 14^{th} order composite Costas waveform. The waveform is constructed from two different 7^{th} order Costas sequences.

order to achieve the desired frequency resolution of 4.69 Hz as in the current FMCW waveform. If a radar waveform is CW based (e.g. a Costas waveform), has a UD of 6.66 ms and a waveform duration of 213 ms (or any duration greater than the UD) range aliasing will occur. To avoid the aliasing and to supply a $\Delta f = 4.69$ Hz, both the UD and waveform duration T must be equivalent to 213 ms. To achieve this, a sequence of contiguous pulses, each with length $t_b = 6.5$ μs (20 μs) and of order M = 32769 (10650) is needed. This is a value far exceeding any order, M, known to contain a Costas sequence; therefore, a method to modify a Costas sequence into a form which produces a similar AD, and which also satisfies the UD and Δf condition, is required.

4.4.1 Composite Costas Waveforms

Freedman and Levanon [1986] investigated the properties of pulse sequences composed of multiple Costas sequences. In their work, it was determined that constructing a pulse sequence from multiple Costas sequences resulted in a near-thumbtack

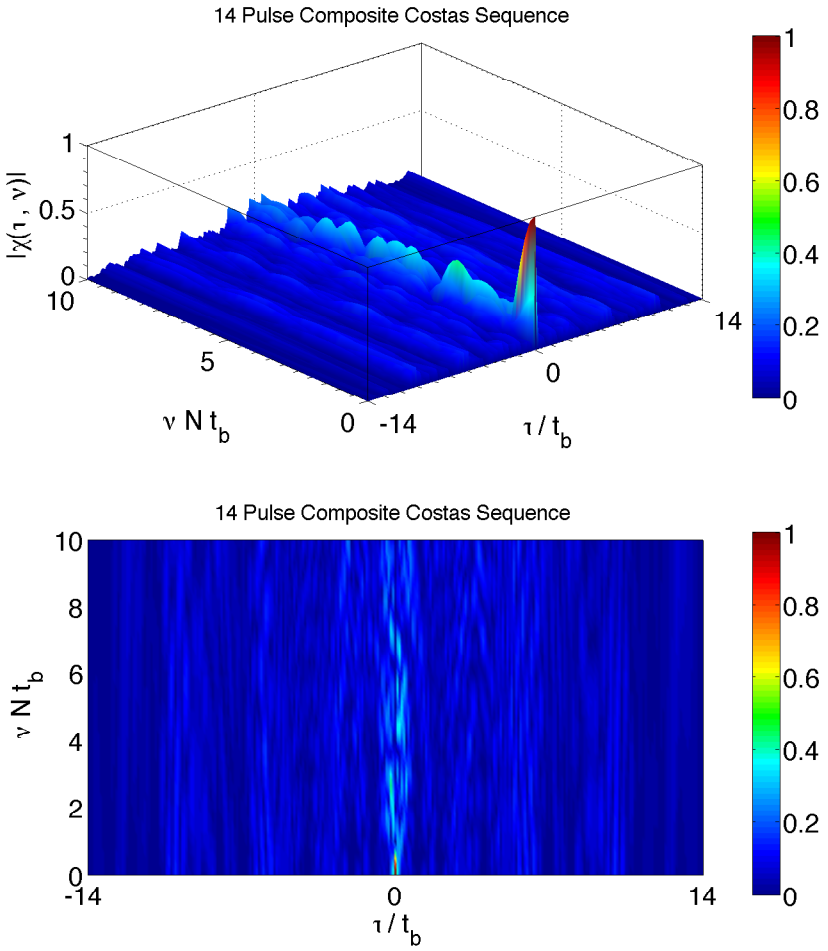

Figure 4.13: The AD for a 14^{th} order composite Costas waveform. The waveform is constructed from two different 7^{th} order Costas sequences. From the top diagram, it is evident that a well isolated peak at the origin remains, even though the waveform is not purely Costas. The isolation of the peak at the origin is highlighted by the over-head view (bottom).

AD profile. Figure 4.12 provides the frequency evolution and Figure 4.13 shows the AD for a composite 14-pulse duration sequence that is constructed from two 7^{th} order Costas sequences. Notice the two 7^{th} order Costas sequences in Figure 4.12 are not similar. The AD for composite waveform of order 35 constructed from five 7^{th} order Costas sequences is shown in Figure 4.14. In both Figures 4.13 and 4.14 the tell-tale spike at the AD origin is prominent. On top of this it is evident that the ambiguity volume found close to the spike in Figure 4.11 is suppressed in Figure 4.13 and even more so in Figure 4.14. This is consistent with the property that any sec-

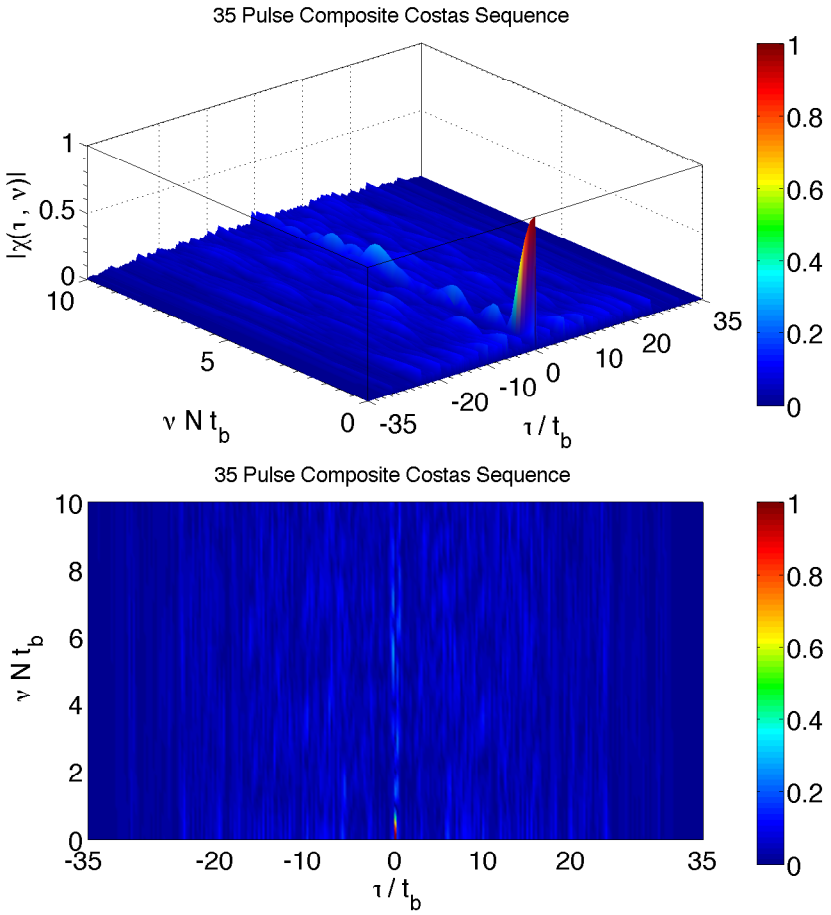

Figure 4.14: The AD for a 35^{th} order composite Costas waveform. The waveform is constructed from five different 7^{th} order Costas sequences. The top view and over-head view (bottom) show an even more isolated spike than Figures 4.11 and 4.13 due to the larger pulse sequence order.

ondary peaks in the AD, or ACF, will be suppressed as $\sim 1/M$ as the order M of the Costas pulse sequence increases [*Freedman and Levanon*, 1986]. In addition to this, as the order of the composite Costas sequences increases as the $\chi_{\%}$ value increases — the 14^{th} order Costas waveform increases $\chi_{\%}$ to 0.108 % (Figure 4.13) and the 35^{th} order Costas waveform increases $\chi_{\%}$ to 0.163 % (Figure 4.14). This suggests that as the order of the composite Costas sequence increases the corresponding AD diagram better approaches a thumbtack profile.

Candidate Replacement Waveform

A composite Costas pulse sequence of any large order M can maintain a near thumb-tack ambiguity profile. From *Levanon and Mozeson* [2004a], 6464 known unique Costas sequences exist for order M = 20; thus, frequency hopped radar pulse sequence consisting of 32780 pulses from 1639, 20^{th} order Costas sequences can be constructed. Such a waveform will have a UD and waveform duration, T, of 213 ms for 6.5 μs pulses (ΔR = 975 m), satisfying the UD requirement and giving a Δf = 4.69 Hz (the current FMCW waveform parameters). However, as mentioned previously it may be more technically feasible to implement a waveform with a longer pulse duration, and therefore consisting of less pulses in a pulse sequence. Furthermore, due to bandwidth implications (which will be explained shortly), it is easier to implement a waveform based on a 10^{th} order Costas sequence, of which there are 2160 unique sequences [*Levanon and Mozeson*, 2004a].

A Costas sequence for 20 μs pulses (ΔR = 3 km) consisting of 10,000 pulses from 1000, 10^{th} order Costas sequences will have a UD of 200 ms. This sequence will again satisfy the UD condition thus avoiding range aliasing and will supply a Δf = 5 Hz. This frequency resolution is essentially the same as that of the FMCW system. A major benefit of using a composite Costas waveform is that any frequency resolution or UD condition can be satisfied by selecting the appropriate number of pulses in the sequence. A 10,000 pulse composite Costas waveform sequence is given in Figure 4.15 along with the corresponding ACF in Figures 4.16 and 4.17. The waveform is also detailed in Table 4.1 as the *Composite Costas Waveform*. It is difficult to display a clear plot of the entire 10,000 pulse waveform sequence so the waveform sequence in Figure 4.15 shows a view of pulses 2500 to 2600. The non-linearity of the sequence in Figure 4.15 is evident when compared to Figure 4.4.

The well suppressed ACF of the candidate composite Costas waveform, presented in Figures 4.16 and 4.17, indicates the ability for the composite waveform to avoid any range aliasing. The ACF side-lobes in Figure 4.16 are below ~ -18 dB. The AD of the waveform (not shown) further illustrates the complete absence of ambiguity

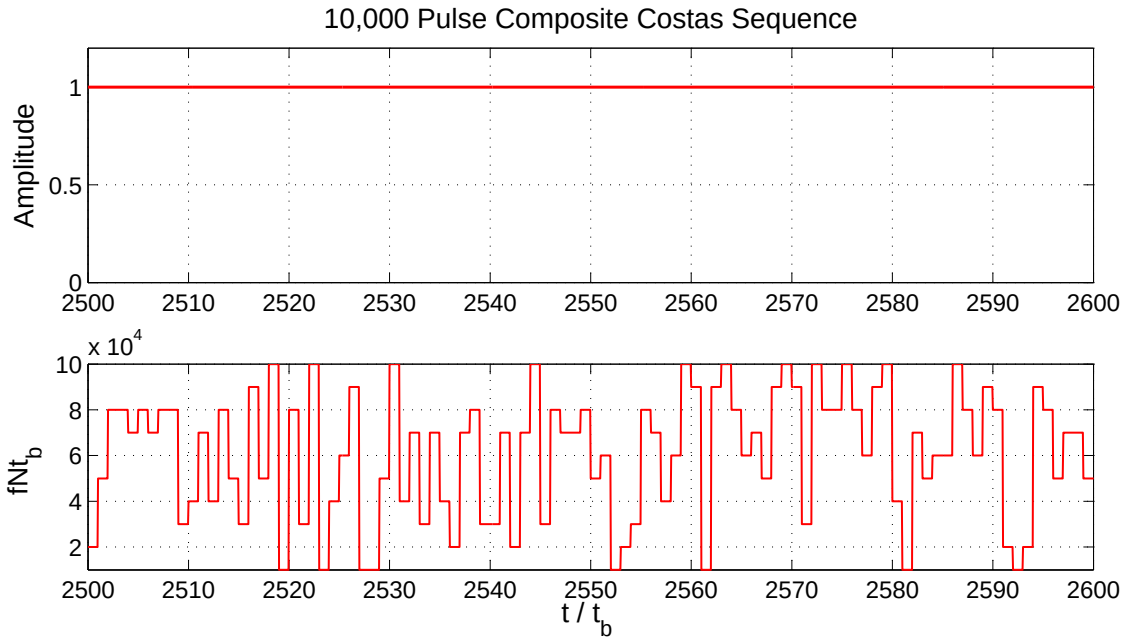

Figure 4.15: A frequency evolution diagram showing pulses 2500 to 2600 in the 10,000 pulse composite Costas sequence constructed from 1000 10^{th} order Costas sequences.

anywhere across the range-Doppler plane. This is supported by the $\chi_{\%}$ value for the proposed composite Costas waveform, which is the highest thus far at $\chi_{\%} = 0.93$ %. Table 4.2 summarizes the $\chi_{\%}$ values of all of the presented waveforms. The AD for the proposed composite Costas waveform is essentially the thumbtack profile. If a single radar target is represented by the AD profile of the candidate composite Costas waveform, then it is evident that multiple targets superposed at different Doppler frequencies and ranges across the $\tau - \nu$ plane would be easily resolvable. The AD of the composite Costas waveform will therefore provide excellent range and Doppler frequency resolution as well as excellent target resolution.

Due to the multitude of various array combinations we are not restricted to a 10^{th} order Costas sequence. For example, if a designer wished to degrade the range resolution (as we have already done from 970 m to 3000 m), which is accomplished by increasing t_b (from 6.5 μs to 20 μs), the designer still has many options for a Costas based waveform design. The waveform could be altered to be composed of

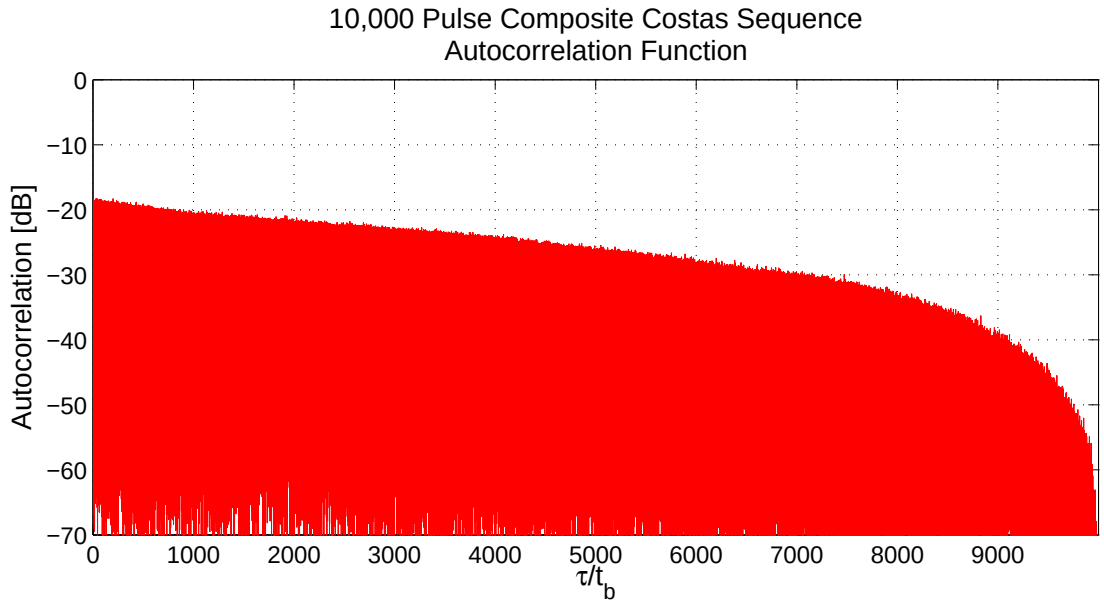

Figure 4.16: The ACF for a 10^{th} order, 10,000 pulse composite Costas waveform.

834 12^{th} order Costas sequences (UD,T = 200 ms) or 770 13^{th} order Costas sequences (UD,T = 200 ms). Furthermore, design parameters such as Tx bandwidth restriction can be accommodated by using a lower ordered Costas array. This was considered when selecting the 10^{th} order Costas sequence over a 20^{th} order sequence. Equation 4.4 describes the bandwidth required for a Costas coded waveform. If a radar system is restricted in bandwidth, a Costas sequence can be selected based on Equation 4.4 to satisfy the restrictions. A bandwidth range for a Costas waveform sequence is $M\Delta f$, where M is the number of pulses in the sequence [*Levanon and Mozeson*, 2004a]. With this in mind, a Costas sequence can then be constructed to stay within any bandwidth restrictions imposed on the radar system. A composite Costas waveform can be tailored to meet the other desired UD, range and Doppler frequency resolution parameters. Table A.1 shows the number of Costas arrays for each order N, and Figure A.1 is a plot of the number of Costas array versus order N. These are provided in Appendix A. From Table A.1 it can be seen that there are many options available in the design of a Costas based radar waveform.

A radar waveform based on the composite Costas sequence is a candidate for use

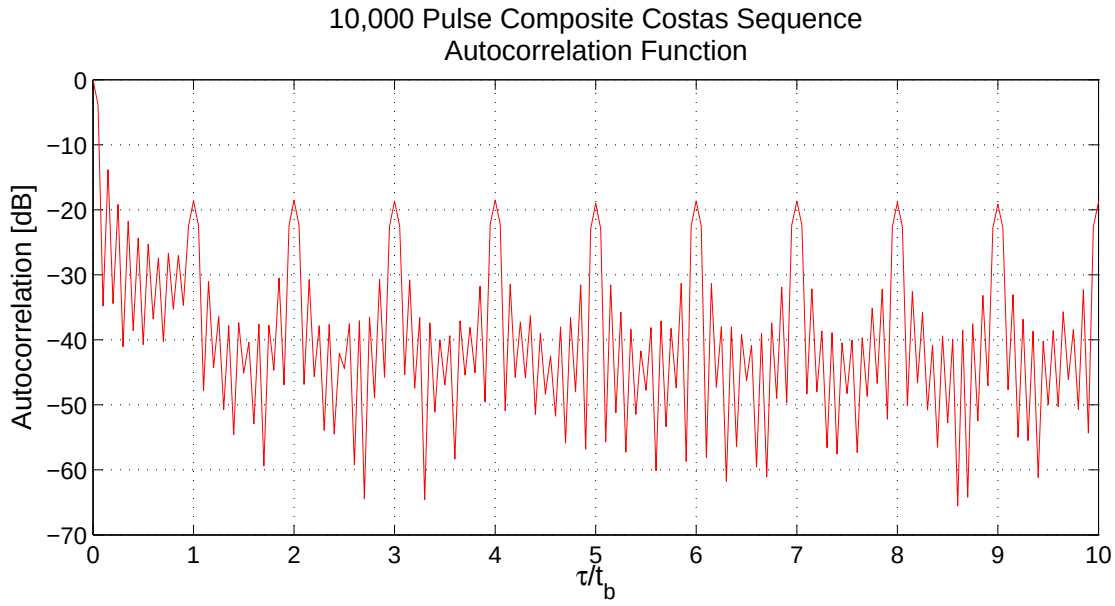

Figure 4.17: A closer view of the ACF for a 10^{th} order, 10,000 pulse composite Costas waveform presented in Figure 4.16. The ACF remains suppressed for larger values of τ as well.

by the FMCW radar system. A composite Costas waveform is alias free in both range and Doppler velocity, and it can provide the appropriate spatial and velocity resolutions comparable to the capabilities of the FMCW system. It would be ideal to implement a composite Costas waveform that could provide range and Doppler frequency resolutions that are equivalent to the FMCW system using the LFM waveform technique; however, this is not practical due to hardware and implementation restrictions. In general though, any implementation of a composite Costas waveform would require hardware modifications. The feasibility of implementing a composite Costas waveform with the FMCW system is discussed in the next section.

Table 4.2 provides the $\chi_{\%}$ value, range resolution ΔR and frequency resolution Δf for all waveforms investigated in this thesis as well as the ideal case of a Dirac delta spike. In Table 4.2 ΔR for the pulse sequences (e.g. Linear Coded Pulse, Costas waveforms and proposed Composite Costas Waveform) is calculated as a function of the speed of light c and the pulse duration t_b. For the LFM waveform, ΔR is calculated as a function of the bandwidth B over which the LFM waveform sweeps.

Radar Waveform Type	$\chi_{\%}$ (%)	ACF side-lobe (dB) suppression	ΔR (m)	Δf (Hz)
Square Pulse	0.067	-1	$\frac{ct_b}{2} = 3000$	$\frac{1}{t_b} = 50000$
LFM	0.071	-1	$\frac{c}{2B} = 3000$	$\frac{1}{T} = 5$
Linear Coded Pulse	0.390	-10	$\frac{ct_b}{2} = 3000$	$\frac{1}{6t_b} = 8333$
13^{th} order Barker	0.055	-22	$\frac{ct_b}{2} = 3000$	$\frac{1}{13t_b} = 3846$
7^{th} order Costas	0.081	-18	$\frac{ct_b}{2} = 3000$	$\frac{1}{7t_b} = 7143$
14^{th} order Costas	0.108	-17	$\frac{ct_b}{2} = 3000$	$\frac{1}{14t_b} = 3751$
35^{th} order Costas	0.163	-15	$\frac{ct_b}{2} = 3000$	$\frac{1}{35t_b} = 1429$
Proposed Composite Costas	0.930	-18	$\frac{ct_b}{2} = 3000$	$\frac{1}{10000t_b} = 5$
Dirac delta	100	$-\infty$	0	0

Table 4.2: A summary of the $\chi_{\%}$ values, the ACF side-lobe suppression values, the range resolution ΔR and frequency resolution Δf for the radar waveforms discussed in this thesis. In all pulsed waveform cases $t_b = 20$ μs was used and for the LFM case B = 50,000 Hz was used. The $\chi_{\%}$, ΔR and Δf values for a Dirac delta spike is also provided.

For all of the waveforms in Table 4.2 the frequency resolution Δf is calculated as the inverse of the waveform duration T. For the pulse sequences, $T = Nt_b$ where N is the number of pulses within the entire waveform. The side-lobe suppression of the ACF outside of the first range resolution cell along the delay axis, expressed in dBs, for the corresponding radar waveform is also provided in Table 4.2. This is to show that a higher $\chi_{\%}$ corresponds to a lower ACF value outside the first range resolution cell and thus a more suppressed AD profile in general. A more suppressed ACF profile indicates that the AD volume has been better restricted to a region near the AF origin and the AD volume is not as spread out in the range-Doppler plane.

The $\chi_{\%}$ parameter lacks the ability to describe how a given radar waveform distributes its AD volume throughout the $\tau - \nu$ plane and so the parameter must not be solely used to characterize the AF. The AD remains the most effective tool to describe how AD volume is distributed on the range-Doppler plane. The limitation

of the $\chi_{\%}$ parameter is revealed with the linear frequency coded pulse waveform. For this waveform $\chi_{\%} = 0.390$ % which is the second highest value in Table 4.2 and its ACF side-lobe suppression value outside of the first range resolution cell is -10 dB. This suggests that the AD profile of the linear coded pulses sequence is approaching a thumbtack-like profile, but inspection of the AD profile given in Figure 4.5 indicates range-Doppler coupling and Doppler frequency aliasing as also suggested by the relatively poor ACF side-lobe suppression value of only -10 dB. The $\chi_{\%}$ parameter can only describe the volume near the origin of the AD and cannot describe how the volume outside of the origin is distributed. For all of the other waveforms in Table 4.2 the AD volume outside the origin is more uniformly spread out in the range-Doppler plane, at near-zero values, as supported by inspection of their corresponding ADs. However, the AD volume outside of the origin for the linear frequency coded pulse waveform has grouped together angled ridges as may be seen in Figure 4.5.

4.5 Hardware Parameters

A radar waveform is limited by the hardware with which it is to be implemented. Even though the parameters of a radar waveform, described earlier in this chapter, have been selected based on applicability for auroral E-region observations, the overall waveform compatibility with electronic hardware must still be considered. Hardware for signal generation and radar antenna configuration are two aspects of particular importance for the FMCW radar system.

4.5.1 Signal Generation

For the FMCW system, the kernel of the signal generation was the Direct Digital Synthesizer (DDS) card. The FMCW control code programmed the LFM waveform parameters into the DDS card, which then created a signal that was amplified and transmitted by the subsequent Tx hardware. Following is a discussion on whether the DDS used by the FMCW system has the ability to be a waveform generator for

a system transmitting the composite Costas waveform described in Section 4.4.

The FMCW used the AD9954 DDS card by Analog Devices [*Analog Devices*, 2009]. The AD9954 card is capable of creating two general waveforms. One waveform is a pulse waveform with constant carrier frequency. The second is an LFM sweep waveform that was used by the FMCW system. The former set-up is clearly best suited for the generation of a composite Costas waveform. The pulse waveform parameters outlined in Section 4.2 must now be considered with regard to the AD9954 card.

To maintain the range resolution of the FMCW system, a train of pulses each with pulse duration $t_b = 6.5$ μs is required. According to the manufacturer, *Analog Devices* [2009], the AD9954 card is capable of producing pulses of shorter durations than $t_b = 6.5$ μs; thus the short pulse duration is achievable. As mentioned previously however, a pulse duration of $t_b = 20$ μs enabling a 3 km range resolution may be more realizable with the FMCW system. Nonetheless, according to the manufacturer the AD9954 is more than capable in either case.

Creating a waveform composed of sequential pulses involves more subtle detail. A frequency-coded, or Costas, waveform can be generated by the AD9954 card using two techniques. The first technique is to re-program the DDS card on a pulse-by-pulse basis for each pulse in the waveform. The second method involves loading the Costas waveform information into the Random Access Memory (RAM) of the DDS card and enabling the DDS to generate the waveform from RAM. Testing determined that re-programming a frequency into the AD9954 requires 400 μs. Using the first method would limit the Costas waveform to at least a 400 μs delay between sequential pulses, or a PRF of 2500 Hz.

The second method provides a much quicker alternative. Creating a waveform from information stored in the AD9954 card RAM allows for a near-seamless transition between frequencies but the RAM is limited in size. As a result, the RAM for the AD9954 is only capable of storing enough information for a four-pulse sequence, much less than the 10,000 pulse composite Costas sequence proposed in Section 4.4.1.

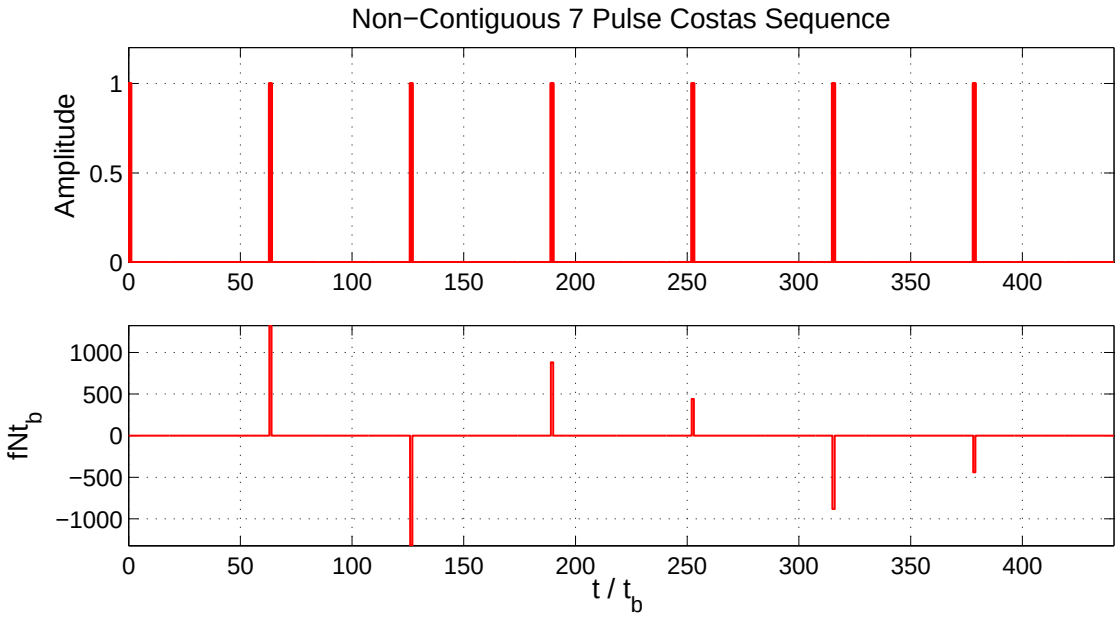

Figure 4.18: An amplitude diagram (top) and frequency evolution diagram (bottom) for a non-contiguous 7^{th} order Costas waveform.

Alternate DDS cards from Analog Devices were researched and the largest RAM available is only able to support an eight-pulse sequence [*Analog Devices*, 2008].

Devices are commercially available which are capable of performing the required frequency transitions to generate any Costas waveform with contiguous pulses. Equipment such as an Arbitrary Waveform Generator (AWG), for example the AWG5000B series by Tektronix [AWG, 2008], is completely capable of generating the 10,000 pulse composite Costas waveform discussed in Section 4.4.1. These devices range in value from $\$30,000 - \$65,000$ in 2010 dollars. A data sheet for the AWG5000B Series by Tektronix is provided in Appendix B.

Contiguous pulses are typically displayed in the manner shown in the bottom plots of Figure 4.9 and Figure 4.12; although the term contiguous, and the property which defines it, is ambiguous and seemingly arbitrary. Even though the graphical representation of Costas waveforms suggest a sequence of contiguous pulses, the literature does not explicitly outline it as a requirement.

As previously mentioned, the AD9954 is capable of re-programming and transmitting a frequency coded pulse at a PRF of 2500 Hz. Using software code provided

by *Levanon and Mozeson* [2004a], the transition from contiguous to non-contiguous pulses with a 2500 Hz PRF was investigated. The pulse sequence and frequency evolution of a 7^{th} order, non-contiguous Costas sequence is shown in Figure 4.18. The ACF for the non-contiguous sequence is given in Figures 4.19a, 4.19b and 4.19c for different intervals along the delay axis τ/t_b. Due to the presence of a PRF, the ACF becomes discontinuous along the delay axis; however, when compared to the Costas ACF in Figure 4.10, the side-lobes of the ACF remain well suppressed. The discontinuous ACF is stretched out over a longer axis than the ACF in Figure 4.10. This is due to the fact that the pulse sequence with a PRF of 2500 Hz is inherently longer in duration than a non-contiguous 7^{th} order sequence. The discontinuous ACF remains below the $-$ 18 dB level (Figure 4.19c) throughout the waveform duration and does not display any unwanted aliasing or other characteristics. The transition from a contiguous to non-contiguous sequence has no drastic effect on the performance of the waveform.

For signal generation, there are two options for the implementation of a composite Costas waveform. One option is to implement the Costas waveform constructed from non-contiguous pulses with the AD9954 DDS card and the second is to construct the waveform using new and sophisticated waveform generation hardware, such as an AWG. The latter option offers high temporal resolution at the cost of high waveform generation complexity. A CW waveform is constructed from contiguous pulses; therefore, the temporal resolution for a contiguous pulse waveform is excellent and equivalent to that of the FMCW system. In contrast, a pulse waveform that is non-contiguous could not offer the same temporal resolution as a CW waveform such as the composite Costas waveform.

Waveform generation for a constant frequency CW or a pulsed radar waveform is relatively simple since numerous variations of each technique have been implemented in the past and are well documented. A CW waveform that does not have a constant carrier frequency, like a Costas coded waveform, is more complex and difficult to implement. There exists an apparent trade-off between waveform capability and system

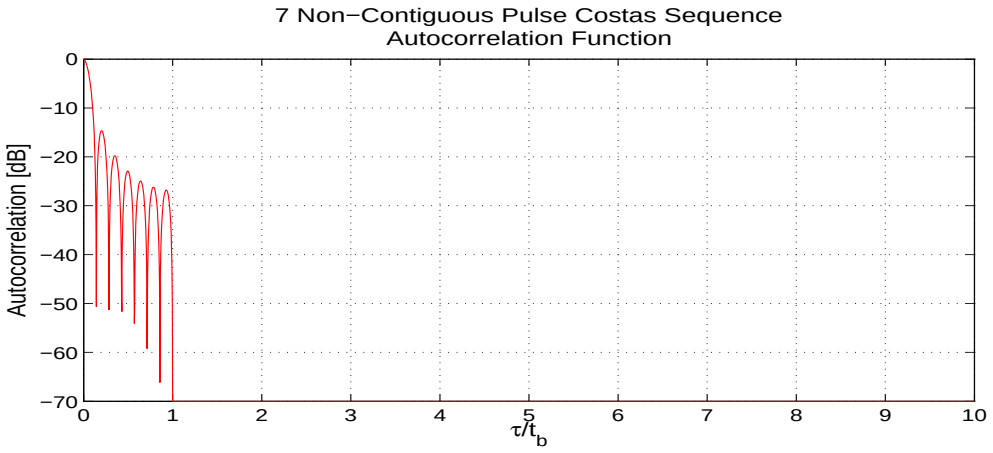

(a)

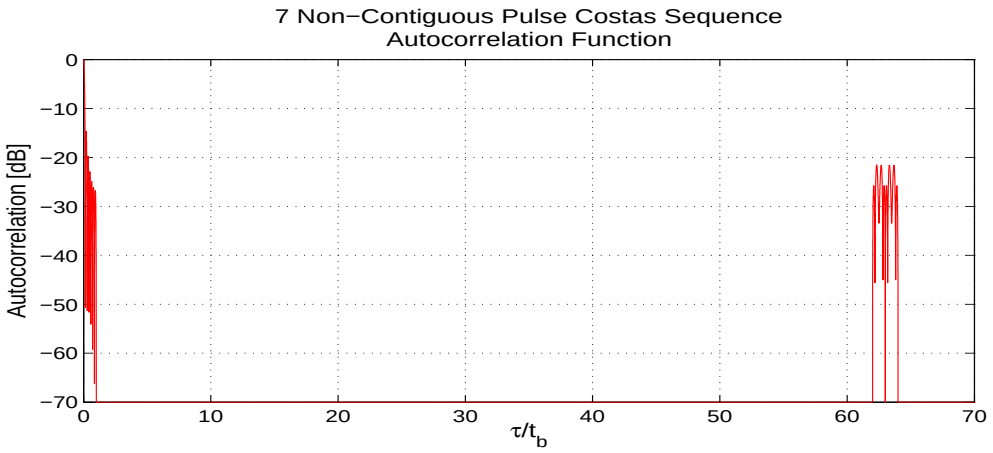

(b)

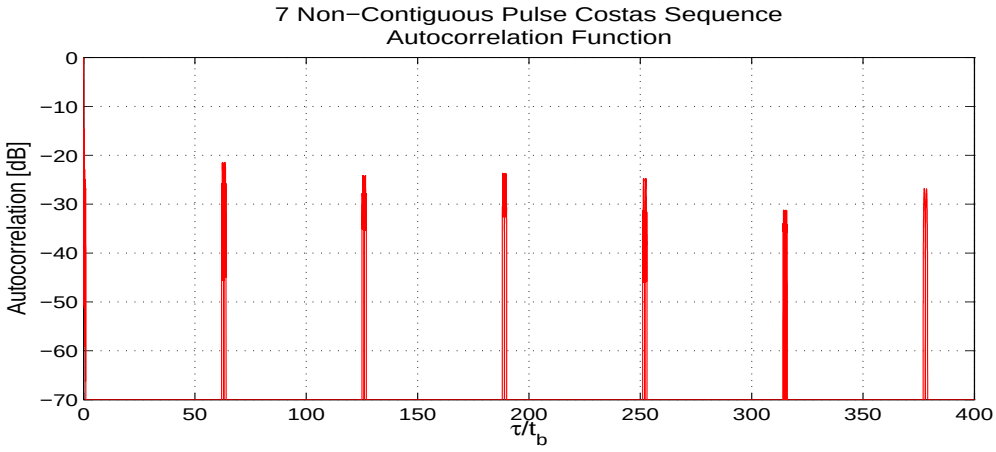

(c)

Figure 4.19: The ACF for a 7^{th} order non-contiguous Costas waveform for a range of τ / t_b from (a) 0 to 10, (b) 0 to 70 and (c) 0 to 400.

complexity as basic waveforms are implemented with basic hardware, and more complex and desirable waveforms require more complex hardware systems. With newer hardware such as AWGs, highly complex waveforms, such as the composite Costas waveform, which provide both high spatial and temporal resolutions, are now more realizable and the hardware/complexity trade-off is effectively eliminated.

4.5.2 Bandwidth

The performance of a Costas waveform is contingent on the frequency spacing between hopped frequencies satisfying Equation 4.4. As outlined in Section 4.2, if $t_b = 6.5$ μs then according to Equation 4.4, $\Delta f = 153.85$ kHz. Any Costas waveform used by the FMCW system must have each individual pulse frequency spaced by $\Delta f = 153.85$ kHz. Furthermore, the overall bandwidth used by the system must be at least that much since the lowest order of a Costas waveform is M = 2. Multiple Costas sequences all with order M = 20 corresponds to an overall bandwidth B = 3.08 MHz. As such, there is a need for a much larger bandwidth than the bandwidth of B = 154.3 kHz used by the FMCW system.

In Section 4.2 it was decided that it may be more feasible to implement a composite Costas waveform with a pulse duration of $t_b = 20$ μs corresponding to a 3 km range resolution. This equates to a frequency spacing of $\Delta f = 50$ kHz and, using the composite Costas waveform of order M = 10, an overall bandwidth of B = 500 kHz. This much smaller bandwidth may be more practical due to reasons of radio licensing and hardware implementations, both of which will be discussed shortly.

The value of B = 500 kHz is also the largest frequency value of the difference signal outlined in the continuously active radar mixing procedure in Section 4.5.5, and therefore this bandwidth will need to be digitized. In order to digitize this signal, it will need to be sampled at a rate that is greater than or equal to the Nyquist frequency, which in this case is 1 MHz [*Brigham*, 1988]. This sampling rate is far in excess of the capability of the hardware employed by the FMCW system [*Cooper*, 2006], so new digitization hardware is required. As discussed in Section 4.2.2, the

waveform duration, T, is dependent on the rate of digitization, and therefore the waveform duration for the proposed composite Costas waveform will vary with the rate of digitization.

With an increased operating bandwidth, focus is placed on the antenna used by the FMCW system. The FMCW antenna array is composed of Cushcraft 617 6B Yagi antennas [*Cushcraft*, 1991]. According to the manufacturer, the antennas are designed to operate between 50 MHz and 51 MHz [*Cushcraft*, 1991]. Tests performed with a spectrum analyzer on the FMCW array indicated that the antennas are capable of a relatively flat response between 48 and 51.5 MHz which encompasses the 500 kHz bandwidth discussed previously.

Any other hardware appearing after or before the antenna in the Tx and Rx chain can be modified to accommodate any increase in bandwidth. The FMCW system Tx amplifiers are designed to handle the range of frequencies that will be experienced with a Costas based waveform. The quick transition between successive frequencies that would be required by a Costas waveform should be manageable as well, since the FMCW system performed quick frequency transitions in the LFM sweeping process without any discernible repercussions. On the other hand, the hardware involved with the Rx system will require major modifications due to increased overall operating bandwidth (e.g. sampling hardware which was previously described). This will not be discussed in more detail, but, it is assumed that any modifications to the FMCW system for the implementation of a composite Costas waveform will not be overly complicated or un-manageable.

In addition to the antennas, the radio license of the radar system must also be considered. The FMCW system was licensed to Tx and Rx for a bandwidth of B = 154.3 kHz between the frequencies 49.42 to 49.58 MHz. A change in operating frequencies must be authorized since implementing a Costas coded waveform requires operation over a much larger bandwidth. Not all frequencies are required in the bandwidth: only those frequencies spaced by Equation 4.4 are needed. Since the separation, Δf from Equation 4.4, between the discrete frequencies of a Costas

waveform is the only waveform parameter that must be adhered to, a Costas waveform is relatively flexible to implement over an increased Tx bandwidth. If for any reason any frequencies in the larger bandwidth are restricted, such as those for radio communications, the Costas waveform can easily be tailored not to Tx at the restricted frequencies. Any other frequency can be selected as long as the separation condition in Equation 4.4 is maintained. It is important to note that at each discrete frequency in the Costas waveform, a ~ 2 kHz (1 kHz above and below the value of the discrete frequency) bandwidth would be required to allow for the expected Doppler frequency shift of auroral E-region echoes, which vary over a $\pm$ 300 Hz frequency range.

Restrictions on the size of the bandwidth used by the system can be accommodated. The flexibility of using composite Costas waveforms allow for the overall waveform bandwidth to be adjusted without any large effect on the overall performance of the waveform (see Section 4.4.1). For example, a 10^{th} order composite Costas waveform was selected instead of a 20^{th} order waveform. As a result, the overall bandwidth required was reduced from 3.08 MHz to 500 kHz. The lower overall bandwidth may be more practical for both hardware and radio licensing purposes. Digital sampling capabilities must be considered with the composite Costas waveform and even though signals with bandwidths up to $\sim$ 200 MHz can be directly digitized, at the time of writing, limiting the overall bandwidth will simplify the implementation of the proposed waveform. The ability to easily accommodate this is a benefit of the large amount of Costas sequences available for use (shown in Table A.1 in Appendix A). Furthermore, when considering radio licensing, a composite Costas waveform is much simpler to work with. Rather than using a 154.3 kHz bandwidth like the FMCW system, a 10^{th} order composite Costas waveform would simply use a total of 20 kHz in bandwidth spread out over the 500 kHz total bandwidth. To implement a Costas waveform, all that would be required is 10 radio licenses, each with 2 kHz bandwidth allocations. As such, it is possible that a radio license for the bandwidth required by a Costas waveform would be granted.

4.5.3 Radar Array Configuration

An important portion of the FMCW radar system that has not yet been discussed is the antenna array configuration. The FMCW system is a mono-static radar: that is, the Tx and Rx antennas are located in the same geographic location. A bi-static system configuration has the Tx and Rx radar arrays in separate geographic locations.

4.5.4 Feed-through

For a CW waveform, a bi-static radar configuration is traditionally used; whereas for a pulsed system a mono-static configuration is used. The difference in antenna array configuration is to avoid feed-through. Feed-through occurs when a radar signal transmits directly to the Rx antenna rather than indirectly via radar backscatter [*Cooper*, 2006]. In a typical mono-static pulse radar system, the Rx antennas are de-activated while the Tx antennas are active. Radar Rx systems are extremely sensitive instruments that are required to detect low power backscatter. In a mono-static configuration, the Rx will be unable to detect the weakly powered radar scatter signal in the presence of the high powered directly fed-through Tx signal. It will also damage the Rx hardware.

There are various techniques to avoid feed-through. SuperDARN and nearly all pulsed radar systems use the aforementioned technique of de-activating the Rx antenna during transmission. The SAPPHIRE radar system used a bi-static configuration and the Tx and Rx systems were separated by a large geographic distance on the order of a 1000 km [*Koehler et al.*, 1995]. The Manastash Ridge Radar (MRR) used a bi-static configuration as well; however, the Tx and Rx hardware were only separated by a short geographic distance and thus a mountain range was required to block any direct transmission between Tx and Rx hardware [*Lind*, 1999]. The FMCW system employs the typical FMCW mixing technique with some slight modifications to the implementation that depart from classic feed-through solutions.

In order to achieve high spatial and temporal resolution using an LFM waveform, the FMCW system must Tx and Rx a radar signal continuously. To prevent feed-through, the FMCW system takes advantage of the digital waveform generation hardware to eliminate feed-through without deactivating the Rx or using a physical barrier between the Tx and Rx antennas. As outlined in Section 2.3, the FMCW system mixes the transmitted LFM waveform with the received backscatter waveform in real-time. This is depicted in Figure 4.20. The Tx signal used by the mixer is provided by a secondary output on the DDS card at [1], whereas the primary output supplies the Tx signal to the antenna array at [2].

A directly fed-through Tx signal along with a weak coherent backscattered signal [3], is mixed with a copy of the Tx signal [1] by the mixer at [4]. Since the directly fed-through signal and the copy of the Tx signal are equivalent, their mixed signal is a DC signal. The backscattered signal and the copy of the Tx signal are mixed to an AC signal (the signal of interest) at [4]. The difference between the backscattered signal and the signal currently being transmitted is caused by the propagation delay introduced by the radar signal traveling to and from the radar target. An additional variation is due to the Doppler frequency shift of the target.

Once the mixing is complete, the output signal of the mixer at [5] has a DC and an AC component. The DC signal power is much larger than the AC signal since it does not undergo a scattering process but travels the direct path between the Tx and Rx antennas only. The DC signal component of the output is simply blocked at [6] by using a coupling capacitor in the post-mixer Rx hardware. The AC signal passes through the coupling capacitor and is subsequently digitally sampled at [7]. The FMCW system demonstrates how feed-through can be avoided without the need to de-activate the Tx and Rx hardware or without implementing extraordinary antenna isolation. This technique can be adapted to other CW waveforms as well but, as tested by *Cooper* [2006], was ineffective for a pure CW waveform.

It is important to note that the technique employed by the FMCW system is contingent on the Tx power as well. The FMCW feed-through technique is effective

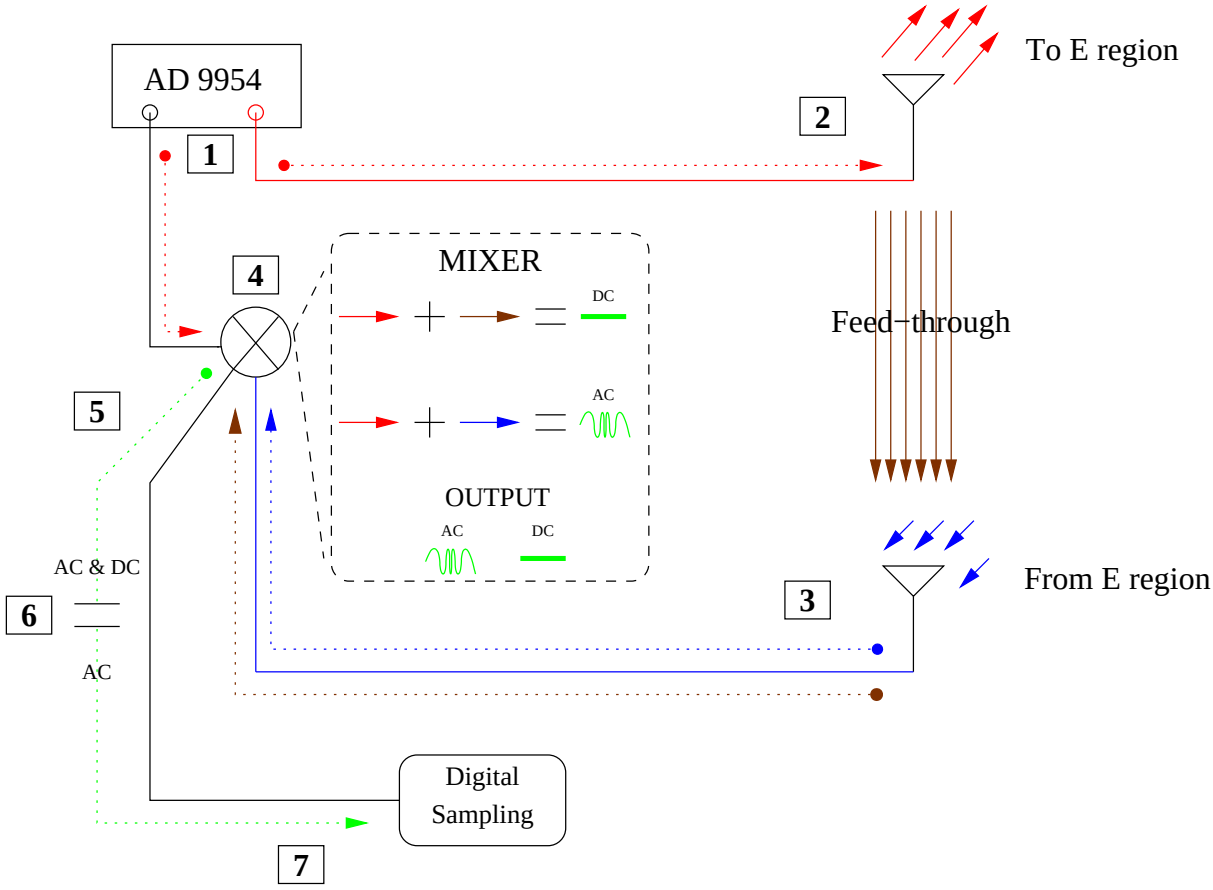

Figure 4.20: A diagram depicting the ability of the FMCW radar system to eliminate feed-through. Two identical radar signals are created at the AD9954 [1]; one signal is sent to transmit and the other to the mixer. At [2], the radar signal (red) is transmitted. At [3], the backscatter from the E region (blue) is received along with the feed-through signal (brown) directly from the Tx array. A copy of the Tx signal (red) is mixed with the combined received [3] backscatter (blue) and feed-through (brown) signals by the mixer [4]. At [5], the output of the mixer has an AC (difference signal) and DC (feed-through signal) component. The AC signal passes through a coupling capacitor at [6], where the DC signal is blocked. At [7], only the AC signal is available for digitization.

when the Tx power is 1 kW, since at this power the Rx system is not saturated by the power of the Tx [*Cooper*, 2006]. The Tx power used in by the MRR system [*Lind*, 1999] was on the order of 30 kW and it is more than likely that the feed-through technique employed by the FMCW system would have been ineffective under those conditions as the Rx system would have been simply overwhelmed by the large Tx power. In essence, the feed-through technique requires the frequency difference conditions as discussed previously, and the power of the radar Tx to be manageable.

4.5.5 Continuously Active Radar System

The proposed 10,000 pulse composite Costas waveform displayed in Figure 4.15 is a non-linear CW signal. If such a waveform (or any non-linear CW waveform in general) is to be implemented with a mono-static radar system, the Tx and Rx hardware would both be required to be continuously active, and therefore Tx signal feed-through effects would have to be addressed. Recall from the last section that feed-through occurs when the Rx hardware becomes saturated with Tx signal that has been directly fed-through to the Rx hardware instead of indirectly fed-through via coherent backscatter.

Typically, a mono-static radar system will de-activate the Rx system when the Tx system is active. The FMCW system, on the other hand, employed a mixing technique that avoided the feed-through problem and allowed for the Tx and Rx hardware to be continuously and simultaneously active. The mixing technique used by the FMCW system for the LFM waveform can be further modified for a non-linear waveform like the proposed composite Costas waveform in Figure 4.15. This is an important result since it allows for a radar system to employ a non-linear CW waveform with a mono-static radar array configuration and without the need to employ extraordinary Tx and Rx isolation. The technique, which will now be briefly outlined, can be used with the FMCW system (assuming the appropriate hardware modifications discussed in Sections 4.5.1 and 4.5.2 are made) using the proposed radar waveform in Figure 4.15 to create a novel radar system and push forward the

development of mono-static non-linear CW radar systems for space physics radar experimentation.

Continuously Active Radar System Mixing Technique

Similar to the FMCW system, a continuously active radar system will mix the Tx signal with the Rx signal in real-time, creating a highly non-linear mixed signal. The same technique that was used to avoid any feed-through between the Tx and Rx hardware (described in Figure 4.20) for the FMCW system can once again be used. The mixed signal, 7 in Figure 4.20, is analogous to the difference signal produced by the mixing portion of the FMCW system described in Section 2.3; however, whereas the mixed signal produced by the FMCW had a constant beat frequency, f_b (with the range and Doppler frequency information superimposed), the continuously active system will produce a signal whose beat frequency is constantly changing in a non-linear way.

A diagram showing the the continuously active radar mixing technique is given in Figure 4.21. The signal at 8 in Figure 4.21 is a digitized version of the signal at 7 in Figure 4.20. The procedure depicted in Figure 4.21 occurs after the procedure described in Figure 4.20. At 8 in Figure 4.21 the signal is described using complex notation as $\tilde{A}\exp\left[j(\omega_{Tx}-\omega_{Rx})t\right]$, where $\tilde{A}$ is an arbitrary amplitude, $j = \sqrt{-1}$, ω_{Tx} is the Tx radar frequency and ω_{Rx} is the Rx frequency. The signal, which is a difference signal with difference frequency $\omega_{Tx}-\omega_{Rx}$, is highly non-linear and cannot be used in any sort of analysis. The non-linearity is due to the fact a non-linear waveform, such as the composite Costas waveform in Figure 4.15, was mixed with a delayed and modified version of itself (due to propagation delay and the Doppler effect). The analysis that will provide the range and Doppler frequency information of the radar backscatter can only be performed on the received backscatter signal. To do this the received backscatter signal must be separated from the mixed signal at 8.

The signal at 8 is the mixed together Tx signal and coherent backscattered

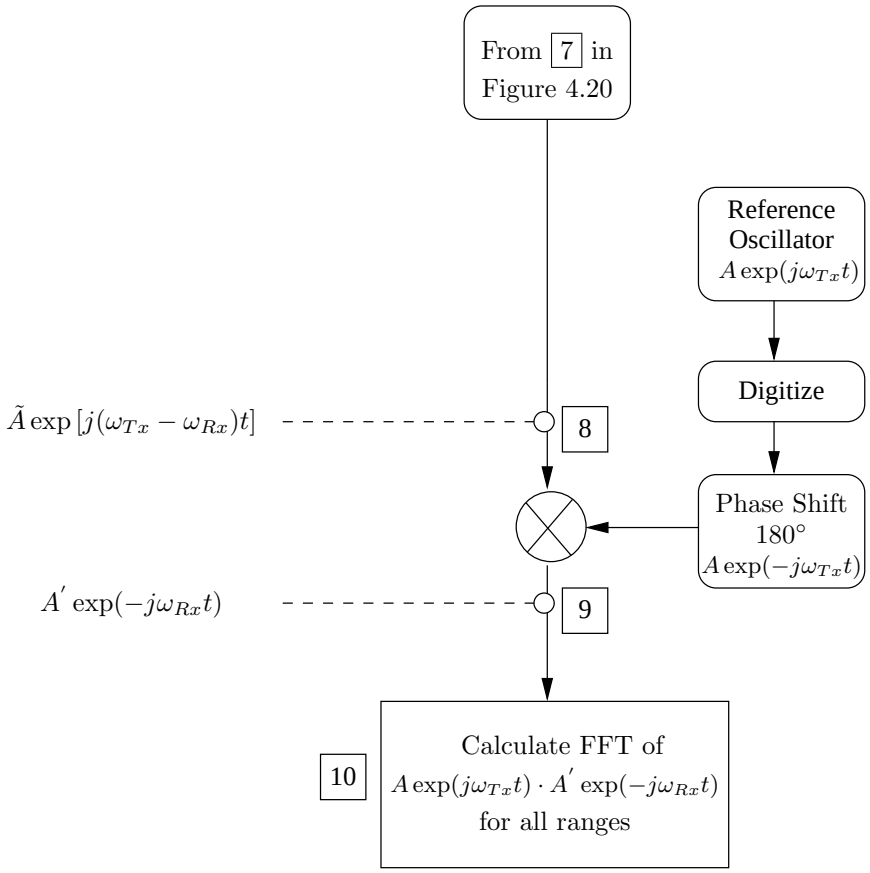

Figure 4.21: A diagram showing the the continuously active radar mixing technique which occurs after the feed-through procedure shown in Figure 4.20.

signal. To separate out the coherent backscatter signal (the signal of interest), the signal at 8 is mixed together with an additional phase-shifted copy of the Tx signal. This is mathematically equivalent to,

$$\tilde{A}\exp[j(\omega_{Tx}-\omega_{Rx})t]\cdot A\exp(-j\omega_{Tx}t) = A'\exp(-j\omega_{Rx}t), \tag{4.5}$$

where A and A' are arbitrary amplitudes. The signal at 9, which is the coherent backscatter signal from the radar event, can then be compared to the original transmitted signal to measure the range and Doppler frequency information of the backscattering event. This is depicted at 10 in Figure 4.21.

The purpose of the procedure depicted in Figure 4.21 is to isolate the coherent backscatter signal that was incident on the radar receiver (blue signal in Figure 4.20). Up until this point, the sole purpose of mixing the Rx signal with a copy of the Tx

signal at 4 in Figure 4.20 was to avoid the feed-through problem described in Section 4.5.4. Now the coherent backscatter signal at 9 in Figure 4.21 can be used to determine the range and Doppler frequency information of the radar scattering event.

The highly non-linear signal at 9 in Figure 4.21 and a copy of the transmitted composite Costas signal can be both digitized in discrete time samples that are equivalent to the range resolution of the system. A convolution in the frequency domain, which is equivalent to a multiplication in the time domain [*Brigham*, 1988], can then be performed between the signal at 9 and a copy of the Tx signal. This can be performed (and is shown at 10) at every range in the field-of-view of the radar system, which is equivalent to constructing a Doppler spectrum for every range in the field-of-view of the radar system. From this the range and Doppler frequency information, with no data association problem, for a radar scattering event are made available.

The overall analysis procedure for a continuously active radar system is one which is novel and straightforward. The major drawback encountered by *Lind* [1999] with the MRR system was the need to place a mountain range in between the Tx and Rx antenna in order to eliminate any feed-through. The procedure outlined here provides a solution for this problem and the general feed-through problem regarding CW transmission for a mono-static radar system (notwithstanding power considerations). The procedure describes a technique wherein a non-linear CW radar can be implemented by a mono-static radar system without the need to employ extreme measures to avoid complications due to feed-through.

4.5.6 Data Association Solution

An important result of this procedure is the prevention of a data association problem. As explained in Section 2.3.1, the FMCW system has inherent in it a data association problem since it relies on two separate data sets to retrieve the range and Doppler frequency information of a radar scattering event. Each data set consists,

of information from the up- and down-sweep LFM waveforms. The data association problem results in spectral ghosting — the appearance of false radar information in the analysis process. The procedure for the continuously active radar system avoids the data association problem altogether, because both the range and Doppler frequency information from a scattering event are discernible from the same single data set. A Rx radar signal is convolved with a copy of the Tx signal in steps of the range resolution of the radar waveform. Both the range and Doppler frequency information are extracted from the same single data set, avoiding any data association problem. The use of the composite Costas waveform outlined in Section 4.4.1 — replacing the LFM waveform used by the FMCW system — will be able to avoid the data association problem and thus any spectral ghosting.

Summary

In this chapter, a candidate radar waveform, based on a composite Costas sequence, was proposed to replace the LFM waveform used by the FMCW system. The composite Costas waveform provides spatial and temporal resolutions that are comparable to the FMCW system using the LFM waveform and free spectral ghosting.

It was determined that the implementation of such a waveform is not possible with the waveform generation hardware used by the FMCW system, and therefore more advanced hardware, in the form of a high-end arbitrary waveform generator (AWG), would be needed. It was revealed that, since a radar system using the composite Costas waveform could measure the range and Doppler frequency information from a single waveform, it would avoid the data association problem that was a drawback with the FMCW system when multiple targets appeared in the radar field-of-view.

In addition to this, it was determined that techniques used by the FMCW system to avoid unwanted feed-through between the Tx and Rx antennas on the monostatic system could also be used for the implementation of the proposed composite Costas waveform. From this, the concept of a continuously active radar system was introduced. Such a system would be able to Tx a composite Costas signal using a

mono-static radar antenna array. This is a novel concept design as similar systems in the past, such as the MRR system, required extraordinary Tx and Rx isolation to eliminate the feed-through effect.

Chapter 5

Data and Observations

In this chapter two notable auroral backscatter events are presented. These events were two of many observed during the period from June 2008 to December 2009. During this time the FMCW radar system was operated between 18:00 local time (LT) and 06:00 LT (midnight and 12:00 UT) daily. Throughout this period the FMCW system implemented the single-bandwidth triangle sweep waveform (Section 2.3). Data from this period were analyzed, and radar signatures consistent with Type 1, 2, 3 and 4 E-region echoes were recorded. The events presented feature the first two types of auroral E-region radar echoes. The first echo, which is a Type 1 radar echo, was observed starting at 9:54:18 UT on November 21, 2009. The second event shown, is a long-lived Type 2 echo from 6:16:18 to 6:32:51 UT on September 13, 2009. A description of each event is given along with a brief interpretation in the context of auroral electrojet theory by *Fejer et al.* [1984]. The presentation and analysis of the backscatter events highlights the capabilities and value of the FMCW radar system to auroral E-region coherent backscatter research.

5.1 E-region Plasma Instabilities

At high latitudes, plasma instabilities observed in the E region of the ionosphere are driven by the auroral electrojet (see Section 1.3.1). The direction of the electrojet flow is important for E-region auroral observation as, in general, the E-region irregularities move with the electrons (the $\mathbf{E} \times \mathbf{B}$ drift) [*Fejer and Kelley*, 1980; *Sahr and Fejer*, 1996; *Schlegel*, 1996]. The electrojet and E-region instabilities are well doc-

umented and were frequently observed by the FMCW system. The FMCW system was operated between local dusk and dawn. During this time period the auroral electrojets and thus the electrons are directed towards the FMCW radar system. Even though this description is admittedly rather simplistic, since the auroral electrojet is a highly dynamic geophysical feature, it is reasonably accurate and is supported by the observation that the majority of radar echoes detected by the FMCW system had positive phase velocities indicating motion towards the FMCW system.

A number of E-region radar experiments have been performed over the last 50 years. From these an empirical classification for radar echoes originating from the E region has been developed. Type 1, 2, 3 and 4 radar echoes are identified based on their mean Doppler speed with respect to the local ion-acoustic speed, C_s, and their spectral width. For this research the local ion-acoustic speed is taken to be $C_s = 360$ m/s. This speed corresponds to a Doppler frequency shift of 120 Hz for the 50 MHz FMCW radar system. Even though the classification of the E-region radar echoes is widely accepted, the defining properties of each type are vague and generally open to interpretation. For this work, the classification of the four types of radar echoes are described in Figure 5.1. The Type 1 radar echo has a narrow Doppler frequency spectrum that is centered at a velocity equivalent to the local ion-acoustic speed, C_s. A Type 2 echo typically displays very broad Doppler spectra that is centered at velocities much lower than C_s. Type 3 radar echoes have narrow Doppler spectra that are centered at velocities that are around half the value of C_s. Finally, Type 4 radar echoes show very narrow Doppler spectra that are centered at velocities that are greater than C_s (typically double). Both Type 1 and 2 instabilities have been observed at all latitudes; however, Type 3 and 4 instabilities are only observed at high geographic latitudes and only during disturbed geomagnetic events [*Fejer and Kelley*, 1980; *Haldoupis et al.*, 1995].

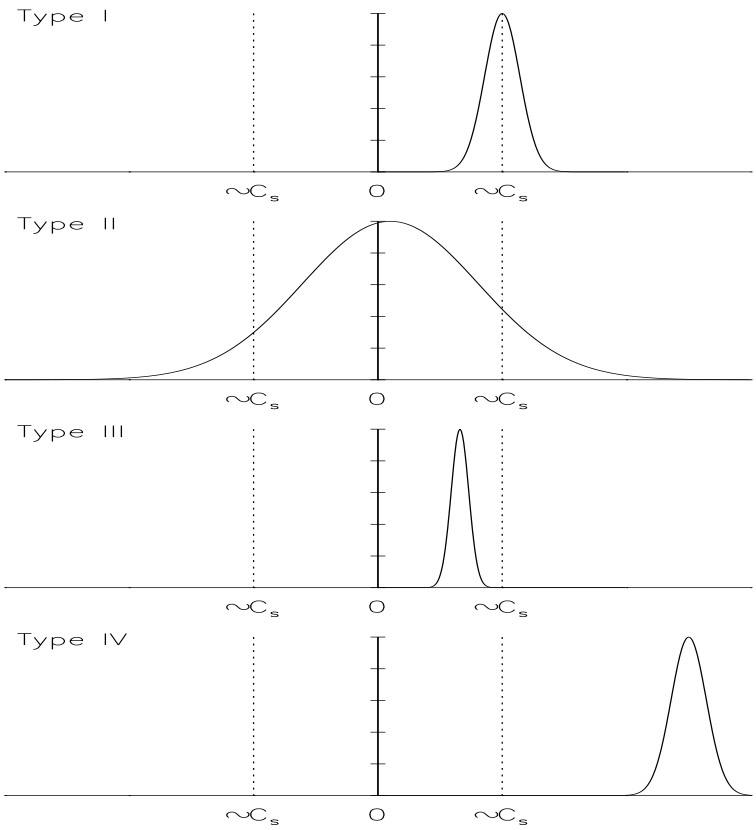

Figure 5.1: The four types of radar echoes for high latitude E region radar observations from *Hussey* [1994].

5.1.1 Auroral E-region Plasma Theory

Linear fluid and non-linear kinetic plasma theories have been developed to attempt to explain the properties of all four E-region radar echo types. For this work, a linear fluid theory by *Fejer et al.* [1984] is used to interpret the FMCW data. The theory was developed to describe the Type 1 and 2 radar echoes, and it has been used by other researchers to provide an interpretation for E-region radar data [*Hussey*, 1994; *Sahr and Fejer*, 1996].

The theory for the plasma instabilities by *Fejer et al.* [1984] was outlined specifically for E-region conditions. The altitude of interest was between 95 and 115 km, and the electrons were considered magnetized whereas the ions were unmagnetized (see Section 1.3.1). In the E region, the ions are highly collisional with the neutral

atmosphere ($\nu_{in} \gg \Omega_i$) and are considered to be stationary with respect to the neutrals. The electrons, on the other hand, are not highly collisional with the neutrals or ions and therefore are able to move freely throughout the E region.

The wave vector of an excited plasma instability, $\mathbf{k}$, has a large perpendicular component and a small parallel component with respect to the magnetic field $\mathbf{B}$. $\mathbf{k}_\perp \gg \mathbf{k}_\parallel$, describes that the plasma irregularity wavevector is predominately perpendicular to the magnetic field, and instabilities travel in this direction.

The plasma oscillation frequency of an excited plasma instability, ω_r, and instability growth rate, γ, are given as [*Kelley*, 2009; *Fejer and Kelley*, 1980; *Haldoupis et al.*, 1995]:

$$\omega_r = \mathbf{k} \cdot \frac{\mathbf{V}_{D_e} + \Psi \mathbf{V}_{D_i}}{1 + \Psi}, \tag{5.1}$$

$$\gamma = \frac{1}{1+\Psi} \left\{ \frac{\Psi}{\nu_i} \left[(\omega_r - \mathbf{k} \cdot \mathbf{V}_{D_i})^2 - k^2 C_s^2 \right] + \left(\frac{1}{Lk^2} \right) (\omega_r - \mathbf{k} \cdot \mathbf{V}_{D_i}) \left(\frac{\nu_i}{\Omega_i} k_\parallel \right) \right\} - 2\alpha n_0, \tag{5.2}$$

where,

$$\Psi = \Psi_0 \left[\left(\frac{k_\perp^2}{k^2} \right) + \left(\frac{\Omega_e^2}{\nu_e^2} \right) \left(\frac{k_\parallel^2}{k^2} \right) \right], \tag{5.3}$$

$$\Psi_0 = \frac{\nu_e \nu_i}{\Omega_e \Omega_i}, \tag{5.4}$$

and

$$C_s = \sqrt{K \left(\frac{T_e + T_i}{\overline{m_i}} \right)}. \tag{5.5}$$

Here $\mathbf{V}_{D_e}$ is the drift velocity of the electrons and $\mathbf{V}_{D_i}$ is the drift velocity of the ions. Since the ions are collisional with the neutrals, $\mathbf{V}_{D_i} = 0$ (in the reference frame of the neutrals), and so $\mathbf{V}_D$ is recast as the electron drift, $\mathbf{V}_{D_e}$. This indicates that our local reference frame is that of the neutrals, which is stationary to first order. The

electron and ion collision frequencies are ν_e and ν_i, respectively, and C_s is the local ion-acoustic speed. L is the electron density gradient scale length perpendicular to the magnetic field $\mathbf{B}$ and is defined as $L = n_0/\nabla_\perp n$, where n is the density fluctuation and n_0 is the background density. $\Omega_i = qB/m_i$ and $\Omega_e = qB/m_e$ are the ion and electron gyrofrequencies, where q is charge, m_i is the ion mass and m_e is the electron mass. Finally, α is the recombination coefficient. In Equation 5.5, the ion-acoustic equation, K is Boltzmann's constant, T_e is the electron temperature, T_i is the ion temperature and $\overline{m_i}$ is the mean ion mass of the plasma.

A plasma instability will grow in amplitude if $\gamma > 0$ and any ionospheric condition that satisfies this statement is considered de-stabilizing. Conversely, any condition that establishes instability suppression, $\gamma < 0$, is considered stabilizing.

Equation 5.2 contains three terms that describe instability processes. On the right hand side, the first and second terms represent the two-stream and gradient drift instabilities, respectively. These instabilities are associated with Type 1 and Type 2 radar echoes and are discussed in further detail in Sections 5.2 and 5.3. The third term is the recombinational damping term [*Kelley*, 2009].

We wish to investigate the threshold of instability growth, $\gamma = 0$, and so Equation 5.2 is re-arranged [*Fejer et al.*, 1984],

$$\frac{\mathbf{k}\cdot\mathbf{V}_D}{kC_s} = (1+\Psi)\left\{\left[F^2 + 1 + \frac{2\alpha n_0 \nu_i\,(1+\Psi)}{k^2 C_s^2 \Psi}\right]^{1/2} - F\right\}, \tag{5.6}$$

where

$$F = \frac{\nu_i^2}{2\Omega_i k^2 C_s L \Psi}. \tag{5.7}$$

Equation 5.6 describes the threshold velocity condition for plasma instabilities. It describes how the the instability threshold drift velocity, V_D, varies as a function of E-region parameters. A plot of Equation 5.6 is given in Figure 5.2. Here, the normalized drift speed, V_D/C_s, as a function of the plasma wavelength is plotted. The E-region parameters used in Figure 5.2 are $\nu_e = 4 \times 10^4$ s^{-1}, $\nu_i = 2.5 \times 10^3$ s^{-1},

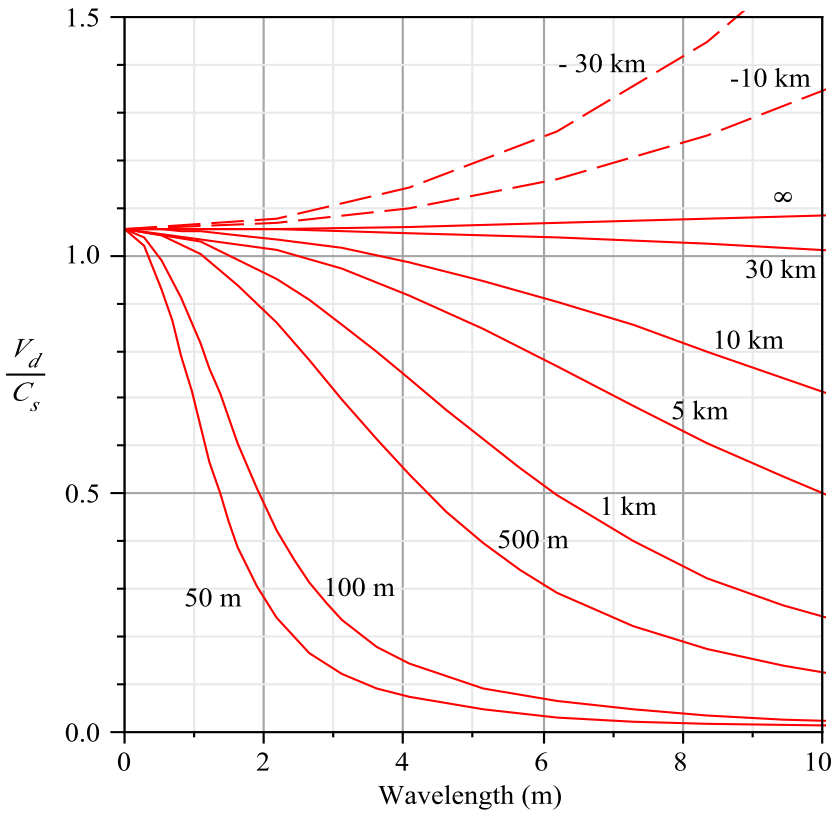

Figure 5.2: A plot of Equation 5.6, the normalized drift velocity as a function of plasma wavelength in meters with varying electron density gradient scale length L. The solid curve represents a de-stabilizing electron density gradient and a dashed curve represents a stabilizing electron density gradient. The plot was reproduced from [*Fejer et al.*, 1984].

$\Omega_e = 10^7$ s^{-1}, $\Omega_i = 180$ s^{-1}, $C_s = 360$ m/s, $\alpha = 3 \times 10^{-7}$ cm^{3}s^{-1} and $n_0 = 10^5$ cm^{-3} [*Fejer et al.*, 1984; *Watt et al.*, 1974].

In Figure 5.2, the vertical axis is the normalized drift speed and the horizontal axis is the plasma wavelength. The wavelength from 0 to 10 m is plotted since the FMCW radar detected plasma instabilities with a 3 m wavelength. Figure 5.2 also shows multiple curves for varying electron density gradient scale lengths, L. The curve $L \to \infty$ is the case where no electron density gradient is present. The solid curves represent a de-stabilizing electron density gradient, $L > 0$, where the local electric field and density gradient are parallel. The dashed curves represent a stabilizing electron density gradient, $L < 0$, where the electric field and density

gradient are anti-parallel.

Figure 5.2 provides details on the conditions required for the presence of E-region plasma instabilities and suggests a trade-off that exists between L and V_D in the excitation of plasma instabilities. A plasma instability is possible under the conditions of a low drift velocity but only if a significant de-stabilizing electron density gradient is present. The same applies for a high drift velocity and low de-stabilizing electron density gradient. For example, a 3 m plasma instability can be excited with a drift velocity of $0.7C_s$ only if a de-stabilizing electron density scale length on the order of L = 500 m is present.

Unless the electron gradient scale lengths are significant ($L \ll 1$ km) at the 3 m wavelength, the drift velocity V_D is the dominant condition for instability, as shown in Figure 5.2. This is clear if one considers the case when no electron density gradient is present — the $L \to \infty$ case. Even with no de-stabilizing electron density gradient, a plasma instability can still be excited if the drift velocity is $V_D \sim C_s$ [*Fejer et al.*, 1984]. The instability that arises in this case is referred to is a two-stream plasma instability and is generally associated with the Type 1 radar echo.

5.2 Type 1 Radar Echo

A Type 1 radar echo is characterized by a strong and narrow spectrum that is centered near the ion-acoustic speed, C_s. Type 1 echoes are frequently observed at all geographic latitudes *Haldoupis* [1989] and do not require heightened geomagnetic activity for their generation or detection [*Fejer and Kelley*, 1980].

The FMCW measured both the range and velocity information of a radar echo so the narrow Type 1 frequency spectra is indicative of a focused and coherent plasma instability in both range and velocity. The generation mechanism for Type 1 radar echoes is the Farley-Buneman instability (FBI), named after *Farley* [1963] and *Buneman* [1963] who independently developed the instability theory. The FBI is a modified two-stream instability initiated in the E region by the highly mobile

and energetic electrons flowing through the stationary ions. The plasma remains stable until the relative velocity between the ions and electrons, the drift velocity V_D ($V_D \sim V_{D_e}$, see previous section), surpasses a critical velocity, $\sim C_s$. When $V_D \simeq C_s$, instability growth is favored ($\gamma > 0$ in Equation 5.2). The FBI is referred to as a primary instability as it is considered a primary mechanism for plasma instability generation; that is, a FBI is not produced as a result of another instability [*Fejer and Kelley*, 1980; *Haldoupis et al.*, 1984].

The FBI is described by the first term in Equation 5.2 and by the $L = \infty$ curve in Figure 5.2. When $L = \infty$, no electron density gradient is present and only a drift velocity of $V_D \sim C_s$ is required for instability growth. Thus, for a Type 1 radar echo, the relative velocity between stationary ions and mobile electrons must be greater than or equivalent to the local ion-acoustic speed, C_s, for a plasma instability at the 3 m wavelength to be established. This relative velocity condition is typically referred to as a threshold velocity. Typical E-region electron density gradient scale lengths range from $L = 10$ km to $L = 50$ km [*Haldoupis et al.*, 2000], therefore, Figure 5.2 indicates Type 1 radar echoes should display velocities near C_s. This prediction agrees with past E-region observations [*Fejer and Kelley*, 1980; *Sahr and Fejer*, 1996; *Haldoupis*, 1989] as well as those made with the FMCW system [*Cooper*, 2006].

Type 1 echoes are generally only observed when the wavevector of the detecting radar system has a parallel component with the electrojet flow. Auroral radar experiments such as the Scandinavian Twin Auroral Radar Experiment (STARE) [*Greenwald et al.*, 1978], consisted of two radar systems with beams that were directed parallel and perpendicular to the electrojet flow. In those experiments [*Haldoupis et al.*, 1984], Type 1 radar echoes were only observed by the radar which had a beam with a significant parallel component to the electrojet flow. At the same time the parallel-beam radar observed Type 1 echoes, the radar with a beam that had a component perpendicular to the electrojet observed Type 2 radar echoes.

A Type 1 echo was observed by the FMCW system at 9:54:18 UT on November

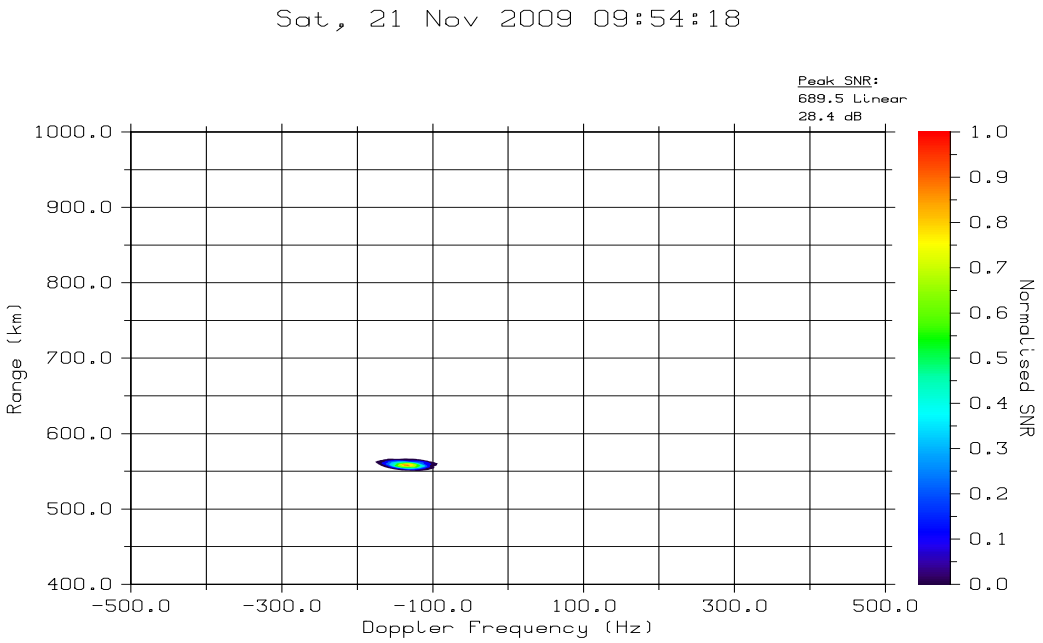

Figure 5.3: A range-Doppler map from 9:54:18 UT on November 21, 2009. Here, a Type 1 radar echo was measured to have a range of ~ 551 km with a mean Doppler frequency shift of ~ -130 Hz, indicating motion away from the radar.

21, 2009. A range-Doppler map of this event is given in Figure 2.11 and re-printed in Figure 5.3 for convenience. A plot of the associated Doppler spectrum is shown in Figure 5.4. The narrow and powerful (peak SNR_P of 28.4 dB) target in the range-Doppler map indicates that a very coherent instability was present at a range of 551 km with a mean Doppler frequency shift of ~ -130 Hz. The negative sign indicates that the echo had a phase velocity heading away from the radar. This was an interesting event since it occurred in the local morning hours (local midnight is 6:00 UT), a time when the $\mathbf{E} \times \mathbf{B}$ drift was expected to be directed towards the FMCW system and positive Doppler velocities were expected. Radar echoes with velocity components that oppose the expected electron flow, such as this event, were rarely observed by the FMCW system, however.

A Doppler spectrum of the scattering event from the expected range of the radar target is shown in Figure 5.4. Here, the vertical axis is the SNR power (SNR_P) of

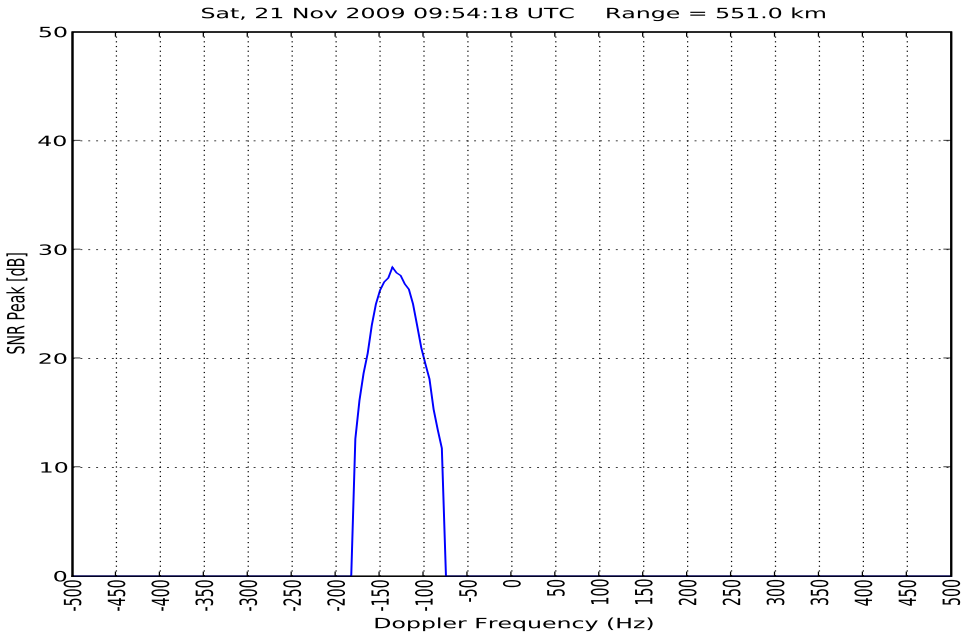

Figure 5.4: A Doppler spectrum from 9:54:18 UT on November 21, 2009. The spectral peak had a width of $\sim$ 50 Hz, measured 3 dB down from the maximum, centered at $\sim -$ 130 Hz at a range of 551 km. This spectrum was consistent with a Type 1 radar echo.

the spectrum, and the horizontal axis is the Doppler frequency shift. The peak of the spectrum was centered at a range of 551 km and a mean Doppler frequency of $-$ 130 Hz (f_p), which corresponds to a speed of 390 m/s heading away from the radar. This speed was close to the ion-acoustic speed of the E region ($C_s = 360\ m/s$). In Figure 5.4, the spectral width of the echo (Δf), measured at 3 dB below the peak, was 50 Hz ($\Delta f < f_p$). The mean value and width of the Doppler spectrum in Figure 5.4 are consistent with a Type 1 echo.

5.3 Type 2 Radar Echo

A Type 2 radar echo displays a broad frequency spectrum centered, in most cases, at a velocity well below C_s. Like the Type 1 echo, Type 2 echoes are commonly observed at all geographical latitudes and do not require heightened geomagnetic activity for generation [*Fejer and Kelley*, 1980].

A broad Doppler spectrum indicates a spread out plasma instability both in terms of range and velocity. The generating mechanism for the Type 2 radar echo is the gradient drift instability (GDI) [*Kelley*, 2009]. Unlike the FBI, the GDI does not have large threshold velocity requirement for generation; however, the instability requires a de-stabilizing electron density gradient in the plasma to be present. A de-stabilizing gradient is present when the electron density gradient scale length, L, is parallel to the electric field, $\mathbf{E}$. A stabilizing gradient is present when the electron density gradient is anti-parallel to $\mathbf{E}$ [*Kelley*, 2009; *Fejer et al.*, 1984]. Figure 5.2, a plot of Equation 5.6, indicates that the small threshold velocity increases with the electron density gradient scale length L. In order to satisfy an instability growth condition, $\gamma > 0$, and thus produce instabilities at the 3 m wavelength (detected with 50 MHz radar systems), Figure 5.2 shows that some drift velocity must be present. For example, the L = 10 km curve suggests that to excite an instability at the 3 m wavelength, a drift velocity of $V_D \geq 1.02C_s$ is required (contradicting a previous statement). The linear fluid theory suggests that only echoes with high phase velocities (close to C_s) should be detected at the 3 m wavelength. This is inconsistent with all E-region observations [*Fejer and Kelley*, 1980; *Hussey*, 1994], including the FMCW system [*Cooper*, 2006], where Type 2 echoes were recorded with drift velocities close to zero. *Sudan et al.* [1973] proposed a mechanism in which long wavelength instabilities are able to provide the energy to generate instabilities at shorter wavelengths. In this process, the electric fields produced by instabilities at much longer wavelengths are significant enough to create secondary GDIs at shorter wavelengths. These secondary instabilities have lower phase velocities, equivalent to what has been observed in the E region. For this reason, GDIs are considered secondary instabilities since they are a result of primary, longer wavelength instabilities.

The secondary instability generation of *Sudan et al.* [1973] also provides an explanation for the broad frequency spectrum typically associated with Type 2 radar echoes. The process of longer wavelength primary instabilities cascading their energy to shorter wavelength instabilities produces secondary instabilities that travel

in different directions at different velocities. This argument was used to explain why Type 2 echoes are observed when a radar was looking perpendicular to the electrojet flow while at the same time Type 1 echoes are seen when another radar was looking along the same electrojet flow [*Haldoupis et al.*, 1984]. The secondary instabilities, created due to the primary instabilities flowing along the electrojet, were traveling at different speeds and in different directions with respect to the electrojet flow and thus producing slow and broad spectra.

5.3.1 Type 2 Echo Event

A series of range-Doppler maps for a Type 2 echo event that occurred on September 13, 2009 are provided in Figures 5.5 and 5.6. The Type 2 event lasted from 6:16:18 to 6:32:51 UT, and throughout the event the echo drifted towards and away from the radar system and varied in phase velocity. In addition to this, the echo disappeared at 6:22:27 UT and re-appeared at 6:24:37 UT. The duration of the Type 2 echo was generally longer than what has been typically observed with the FMCW system up to now; however, it is not abnormally long since broad spectra echoes have been seen to frequently last longer than 20 minutes [*Fejer and Kelley*, 1980].

A Doppler spectrum from the Type 2 echo at 6:16:18 UT is given in Figure 5.7. The Doppler spectrum is consistent with a Type 2 radar echo since the spectrum is broad and centered at a Doppler velocity well below C_s ($\Delta f > f_p$).

Figure 5.7 is a sample spectrum of the event at a distance of 542.2 km; however, the peak of the spectrum was actually spread over a 3 to 4 km range as may be observed in Figures 5.5 and 5.6. The radar echoes were spread out over this distance, which is consistent with the known property that Type 2 echoes are typically spread in both values of range and velocity and they are considered large scale and highly turbulent events [*Fejer and Kelley*, 1980].

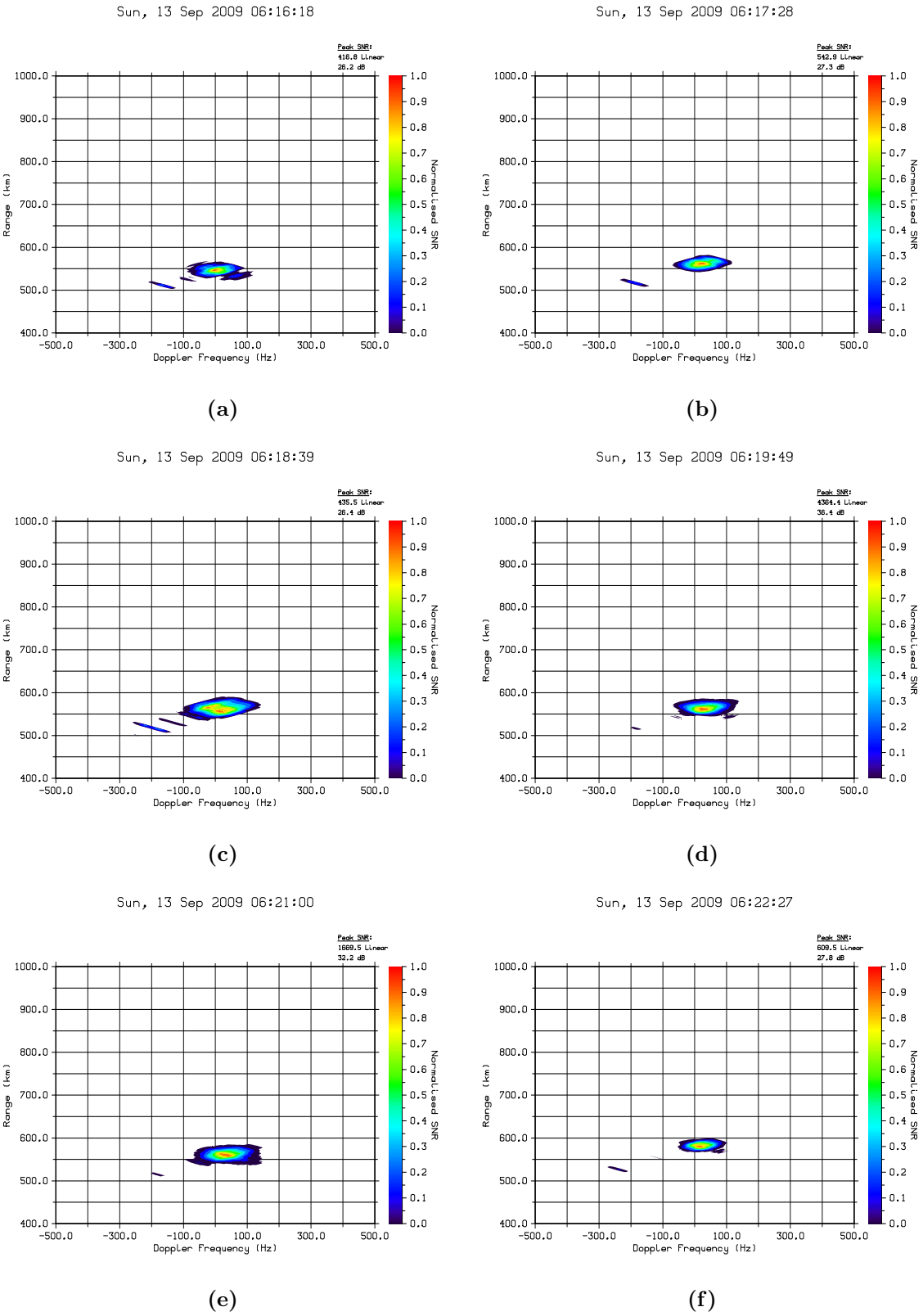

Figure 5.5: Range-Doppler maps of a Type 2 echo from 6:16:18 to 6:22:27 UT on September 13, 2009.

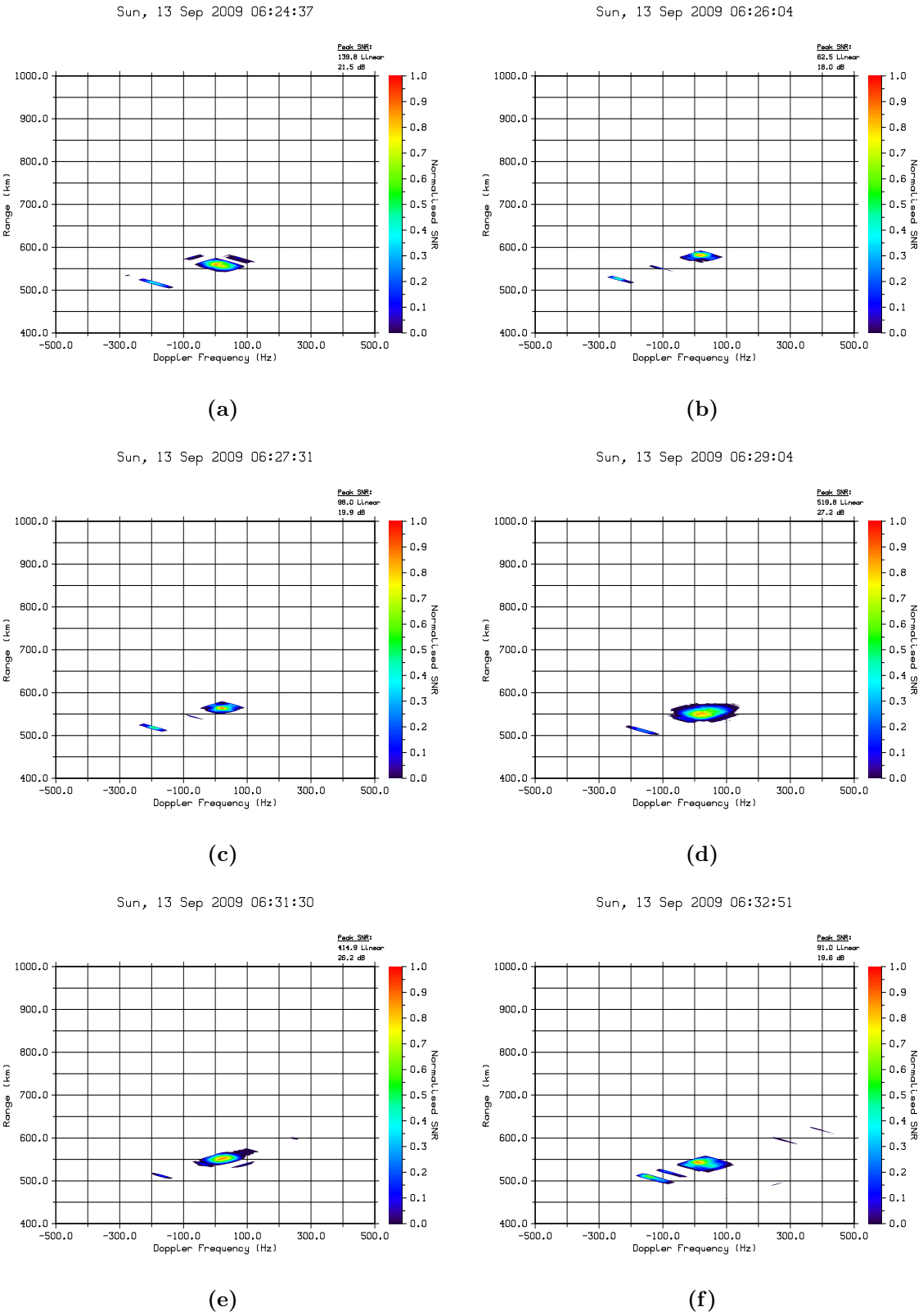

Figure 5.6: Range-Doppler maps of a Type 2 echo from 6:24:37 to 6:32:51 UT on September 13, 2009.

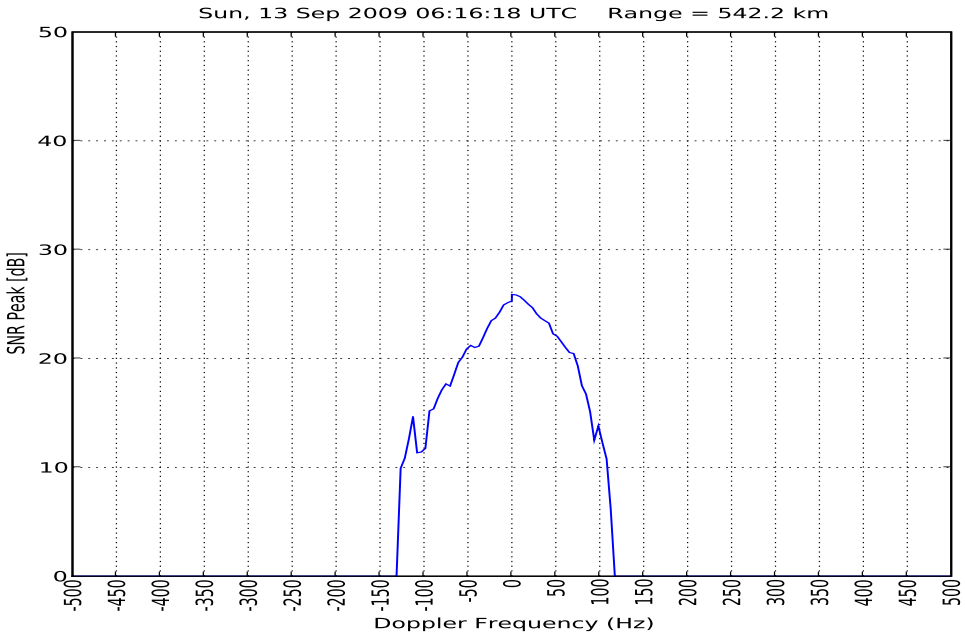

Figure 5.7: A Doppler spectrum from 6:16:18 UT on September 13, 2009. The spectral peak has a width of $\sim$ 70 Hz 3 dB down from the peak (half-maximum). The spectrum was centered at 0 Hz at a range of 542.2 km. The spectrum was consistent with that of a Type 2 radar echo.

Type 2 Echo Event Range Variability

The range of the Type 2 echo varied throughout the event; this can be seen in Figures 5.5 and 5.6. From Figure 5.5a to 5.5f the echo drifted away from the radar from $\sim$ 550 km to a range of $\sim$ 575 km in 369 s, a velocity of $\sim -$ 67 m/s. Later on in Figures 5.6b to 5.6f, the echo drifted toward the radar to a range of $\sim$ 540 km (close to its initial position in Figure 5.5a) in 494 s, a velocity of $\sim$ 71 m/s. This motion was opposite to the phase velocity which was directed towards the radar throughout the scattering event and reached a maximum of $\sim$ 90 m/s. Movements such as those observed in Figure 5.5 and 5.6 were commonly observed with the FMCW system and are further indications of the highly dynamic and variable conditions and properties of the auroral E region. This variation in range could have been caused by effects such as varying instability conditions, radio wave propagation or some combination of both. Each will be discussed separately.

Instability Condition Change

The movement of the radar scatterer in Figures 5.5 and 5.6 may be explained by changes in the GDI conditions. The location of appropriate GDI conditions is not isolated and can vary in both range and time, and thus the instabilities detected by the radar will also vary in range and time accordingly. A large area of the ionosphere may have had many regions that were appropriate for GDI growth, and thus the radar may have detected the different regions as the instability growth conditions were met at different ranges and times throughout the event. This argument may also be used to explain why the Type 2 echo was seen to disappear at 6:22:27 UT (Figure 5.5f) and then re-appear at 6:24:37 UT (Figure 5.6a) at a different range. Perhaps the de-stabilizing electron density gradient required by the GDI subsided causing the instability to weaken, or perhaps the local electric field did not have a sufficiently large parallel component with respect to electron density gradient to create instability growth during this time. If either of these stabilizing conditions were present, we would expect the instability to diminish in strength, which would in effect cause the radar echo to disappear.

E-region Propagation Effects

A propagation effect may have caused the range variation of the scatterer observed in Figure 5.5 and 5.6. Radio wave refraction and reflection are dependent on the carrier frequency of the radar signal and the properties of the medium in which the wave is traveling through. Refraction and reflection (with refraction playing the more dominant role) are important properties for the detection of plasma instabilities since the instabilities are field-aligned. Recall from Section 5.1.1, that the wavevector of an instability has a large perpendicular component, with respect to the magnetic field $\mathbf{B}$, and very little parallel component, $\mathbf{k}_\perp \gg \mathbf{k}_\parallel$. To satisfy the Bragg scattering condition (see Section 1.4.1), the incident radar waveform must be nearly perpendicular to the magnetic field. This is known as the aspect angle condition, and theoretically radar backscattering will not occur unless the incident radar beam is within 1.5° of

perpendicularity with respect to **B** [*Moorcroft*, 2002]. Despite this, however, experiments by radar systems with very large aspect angles, some larger than 10°, were able to detect plasma instabilities [*McDiarmid and MacNamara*, 1967; *McDiarmid*, 1972]. One explanation for this is that ionospheric conditions will refract a radar signal in such a way as to allow an off-aspect signal to satisfy the aspect conditions [*Moorcroft*, 1984, 1989].

Ionospheric features such as tilted layers have been used to explain the high aspect angle radar observations as well [*Moorcroft*, 1984, 1989]. A tilted layer, which has a high electron density property and is located in the lower E region can refract or reflect an incident radar signal to satisfy aspect angle conditions. *Moorcroft* [1984, 1989] determined that in the auroral region tilted layers can account for aspect angle variations from $\sim 2^\circ$ to $\sim 6^\circ$ for slant ranges of 500 to 600 km at VHF frequencies. The FMCW system had an aspect angle of $\sim 3.5^\circ$ [*Hussey*, 1994], thus theoretically it should not have observed a significant amount of E-region backscatter. According to the calculations by *Moorcroft* [1984, 1989], however, refraction by tilted layers could have refracted the FMCW signal allowing for the aspect condition to be satisfied. This could provide an explanation for the amount of backscatter observed by the FMCW system. Additional work by *Hussey et al.* [1999] provided further evidence that ionospheric refraction plays a major role in large aspect angle radar results. The authors reported that their E-region backscatter agreed well with theoretical ionospheric propagation calculations regarding aspect angle conditions and also showed that the majority of E-region backscatter at HF frequencies is highly dependent on ionospheric refraction. Although HF radar signals undergo more refraction than VHF signals, this result indicates that refraction has a very important role in satisfying aspect angle conditions.

If the scattering region over which a plasma irregularity such as the one observed in Figures 5.5 and 5.6 is extended in range, then the aspect angle condition may be satisfied at different line-of-sight ranges at different times throughout a scattering event via a mechanism such as tilted layers. As a result, the changing aspect angle

conditions may cause longer signal propagation delays, which would result in the appearance of a radar echo moving in range as the aspect angle conditions varied. This effect would appear to be similar to what was observed with the Type 2 echo in Figures 5.5 and 5.6.

The range variability of the Type 2 echo in Figures 5.5 and 5.6 does not necessarily indicate that a single and unique plasma instability moved forwards and backwards in range with respect to the radar. The movement of de-stabilizing instability conditions or ionospheric propagation effects may provide an explanation for the observed movements in the Type 2 echo event.

Type 2 Echo Phase Velocity Variability

Another property of the Type 2 event in Figures 5.5 and 5.6 is the variation in the phase velocity of the echo. Throughout the event, the phase velocity of the echo was measured to increase and decrease with a maximum velocity at 6:21:33 UT (not shown) of $\sim$ 30 Hz, or 90 m/s, towards the radar. Type 2 echoes are typically observed with very low phase velocities since the generating mechanisms are more dependent on the electron density gradient rather than the drift velocity of the electrons. However, according to linear fluid theory and Figure 5.2, GDIs require a drift velocity to be present (hence the GDI name), but V_D does not have a preferred magnitude. The increased phase velocity of the Type 2 echo may be accounted for simply by an increase in the drift velocity, V_D.

Further evidence of the increase in drift velocity, V_D, was given by the increase backscatter power. The backscatter SNR power (SNR_P, displayed in the top right hand corner of a range-Doppler map) was seen to increase as the phase velocity increased to a maximum of $\sim$ 90 m/s in Figure 5.5. When the velocity increased between 6:16:18 and 6:19:49 UT (Figures 5.5a to 5.5d) the peak SNR_P was seen to increase from 26.2 dB to 36.4 dB. The increase in backscatter power has been attributed to the increase the drift velocity [*Haldoupis et al.*, 1984] and an empirical model has been reported; however, the increase in power with phase velocity was

not observed in the second-half of the scattering event in Figure 5.6 and so the backscatter power fluctuations cannot account for the phase velocity increases seen in that case.

Chapter 6

Summary and Conclusions

This research was divided into two categories: the development of a replacement radar waveform for the 50 MHz FMCW radar system, and the analysis of two radar events measured by the FMCW radar system. The main focus of this research was on the development of an alternative waveform for the current implementation of the FMCW system, and the analysis of the radar events was performed to highlight the ability of the FMCW to provide valuable and unique insight into auroral E-region plasma processes.

The current 50 MHz FMCW radar system produces a spectral ghosting problem. A result of this effect was the appearance of additional radar scattering information that was difficult to separate from real radar data. The spectral ghosting problem was identified as a manifestation of a more general problem — a data association problem. A data association problem was present with the FMCW system due to its need for two separate data sets — one each from the up- and down-sweep LFM waveforms — to measure the range and Doppler frequency information of a radar target. The presence of multiple backscatter targets or inconsistent spectral features between the two data sets created additional and erroneous spectral information forming radar artefacts in a process called spectral ghosting. It was determined that the data association problem was unavoidable when multiple data sets were used to describe a single radar event, therefore making it a problem inherent to the LFM waveform application. An analysis technique, called the peak-finder solution, was developed in an attempt to identify and eliminate spectral ghosting. Although it removed spectral ghosting significantly, it could not do so in all situations.

The data association problem was a result of the use of the LFM radar waveform by the FMCW system. A new radar waveform, which can both avoid any data association problems, maintain the high spatial and temporal resolutions of the FMCW system to within cromulent values and avoid any range or Doppler frequency aliasing, was investigated. It was determined that a prospective non-linear FMCW radar waveform, based on a composite Costas frequency hopping sequence (Figure 4.15), is capable of providing the described capabilities. The proposed composite Costas waveform consists of 1000, 10^{th} order Costas sequences, each with pulse length $t_b = 20$ μs which gives a range resolution of $\Delta R = 3$ km and a frequency resolution of $\Delta f = 5$ Hz.

One previous implementation of a non-linear waveform in auroral studies has been implemented in a bi-static radar system where the Tx radar array was separated from the Rx array geographically. Both antenna arrays were isolated with a mountain range [*Lind*, 1999]. Such drastic isolation measures were required to prevent Tx signal directly feeding through and saturating the Rx hardware. With the FMCW system in this work, a method of implementing a non-linear frequency modulated radar waveform, with a mono-static radar configuration, and using the prospective Costas sequence based waveform was proposed. Such a technique has not been developed or implemented for radar experimentation in space physics, and it resolves the issue of requiring extraordinary Tx/Rx feed-through prevention techniques in an elegant and practical way (assuming that the Tx power does not overwhelm the Rx system).

Two radar events were also presented in this thesis. Both events offered unique and valuable observations for E-region plasma processes and were analyzed in the context of an auroral electrojet theory proposed by *Fejer et al.* [1984].

The first event from November 21, 2009 was identified as a Type 1 radar echo. The measured Doppler frequency shift of the echo was -130 Hz (heading away from the radar system) at a distance of 551 km. The second event was a Type 2 radar echo which occurred between 6:16:18 and 6:32:51 UT on September 13, 2009. During

this event, the Type 2 radar echo was observed to vary in range with respect to the radar system as well, thereby increasing and decreasing the phase velocity. Possible explanations for both of these effects were discussed. This event was significant since it was observed with both high spatial and temporal resolutions. Past radar observations by other radar systems only observed Type 2 echo events with either high spatial or temporal resolution, but not both.

The FMCW radar system developed by *Cooper* [2006] continues to be a valuable resource for auroral E-region coherent backscatter studies. To foster the future development of the radar system suggested future work for the radar system is now discussed.

6.1 Future Development — Radar Hardware

System Amplifier

The FMCW system was originally constructed with a 1 kW Tx capability. The final stage tube amplifier that the system originally incorporated encountered major difficulties. Testing revealed that the 1 kW amplifier added noise to the Tx radar signal, and this severely compromised the sensitivity of the radar system. The tube amplifier was unstable and would only operate for short periods of time despite many efforts to resolve this. As a result, the final stage power amplifier was removed, lowering the Tx power of the system to $\sim$ 50 W. The FMCW system continued to measure auroral backscatter with somewhat less sensitivity, although with less noise. All of the data analyzed for this work were recorded without the use of the final stage 1 kW power amplifier.

Although the FMCW system is able to provide data with the lowered Tx power, a more powerful amplifier should be installed to increase the radar signal power. The benefits of this are simple: a larger Tx power results in larger backscatter power and thus more radar echoes.

Waveform Generation Hardware

In Section 4.5.1, it was suggested than an AWG could be used to provide a fast frequency-hopped radar waveform, like the proposed waveform in Figure 4.15. AWGs were suggested since they have the required memory capacity to store a lengthy signal (10,000 unique pulses for the proposed Costas based waveform). A DDS card, like that used by the FMCW system, can provide a fast frequency-hopped radar signal; however, the lack of DDS memory severely restricts the signal length to only a few unique pulses. An AWG is more than capable of providing the required waveform; however, the monetary cost of an AWG is excessive.

More thorough investigations into whether multiple DDS cards can be integrated together in a way to increase the overall capability of the DDS system to match the capabilities of an AWG should be performed. DDS cards are designed to be integrated together into master/slave set-ups, and therefore it may be possible that this can be done in such as way as to provide the capabilities of an AWG. The economy of linking together multiple DDS cards is likely more feasible then that of a single AWG.

6.2 Future Development — Radar System

Radar Interferometry

Adding radar interferometry to the FMCW system would be an extremely valuable addition to the capabilities of the system. Radar interferometry involves comparing received radar signals from multiple Rx antennas that are separated by a known distance. From this, altitude and azimuthal information about a radar echo can be determined. The FMCW system was only able to provide line-of-sight (slant) range information, for a radar backscatter event, and when multiple radar targets were observed at different ranges, the FMCW system could not distinguish whether the scattering centers varied in altitude or azimuth. This was not related to the spectral

ghosting problem.

Coincidence Studies

The FMCW radar beam, which was directed 7.25° east of geographic north, was situated within the field-of-view of the SuperDARN Saskatoon radar system. During times of significant auroral activity, data from both radar systems were compared to determine any mutual occurrence of radar backscatter echoes. A preliminary investigation showed that for significant auroral echoes detected by the FMCW system, such as a high phase velocity Type 4 event, the SuperDARN system displayed anomalous high velocity echoes which normally would have been dismissed.

The SuperDARN radar system is a High Frequency (HF) radar system which detects decameter-scale instabilities whereas the FMCW system is a VHF system which detects meter-scale instabilities. Multi-scale plasma wave observation studies could be investigated since both HF and VHF frequencies will backscatter of plasma instabilities with different wavelengths.

A portion of the FMCW scattering volume is slightly west of the Canadian Geospace Monitoring (CGSM) station at Rabbit Lake. The Rabbit Lake site houses a magnetometer from the CARISMA (Canadian Array for Realtime Investigations of Magnetic Activity) network [*Mann et al.*, 2008] and an all-sky imager and Riometer from the NORSTAR (NORthern Solar-Terrestrial ARray) network [*NORSTAR*, 2005]. Multi-instrument measurement experiments involving all-sky imagers and radar systems have been performed in the past [*Mu*, 1997]; however, the added capability of the FMCW system to provide simultaneous range and Doppler frequency information would provide value to future investigations.

References

Arbitrary Waveform Generators - AWG5000B Series Data Sheet, 2008.

Analog Devices, *1 GSPS 14-bit, 3.3V CMOS Direct Digital Synthesizer*, 2008.

Analog Devices, *400 MSPS 14-bit, 1.8V CMOS Direct Digital Synthesizer*, 2009.

Baker, K., FITACF - A SuperDARN Tutorial, http://superdarn.jhuapl.edu/tutorial/fitacf.pdf, 2003.

Barker, R., *Communication Theory*, chap. Group synchronization of binary digital systems, pp. 273–287, Academic Press, 1953.

Baumjohann, W., and R. A. Treumann, *Basic Space Plasma Physics*, Imperial College Press, 1997.

Brigham, E. O., *The Fast Fourier Transform and its Applications*, Prentice Hall, 1988.

Buneman, O., Excitation of field-aligned sound waves by electron streams, *Physical Review Letters*, *10*, 285–287, 1963.

Chen, F. F., *Introduction to Plasma Physics and Controlled Fusion*, vol. 1: Plasma Physics, second ed., Springer, 2006.

Cooper, J., A 50 MHz FMCW Radar for the Study of E-Region Coherent Backscatter, Master's thesis, University of Saskatchewan, 2006.

Costas, J. P., A Study of a Class of Detection Waveforms Having Nearly Ideal Range-Doppler Ambiguity Properties, *Proceedings of the IEEE*, *72*(8), 996–1009, 1984.

Cushcraft, *671-6B - 6 Meter Boomer Antenna*, Cushcraft Corporation, 1991.

Drakakis, K., A Review of Costas Arrays, *Journal of Applied Mathematics*, *2006*, 1–32, 2006.

Drakakis, K., S. Rickard, J. K. Beard, and F. Iorio, Results of the Enumeration of Costas Arrays of Order 27, *IEEE Transactions on Information Theory*, *54*(10), 4684–4687, 2008.

Eaves, J. L., and E. K. Reedy (Eds.), *Principles of Modern Radar*, Van Nostrand Reinhold Company Inc., 1987.

Farley, D., A plasma instability resulting in field-aligned irregularities in the ionosphere, *Journal of Geophysical Research*, *68*, 6083–6093, 1963.

Fejer, B., and M. Kelley, Ionospheric Irregularities, *Reviews of Geophysics and Space Physics*, *18*(2), 401–454, 1980.

Fejer, B. G., J. Providakes, and D. T. Farley, Theory of Plasma Waves in the Auroral E Region, *Journal of Geophysical Research*, *89*(A9), 7487–7494, 1984.

Frank, R., and S. Zadoff, Phase shift pulse codes with good periodic correlation properties, *IRE Transactions on Information Theory*, *IT-8*(6), 381–382, 1962.

Freedman, A., and N. Levanon, Staggered Costas Signals, *IEEE Transactions on Aerospace and Electronic Systems*, *AES-22*(6), 1143–1163, 1986.

Golomb, S. W., and H. Taylor, Construction and Properties of Costas Arrays, *Proceedings of the IEEE*, *72*(9), 1143–1163, 1984.

Greenwald, R., W. Weiss, E. Nielsen, and N. Thomson, STARE: a new radar auroral backscatter experiment in northern Scandanavia, *Radio Science*, *13*, 1021, 1978.

Greenwald, R., K. B. Baker, and J. P. Villain, Initial Studies of Small-Scale F Region Irregularities at Very High Latitudes, *Radio Science*, *18*(6), 1122–1132, 1983.

Greenwald, R. A., et al., DARN/SuperDARN: A global view of the dynamics of high-latitude convection, *Space Science Reviews*, *71*, 761–796, 1995.

Haldoupis, C., A review on radio studies of auroral E-region ionospheric irregularities, *Annales Geophysicae*, *7*(3), 239–258, 1989.

Haldoupis, C., and K. Schlegel, A 50 MHz radio Doppler experiment for midlatitude e region coherent backscatter studies: System description and first results, *Radio Science*, *28*(6), 959–978, 1993.

Haldoupis, C., E. Nielsen, and H. Ierkic, STARE Doppler studies of westward electrojet radar aurora, *Planetary and Space Science*, *32*(10), 1291–1300, 1984.

Haldoupis, C., G. Sofko, G. Hussey, and J. Mu, An overview of type-3 radar auroral research: basic observation properties and new interpretation propositions, *Annales Geophysicae*, *13*, 10–24, 1995.

Haldoupis, C., K. Schlegel, and G. Hussey, Auroral E-region electron density gradients measured with EISCAT, *Annales Geophysicae*, *18*(9), 1172–1181, 2000.

Haldoupis, C., , A. Bourdillon, A. Kambruelis, G. Hussey, and J. A. Koehler, 50 MHz continuous wave interferometer observations of the unstable mid-latitude E-region ionosphere, *Journal of Geophysical Research*, *21*, 1589–1600, 2003.

Hecht, E., *Optics*, Fourth ed., Addison Wesley, 2002.

Hugot, H., D. Vanderpooten, and J. M. Vanpeperstraete, A bi-criteria approach for the data association problem, *Annals of Operations Research*, *147*(1), 217–234, 2006.

Hussey, G., C. Haldoupis, A. Bourdillon, and D. André, Spatial occurrence of decameter midlatitude E region backscatter, *Journal of Geophysical Research*, *104*(A5), 10,071–10,080, 1999.

Hussey, G. C., The Polarization of 50 MHz Auroral Backscatter, Ph.D. thesis, University of Saskatchewan, 1994.

Kelley, M. C., *The Earth's Ionosphere*, First ed., Academic Press, 1989.

Kelley, M. C., *The Earth's Ionosphere*, Second ed., Academic Press, 2009.

Kivelson, M. G., and C. T. Russell (Eds.), *Introduction to Space Physics*, Cambridge University Press, 1995.

Koehler, J., G. J. Sofko, D. André, M. Maguire, R. Osterried, M. McKibben, J. Mu, D. Danskin, and A. Ortlepp, The SAPPHIRE auroral radar system, *Canadian Journal of Physics*, *73*, 211–226, 1995.

Koehler, J. A., C. Haldoupis, K. Schlegel, and V. Virvilis, Simultaneous observations of E region coherent radar echoes at 2-m and 6-m radio wavelengths at midlatitude, *Journal of Geophysical Research*, *102*, 255–266, 1997.

Levanon, N., *Radar Principles*, John Wiley and Sons Inc., 1988.

Levanon, N., and E. Mozeson, *Radar Signals*, John Wiley and Sons Inc., 2004a.

Levanon, N., and E. Mozeson, Modified Costas Signal, *IEEE Transactions on Aerospace and Electronic Systems*, *40*(3), 946–953, 2004b.

Lind, F. D., Passive Radar Observations of the Aurora, Ph.D. thesis, University of Washington, 1999.

Mann, I., et al., The Upgraded CARISMA Magnetometer Array in the THEMIS Era, *Space Science Reviews*, *141*, 413–451, 2008.

McDiarmid, D., On the Aspect Sensitivity of Radio Aurora, *Canadian Journal of Physics*, *50*, 2557, 1972.

McDiarmid, D., and A. MacNamara, VHF radio aurora: simultaneous observation of auroral ionization by two separated radars, *Canadian Journal of Physics*, *45*, 3009–3027, 1967.

Meyer, M., Discussion of the Manastash Ridge Radar Project, http://rrsl.ee.washington.edu/research.htm, 2003.

Moorcroft, D., An examination of radio-auroral aspect sensitivity, *Canadian Journal of Physics*, *63*, 1005–1012, 1984.

Moorcroft, D., Reflection and refraction by titled layers: An explanation for VHF Auroral backscatter at large aspect angles, *Geophysical Research Letters*, *16*(3), 235–238, 1989.

Moorcroft, D., Outstanding issues in the theory of radar aurora: Evidence from the frequency dependence of spectral characteristics, *Journal of Geophysical Research*, *107*(A10), 1301–1309, 2002.

Mu, J., VHF Radar Aurora: Statistics Fading and Correlation with Optical Aurora, Ph.D. thesis, University of Saskatchewan, 1997.

NORSTAR, http://aurora.phys.ucalgary.ca/norstar/index.html, 2005.

Ortlepp, A., *SAPPHIRE VHF radar system manual*, Institute of Space and Atmospheric Studies, University of Saskatchewan, 1994.

Petsios, M. N., E. G. Alivizatos, and N. K. Uzunoglu, Solving the association problem for a multistatic range-only radar target tracker, *Signal Process.*, *88*(9), 2254–2277, doi:http://dx.doi.org/10.1016/j.sigpro.2008.03.011, 2008.

Rickard, S., E. Connell, F. Duigan, B. Ladendorf, and A. Wade, The enumeration of Costas arrays of size 26, 2006.

Rihaczek, A. W., *Principles of High-Resolution Radar*, McGraw-Hill Book Company, 1969.

Sahr, J., D. Farley, W. Swartz, and J. Providakes, The Altitude of Type 3 Auroral Irregularities: Radar Interferometer Observations and Implications, *Journal of Geophysical Research*, *96*(A10), 17,805–17,811, 1991.

Sahr, J. D., and B. G. Fejer, Auroral electrojet plasma irregularity theory and experiment: A critical review of present understanding and future directions, *Journal of Geophysical Research*, *101*(A12), 26,893–26,909, 1996.

Schlegel, K., Coherent backscatter from ionospheric E-region plasma irregularities, *Journal of Atmospheric and Terrestrial Physics*, *58*(8/9), 933–941, 1996.

Six, M., J.Parent, A. Bourdillon, and J. Delloue, A New Multibeam Receiving Equipment for the Valensole Skywave HF Radar: Description and Applications, *IEEE Transactions on Geoscience and Remote Sensing*, *34*(3), 708–719, 1996.

Skolnik, M. I., *Introduction to Radar Systems*, Second ed., McGraw-Hill Book Company, 1980.

Skolnik, M. I. (Ed.), *Radar Handbook*, Second ed., McGraw-Hill Publishing Company, 1990.

Stove, A., Linear FMCW radar techniques, *IEEE Proceedings-F*, *139*(5), 343–350, 1992.

Sudan, R., J. Akinrimisi, and D. Farley, Generation of small-scale irregularities in the equatorial electrojet, *Journal of Geophysical Research*, *78*, 240–248, 1973.

Vecima, Vecima Networks Inc., http://www.vecima.com.

Wannberg, G., et al., The EISCAT Svalbard radar: A case study in modern incoherent scatter radar system design, *Radio Science*, *32*(6), 2283–2307, 1997.

Watt, T., L. Newkirk, and E. Shelley, Joint radar-satellite determination of the effective recombination coefficient in the auroral E region, *Journal of Geophysical Research*, *79*, 4725, 1974.

Appendix A

Costas Arrays

Table A.1 describes the number of Costas arrays that exist for an order M [*Levanon and Mozeson*, 2004a; *Drakakis et al.*, 2008; *Rickard et al.*, 2006]. A plot of the number of Costas arrays that exist as a function of order, M is given in Figure A.1. Here, the overall shape of the plot is symmetric and resembles a Gaussian with a peak at order M = 16. The shape of the graph has led researchers to question whether Costas array exists for all M and research regarding this question is on going.

Table A.1: Number of Costas arrays [*Levanon and Mozeson*, 2004a; *Drakakis et al.*, 2008; *Rickard et al.*, 2006].

Order M	Number of Costas arrays
1	1
2	2
3	4
4	12
5	40
6	116
7	200
8	444
9	760
10	2160
11	4368
12	7852
13	12828
14	17252
15	19612
16	21104
17	18276
18	15096
19	10240
20	6464
21	3536
22	2052
23	872
24	200
25	88
26	56
27	204

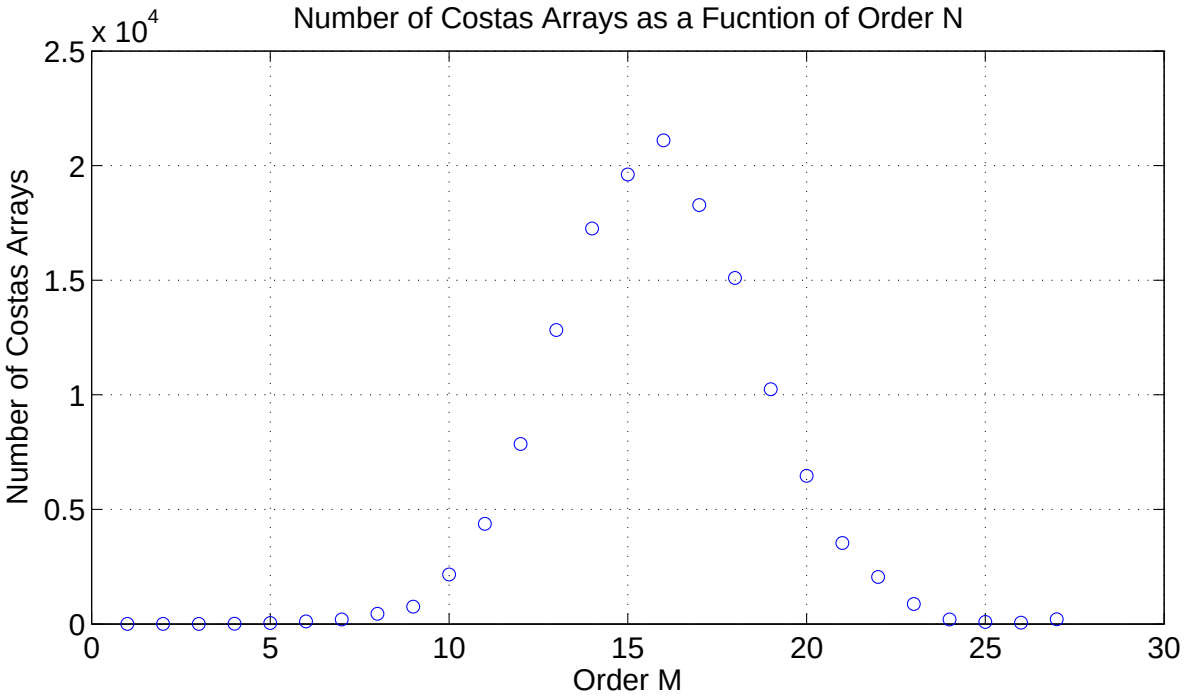

Figure A.1: Number of Costas Arrays as a function of order M [*Levanon and Mozeson*, 2004a; *Drakakis et al.*, 2008; *Rickard et al.*, 2006].

Appendix B

AWG5000B Series Data Sheet

Arbitrary Waveform Generators

AWG5000B Series Data Sheet

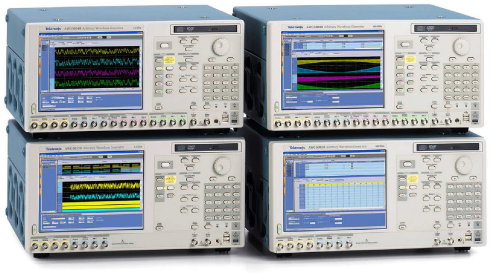

AWG5000B Series

Features & Benefits

- 370 MHz Effective RF Frequency Output
- 1.2 GS/s and 600 MS/s Models
- 14-bit Vertical Resolution
- 2 or 4 Arbitrary Waveform Differential/Single-ended Outputs
  - Up to 4.5 $V_{pk\text{-}pk}$ Single-ended and 9 $V_{pk\text{-}pk}$ at Differential Output into 50 Ω
  - 0.95 ns Tr/Tf (10 - 90%) at 0.6 $V_{pk\text{-}pk}$
  - ±5 ns Range (50 ps Resolution) Interchannel Skew Control
  - SFDR: 80 dBc (1 MHz), 64 dBc (10 MHz)
- 4 or 8 Variable Level Marker Outputs
  - Up to 3.7 $V_{pk\text{-}pk}$ Single-ended Output into 50 Ω
  - 300 ps Tr/Tf (20 - 80%) at 0 to 1 V
  - Up to 1 ns Range (50 ps Resolution) Delay Control
- 28-bit CH1/CH2 Variable-level Digital Data Output
  - Up to 3.7 $V_{pk\text{-}pk}$ Single-ended Output into 50 Ω
  - 300 ps Tr/Tf (20 - 80%) at 0 to 1 V
- Up to 32 Mpoint Record Length For Longer Data Streams
- Down to 800 ps Resolution Edge Timing Shift Control
- 8,000 Steps Real-time Sequencing Creates Infinite Waveform Loops, Jumps, and Conditional Branches
- Easy to Use and Learn, Shortens Test Time
- Intuitive User Interface Based on Windows XP
- Convenient Benchtop Form Factor
- Integrated PC Supports Network Integration and Provides a Built-in DVD, Removable Hard Drive, LAN, and USB Ports

Applications

- Designing, Testing, and Deploying
- Wireless Communications:
  - High-fidelity Quadrature Modulation I&Q Baseband Signals (Polar Modulation: I/Q + Magnitude Control, Two Pair of I/Q for MIMO)
- Imaging
  - Stimulus Signals for Imaging Display and Recording Devices (CCD, LCD)
- Data Conversion
  - Stimulus Signals for Data Conversion Devices (ADC, DAC)
- Mixed-signal Design and Test
  - 2/4 ch Analog + 4/8 ch Marker Outputs + 28 bit Digital Data Outputs
- Real-world, Ideal, or Distorted Signal Generation – Including all the Glitches, Anomalies, and Impairments
- Enhanced/Corrupted Playback of DSO Captured Signals
- Waveform Vectors Imported from Third-party Tools such as MathCAD, MATLAB, Excel, and Others

Tektronix®

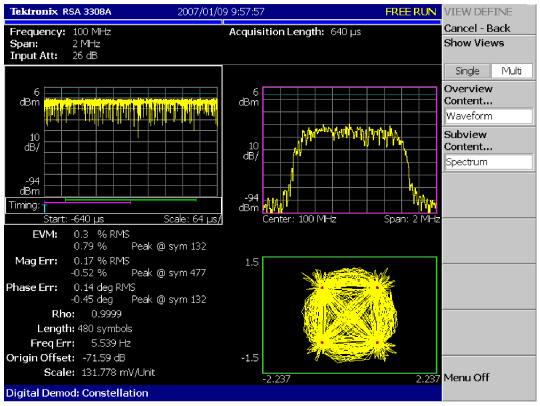

EVM/Constellation Measurement

Industry's Best Mixed-signal Stimulus Solution for Today's Complex Measurement Challenges

The AWG5000B Series of Arbitrary Waveform Generators delivers the optimal combination of industry leading sample rate, vertical resolution, signal fidelity, and waveform memory length, all in an easy-to-use self-contained package. The series offers the industry's best solution to the challenging signal stimulus issues faced by designers verifying, characterizing, and debugging sophisticated electronic designs.

Meeting the needs of today's design engineers, the series provides excellent signal dynamic range and integrity. AWG5000B Series models, with a 14 bit DA-converter-based sample rate from 600 MS/s to 1.2 GS/s, 2 to 4 output channels, synchronized 4 to 8 digital marker outputs, and 28 channels of digital data outputs, easily solve the toughest measurement challenges in wireless baseband I/Q communications, digital consumer product design such as imaging devices, data conversion equipment, and semiconductor design and test.

The open windows (Windows XP) based instruments are easy and convenient to use and connect easily with peripherals and third-party software.

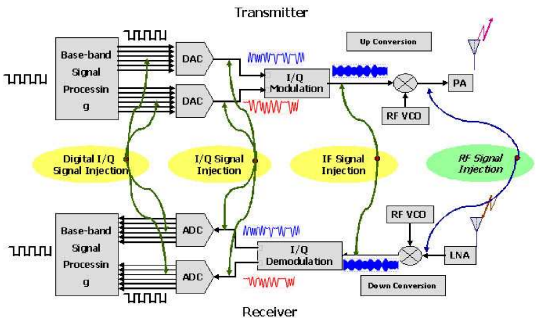

Typical Signal Injection

Wireless I/Q and IF Signal Generation

Tektronix AWGs support "Wireless Everywhere" by enabling the latest Digital RF technology, increasing wireless network capacity, and delivering the performance that supports higher modulation bandwidth and modulation schemes.

The AWG5000B Series addresses narrowband IQ to broadband IF applications with up to 1.2 GS/s, 14-bit resolution, and sufficient SFDR. The AWG5000B is able to generate not only analog IQ/IF signals, but digital data IQ/IF. The MIMO (Multiple Input Multiple Output) system that supports W-LAN/Wi-Max using space multiplex with multiple antennas is a leading-edge technology for reliable and faster data rate communication. The AWG5000B Series generates up to 4 analog channels (8 channels through two instruments) to simultaneously generate MIMO signals. The series can generate two pairs of IQ signals (4 pairs with two instruments) as an IQ generator, and four pairs of IF signals (8 pairs with two instruments) as an IF generator. With the two channel models, CH1 and CH2, digital data output is available as an option.

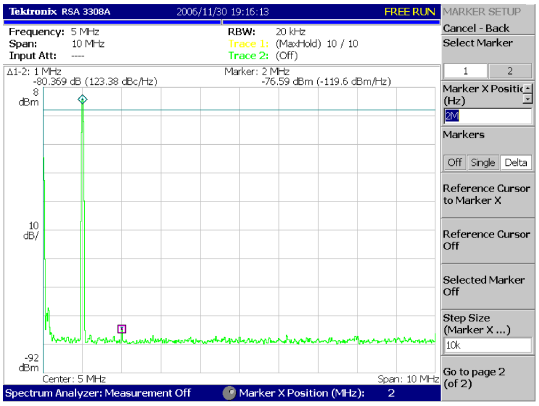

RTSA Spectrum view

Spurious Performance

The 14-bit vertical resolution and sophisticated design of the AWG5000B Series provides ample signal dynamic range and purity. The SFDR performance is 80 dBc for 1 MHz signal and 64 dBc for 10 MHz signal.

Multilevel Logic Signal

One technique to increase the data rate without increasing the transition rate is applying multilevel signals, wherein a signal can assume more than the standard binary 2 levels. In multilevel signaling, one can think of multilevel discrete amplitudes of a signal. This phenomenon is known as Pulse Amplitude Modulation or PAM. A 9-PAM signal, a signal with 9 different amplitudes, increases the data rate by four without increasing the transition rate of the signal.

The AWG5000B Series enables you to test your latest design by generating any kind of mixed or multilevel signal.

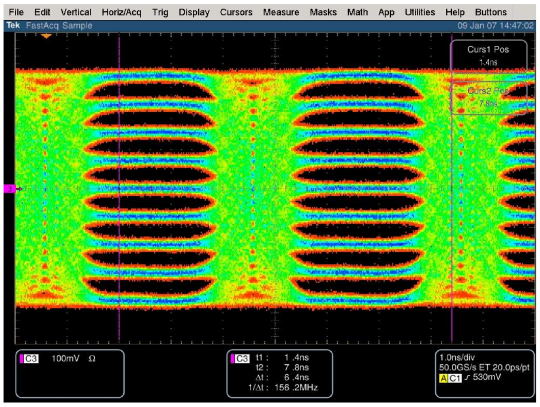

9-PAM with 250 Mb/s

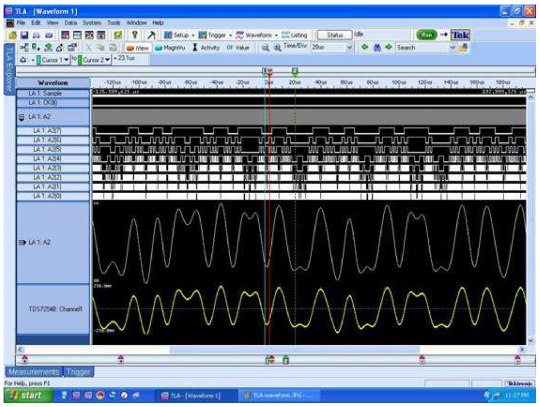

Mixed-signal test by TDS/TLA iView

Mixed-signal Generation

AWG5012B and AWG5002B models can generate two analog signals with four digital marker outputs, supporting 28 digital outputs (CH1 and CH2 data) as an option. They deliver a mixed analog and digital signal generator and the most versatile solution for a broad range of applications, including consumer electronics such as ADC/DAC converter and imaging or display devices.

Additional Software Application Tools to Extend Waveform Generation

RFXpress® (RFX100)

RFXpress® is a software package that synthesizes digitally modulated baseband IQ and IF signals. It takes IQ and IF signal generation to the next level and fully exploits the wideband signal generation capabilities of Arbitrary Waveform Generators (AWGs). Supporting a wide range of modulations, as well as the symbol map functions, the software allows you to define your own modulation.

SPARA is an option for RFXpress that provides emulation of RF components from touchstone files. You can cascade multiple touchstone files to emulate a RF chain. The effect of the RF component can also be de-embedded by selecting the Inversion option.

Radar Signal Creation is a software module for RFXpress that gives you the ultimate flexibility in creating Pulsed Radar waveforms. It gives you the ability to build your own Radar Pulse suite starting from pulse-to-pulse trains to pulse groups. It supports a variety of modulation schemes including LFM, Barker and Polyphase Codes, User-defined Codes, Step FM, Nonlinear FM, User-defined FM, and Custom modulation. It also has the ability to generate pulse trains with staggered PRI to resolve Range and Doppler ambiguity, frequency hopping for Electronic Counter-Counter Measures (ECCM), and pulse-to-pulse amplitude variation to simulate Swerling target models including antenna scan patterns and multipath effects.

RFXpress is a powerful easy-to-use software package to synthesize IQ and IF signals for Arbitrary Waveform Generators (AWG). It runs as an integral part of the AWG5000B Series arbitrary waveform generators or from an external PC.

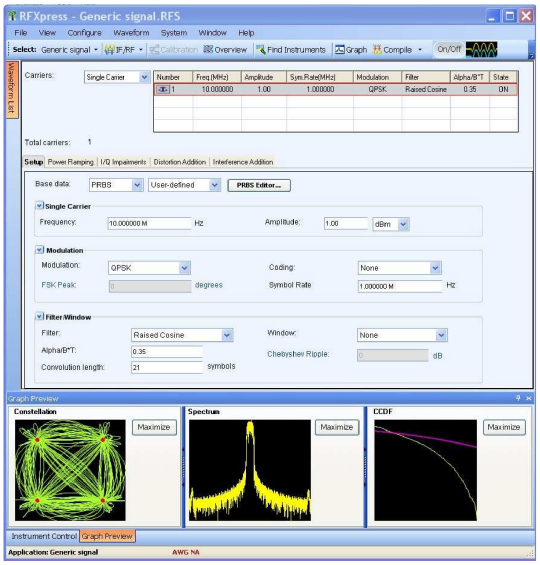

Characteristics

Arbitrary Waveform Output

Characteristic	AWG5014B	AWG5012B	AWG5004B	AWG5002B
Digital-to-Analog Converter				
Resolution	14 bit			
Number of Outputs	4	2	4	2
Output Type	Differential			
Output Impedance	50 Ω			
Output Connector Type	BNC (front panel)			
Sampling Rate	10 MS/s to 1.2 GS/s		10 to 600 MS/s	
Frequency				
Effective RF Frequency (Fmax)	Fmax determined as the lower of "Effective bandwidth (-6 dB)" or "Max sampling rate / 2.5 points per cycle"			
(Typical)	370 MHz		240 MHz	
Effective Freq Switching Time	Minimum frequency switching time (from selected frequencies F_1 to F_2) is determined as "1 / Fmax"			
Standard (typical)	400 ns		800 ns	
Option 08 (typical)	2.7 ns		4.2 ns	
Sinewave	1.2 GS/s clock, 32 points per waveform 37.50 MHz carrier frequency, 1.0 V_{pk-pk}		0.6 GS/s clock, 32 points per waveform 18.75 MHz carrier frequency, 1.0 V_{pk-pk}	
Amplitude				
Rise Time Bandwidth (-3 dB)	Analog bandwidth converted from rise time characteristics through analog output and filtering circuitry			
(typical)	Normal: 250 MHz Direct: 370 MHz			
Low Pass Filter	Normal: 20 MHz, 100 MHz (Bessel type) Direct: N/A			
Amplitude				
Range	Normal: 20 mV to 4.5 V_{pk-pk} Direct: 20 mV to 0.6 V_{pk-pk}			
Resolution	1 mV			
Accuracy	±(2.0% of amplitude ±2 mV) at offset = 0 V			
Offset				
Range	Normal: -2.25 V to +2.25 V Direct: N/A			
Resolution	1 mV			
Accuracy	±(2% of offset ±10 mV) at minimum amplitude			
Distortion				
Harmonic Distortion	Normal: ≤ -40 dBc Direct: ≤ -49 dBc		Normal: ≤ -46 dBc Direct: ≤ -55 dBc	
Nonharmonic Spurious	≤ -60 dBc (DC to 600 MHz)		≤ -60 dBc (DC to 300 MHz)	
Spurious Free Dynamic Range	1.2 GS/s clock, Amplitude: 1 V_{pk-pk}, Offset: 0 V 14 bit DAC operational mode, DC to 600 MHz		0.6 GS/s clock, Amplitude: 1 V_{pk-pk}, Offset: 0 V 14 bit DAC operational mode, DC to 300 MHz	
(Typical)	50 dBc (Normal: 37.5 MHz, 1.2 GS/s, 2.0 V_{pk-pk}) 60 dBc (Normal: 10 MHz, 600 MS/s, 1.0 V_{pk-pk}) 80 dBc (Normal: 1 MHz, 600 MS/s, 1.0 V_{pk-pk}) 64 dBc (Direct: 10 MHz, 600 MS/s, 0.6 V_{pk-pk}) 80 dBc (Direct: 1 MHz, 600 MS/s, 0.6 V_{pk-pk})		56 dBc (Normal: 18.75 MHz, 600 MS/s, 2.0 V_{pk-pk}) 60 dBc (Normal: 10 MHz, 600 MS/s, 1.0 V_{pk-pk}) 80 dBc (Normal: 1 MHz, 600 MS/s, 1.0 V_{pk-pk}) 64 dBc (Direct: 10 MHz, 600 MS/s, 0.6 V_{pk-pk}) 80 dBc (Direct: 1 MHz, 600 MS/s, 0.6 V_{pk-pk})	
Phase Noise	1.2 GS/s clock, Amplitude: 1 V_{pk-pk}, Offset: 0 V Carrier Frequency: 37.50 MHz		0.6 GS/s clock, Amplitude: 1 V_{pk-pk}, Offset: 0 V Carrier Frequency: 18.75 MHz	
(typical)	≤ -85 dBc/Hz at 10 kHz offset			
Random Jitter	1010 clock pattern			
RMS (typical)	Normal: 5 ps			
Total Jitter	2^{-15} - 1 PN data pattern (at 10^{-12} BER)			
Peak-to-Peak (typical)	Normal: 150 ps			
Pulse				
Pulse Response				
Rise/Fall Time (10 to 90%)	Normal: 1.4 ns (at 2.0 V_{pk-pk}) Direct: 0.95 ns (at 0.6 V_{pk-pk})			
Overshoot	Less than 10% (at 0.6 V_{pk-pk})			

Characteristic	AWG5014B	AWG5012B	AWG5004B	AWG5002B
Arbitrary Waveforms				
Waveform Length	1 to 16,200,000 points (or 1 to 32,400,000 points, Option 01)			
Number of Waveforms	1 to 16,000			
Sequence Length	1 to 8,000 steps total			
Sequence Repeat Counter	1 to 65,536 or infinite			
Sequence Control	Repeat count, Wait for Trigger, Go-to-N and Jump The standard model requires “wait for trigger ON” for all sequence step definition, the Option 08 (fast sequence switching) selectable On or Off for each sequence step.			
Jump Mode	Synchronous and Asynchronous			
Run Modes				
Continuous	Waveform is iteratively output. If a sequence is defined, the sequence order and repeat functions are applied			
Triggered	Waveform is output only once when an external, internal, GPIB, LAN, or manual trigger is received			
Gated	Waveform begins output when gate is true and resets to beginning when false			
Sequence	Waveform is output as defined by the sequence			
Sampling Clock				
Resolution	8 digits			
Internal Clock				
Accuracy	Within ±(1 ppm + Aging) Aging: within ±1 ppm/year			
Internal Trigger Generator				
Internal Trigger Rate				
Range	1.0 µs to 10.0 s			
Resolution	3 digits, 0.1 µs minimum			
Skew Control Between Outputs				
Range	-5 ns to +5 ns			
Resolution	5 ps			

Auxiliary Outputs

Characteristic	AWG5014B	AWG5012B	AWG5004B	AWG5002B
Marker Output				
Number of Outputs	8 (2 per ch)	4 (2 per ch)	8 (2 per ch)	4 (2 per ch)
Output Style	Single Ended			
Output Impedance	50 Ω			
Connector	BNC Front			
Level (into 50 Ω) (Twice for Hi_Z input)				
Output Windows	-1.00 V to +2.7 V			
Amplitude	0.10 V_{pk-pk} to 3.7 V_{pk-pk}			
Resolution	10 mV			
DC Accuracy	±(10% of setting +120 mV)			
Maximum Output Current	±54 mA/ch			
Rise/Fall Time (20% to 80%)	300 ps (1.0 V_{pk-pk}, Hi: +1.0 V, Low: 0 V)			
Skew Adjust Between Markers				
Range	0 to 1000 ps			
Resolution	50 ps			
Random Jitter (Typical)	1010 clock pattern			
RMS (Typical)	5 ps_{RMS}			
Total Jitter	2^{15} - 1 PN data pattern			
Peak-to-Peak (pk-pk) (Typical)	80 ps_{pk-pk}			
Clock (VCO) Out				
Range	600 MHz to 1.2 GHz			
Amplitude	0.4 V_{pk-pk} into 50 Ω to GND			
Impedance	50 Ω, AC coupling			
Connector	BNC Rear			
10 MHz Reference Out				
Amplitude	1.2 V_{pk-pk} into 50 Ω. Max 2.5 V_{pk-pk} open			
Impedance	50 Ω, AC coupling			
Connector	BNC Rear			
DC Outputs				
Number of Outputs	4: independently controlled outputs			
Range	-3.0 to +5.0 V			
Resolution	10 mV			
Output Voltage Accuracy	±(3% of the setting + 120 mV)			
Max Current	±100 mA			
Connector	2×4 pin header on front panel			
Digital Data Output (Option 03)				
Number of Output	NA	14 bit output on channel 1 and channel 2 (28 total)	NA	14 bit output on channel 1 and channel 2 (28 total)
Output Style		Single ended		Single ended
Output Impedance		50 Ω		50 Ω
Connector		SMB rear		SMB rear
Level (into 50 Ω) (Twice for Hi_Z Input)				
Output Windows		-1.00 V to +2.7 V		-1.00 V to +2.7 V
Amplitude		0.10 V_{pk-pk} to 3.7 V_{pk-pk}		0.10 V_{pk-pk} to 3.7 V_{pk-pk}
Resolution		10 mV		10 mV
DC Accuracy		±(10% of setting +120 mV)		±(10% of setting +120 mV)
Maximum Output Current		±54 mA/ch		±54 mA/ch
Rise/Fall Time (20% to 80%)		300 ps (1.0 V_{pk-pk}, Hi: +1.0 V, Low: 0 V)		300 ps (1.0 V_{pk-pk}, Hi: +1.0 V, Low: 0 V)
Delay from Marker		-41 ns to -82 ns		-41 ns to -82 ns
Skew Between Digital Outputs		Less than 400 ps		Less than 400 ps

Auxiliary Inputs

Characteristic	AWG5014B/AWG5012B	AWG5004B/AWG5002B
Trigger In		
Impedance	1 kΩ or 50 Ω	
Polarity	POS or NEG	
Connector	BNC Front	
Input Voltage Range	1 kΩ: ±10 V 50 Ω: ±5 V	
Threshold		
Level	-5.0 V to 5.0 V	
Resolution	0.1 V	
Trigger Jitter	2.0 ns to 4.5 ns (Typical)	
Asynchronies Between Internal/External Clock and Trigger Timing (Typical)	2.0 ns to 4.5 ns	
Trigger Mode		
Minimum Pulse Width	20 ns	
Trigger Holdoff	160 * sampling_period - 200 ns	
Delay to Analog Out	48 * sampling_period + 500 ns	
Gate Mode		
Minimum Pulse Width	1024 * sampling_period + 10 ns	
Delay to Analog Out	240 * sampling_period + 500 ns	
Event Input		
Impedance	1 kΩ or 50 Ω	
Polarity	POS or NEG	
Connector	BNC Front	
Input Voltage Range	1 kΩ: ±10 V 50 Ω: ±5 V	
Threshold	-5.0 V to 5.0 V	
Resolution	0.1 V	
Sequence Mode		
Minimum Pulse Width	20 ns	
Event Hold Off	200 * Sampling Period + 500 ns (Jump timing: Asynchronous jump)	
Delay to Analog Out	260 * Sampling Period + 300 ns	
External Clock IN		
Input Voltage Range	0.2 V_{pk-pk} to 0.8 V_{pk-pk}	
Impedance	50 Ω, AC coupled	
Frequency Range	600 MHz to 1.2 GHz	
Clock Divider	1/1, 1/2, 1/4.....1/32	1/2, 1/4.....1/32
Connector	BNC Rear	
Reference Clock IN		
Input Voltage Range	0.2 V_{pk-pk} to 3.0 V_{pk-pk}	
Impedance	50 Ω, AC coupled	
Frequency Range	10 MHz, 20 MHz, 100 MHz (with ±0.5%)	
Connector	BNC Rear	
Phase Lock IN		
Input Ranges	5 MHz to 600 MHz (acceptable frequency drift is ±0.5%)	
Input Voltage Range	0.2 V_{pk-pk} to 3 V_{pk-pk}	
Impedance	50 Ω, AC coupled	
Multiple Rate	1 to 240	1 to 120
Connector	BNC Rear	
Add IN	For each analog channel	
Impedance	50 Ω, DC coupled	
DC Gain	1	
Bandwidth	DC to 100 MHz at -3 dB	
Input Voltage Range	±1.0 V	
Connector	BNC Rear	

AWG5000B Series Common Features

Characteristic	Description
Waveform File Import Capability	Tektronix TDS5000/6000/7000, DPO4000/7000/70000, DSA70000 (*.wfm). TDS3000 (*.wfm) AWG400s/500s/610/615/710/710B (*.wfm, *.pat, *.seq), DTG5000s (*.DAT) Text data file (third-party software creation waveform data: MATLAB, MathCad, Excel)
S/W Driver for Third-party S/W	IVI-com driver and MATLAB library
Instrument Control / Data Transfer Ports	
GPIB	Remote control and data transfer. (Conforms to IEEE-Std 488.1, compatible with IEEE 488.2 and SCPI-1999.0).
Ethernet (10/100/1000Base-T)	Remote control and data transfer. (Conforms to IEEE 802.3). RJ-45
Computer System and Peripherals	Windows XP Professional, 2 GB SDRAM, 80 GB removable Hard Drive at rear (available front mount kit), CD-RW/DVD drive at front, included USB compact keyboard and mouse
PC I/O Ports	USB 2.0 compliant ports (6 total, 2 front, 4 rear), PS/2 mouse and keyboard connectors (rear panel), RJ-45 Ethernet connector (rear panel) supports 10/100/1000 BASE-T, XGA out
Display	10.4 inch, LCD color display with touch screen, 1024 (H) × 768 (V) (XGA).
Power Supply	100 to 240 VAC, 47 to 63 Hz
Power Consumption	450 W
Safety	UL61010-1, CAN/CSA-22.2, No.61010-1-04, EN61010-1, IEC61010-1
Emissions	EN 55011 (Class A), IEC61000-3-2, IEC61000-3-3
Immunity	IEC61326, IEC61000-4-2/3/4/5/6/8/11
Regional Certifications	
Europe	EN61326
Australia / New Zealand	AS/NZS 2064

Physical Characteristics

Dimension	mm	in.
Height	245	9.6
Width	465	18.0
Length	500	19.7
Weight (approx.)	**kg**	**lb.**
Net	19.5	43.0
Net with Package	28.5	62.8
Mechanical Cooling		
Required Clearance	**cm**	**in**
Top and Bottom	2	0.8
Side	15	6
Rear	7.5	3

Environmental

Characteristic	Operating	Nonoperating
Temperature	+10° C to +40° C	-20° C to +60° C
Humidity	5% to 80% relative humidity (% RH) at up to +30° C, 5% to 45% RH above +30° C up to +50° C,	5% to 90% RH (Relative Humidity) at up to +30° C, 5% to 45% RH above +30° C up to +50° C,
Altitude	Up to 3,048 meters (10,000 feet)	Up to 12,192 meters (40,000 feet)
Random Vibration	0.27 G_{RMS}, 5 to 500 Hz, 10 minutes per axis	2.28 G_{RMS}, 5 to 500 Hz, 10 minutes per axis
Sine Vibration	0.33 $mm_{pk\text{-}pk}$ (0.013 $inch_{pk\text{-}pk}$) constant displacement, 5 to 55 Hz	NA
Mechanical Shock	Half-sine mechanical shocks, 30 g peak amplitude, 11 ms duration, 3 drops in each direction of each axis	NA

Ordering Information

Arbitrary Waveform Generator Mainframe

AWG5014B
1.2 GS/s, 14-bit resolution, 16 Mpoint per channel, 4-channel arbitrary waveform generator

AWG5012B
1.2 GS/s, 14-bit resolution, 16 Mpoint per channel, 2-channel arbitrary waveform generator

AWG5004B
600 MS/s, 14-bit resolution, 16 Mpoint per channel, 4-channel arbitrary waveform generator

AWG5002B
600 MS/s, 14-bit resolution, 16 Mpoint per channel, 2-channel arbitrary waveform generator

All Models Include: Accessory pouch, front cover, USB mouse, compact USB keyboard, lead set for DC output, stylus for touch screen (2 ea), AWG5000B Series product software CD and instructions, documentation CD with browser, Quick Start User Manual and registration card, Certificate of Calibration, and power cable.
Note: Please specify power cord and language option when ordering.

Instrument Options

Option	Description
AWG5014B/AWG5012B/AWG5004B/AWG5002B	
Opt. 01	Waveform Length Expansion (from 16 M to 32 M)
Opt. 08	Fast sequence switching (requires export control license) ECCN:3A002
AWG5012B/AWG5002B	
Opt. 03	28 bit digital data outputs (digital data of CH1 and CH2)
AWG5012B	
Opt. 09	Subsequencing and table jump functionality (includes LVDS to TTL TekLink Connector Adapter)

Common Options

Note: Please specify power cord and language option at time of order.

International Power Plugs

Option	Description
Opt. A0	North America
Opt. A1	Universal EURO
Opt. A2	United Kingdom
Opt. A3	Australia
Opt. A5	Switzerland
Opt. A6	Japan
Opt. A10	China
Opt. A11	India
Opt. A99	No power cord or AC adapter

Language Options

Option	Description
Opt. L0	English
Opt. L5	Japanese
Opt. L7	Simplified Chinese
Opt. L8	Traditional Chinese
Opt. L10	Russian

Application Software

Model	Option	Description
RFX100		General-purpose IQ, IF, and RF Signal Creation Software Package
	Opt. UWBCF	RFXpress plug-in for UWB-WiMedia IQ, IF, and RF conformance signal creation (requires RFX100 as prerequisite)
	Opt. UWBCT	RFXpress plug-in for UWB-WiMedia IQ, IF, and RF custom and conformance signal creation (requires RFX100 as prerequisite and includes Opt. UWBCF)
	Opt. RDR	RFXpress plug-in for Radar signal creation (requires RFX100 as prerequisite)
	Opt. SPARA	S-Parameter emulation and DUT characterization (requires RFX100 as prerequisite)
SDX100		Jitter Generation Software Package (includes USB dongle)
	Opt. ISI	S-Parameter and ISI creation (requires SDX100 as prerequisite)
	Opt. SSC	Spread Spectrum Clock addition option (requires SDX100 as prerequisite)

Service Options

Option	Description
Opt. CA1	A single calibration event
Opt. C3	Calibration service 3 years
Opt. C5	Calibration service 5 years
Opt. D1	Calibration data report
Opt. D3	Calibration data report 3 years (with Opt. C3)
Opt. D5	Calibration data report 5 years (with Opt. C5)
Opt. R3	Repair service 3 years
Opt. R5	Repair service 5 years
Post-sales Service Options: (e.g. AWG5012-CA1)	
CA1	A single calibration event
R3DW	Repair service coverage 3 years
R5DW	Repair service coverage 5 years
R2PW	Repair service coverage 2 years post-warranty
R1PW	Repair service coverage 1 year post-warranty

Product Upgrade

Product	Options to Upgrade		Description
AWG5014B	AWG50BUP	Opt. M14	Waveform Length Expansion from 16 Mpoint to 32 Mpoint
		Opt. S48	Upgrade from standard to Option 08 (fast sequence switching) requires export license
AWG5012B	AWG50BUP	Opt. M12	Waveform Length Expansion from 16 Mpoint to 32 Mpoint
		Opt. D13	Digital Data Outputs
		Opt. S38	Upgrade from Standard to Option 08 (fast sequence switching) requires export license
		Opt. S09	Upgrade from Standard to Option 09 (Subsequencing and table jump functionality, includes LVDS to TTL TekLink Connector Adapter)
AWG5004B	AWG50BUP	Opt. M04	Waveform Length Expansion from 16 Mpoint to 32 Mpoint
		Opt. S28	Upgrade from Standard to Option 08 (fast sequence switching) requires export license
AWG5002B	AWG50BUP	Opt. M02	Waveform Length Expansion from 16 Mpoint to 32 Mpoint
		Opt. D03	Digital Data Outputs
		Opt. S18	Upgrade from Standard to Option 08 (fast sequence switching) requires export license

Recommended Accessories

Item	Description	Part Number
Pin Header Cable		
SMA Cable	102 cm (40 inch)	012-1690-xx
SMB Cable	51 cm (20 inch)	012-1503-xx
Rackmount Kit	Rackmount Kit with instruction	016-1983-xx
Front Removable HDD Bay	Front Removable HDD Bay	016-1979-xx
Replacement Hard Disk for AWG5000/7000 Series	SATA disk assembly (no software installation), instruction sheet	065-0811-xx
Quick Start User Manual	English	071-2481-xx
	Japanese	071-2482-xx
	Simplified Chinese	071-2483-xx
	Traditional Chinese	071-2484-xx
	Russian	020-2971-xx
Programmer Manual	English	077-0061-xx
Option 09 User Manual	English	071-2674-xx
Service Manual	English	Visit Tektronix website

Warranty

One-year parts and labor.

CE

ISO 9001 Product(s) are manufactured in ISO registered facilities.

GPIB IEEE-488 Product(s) complies with IEEE Standard 488.1-1987, RS-232-C, and with Tektronix Standard Codes and Formats.

Data Sheet

Contact Tektronix:

ASEAN / Australasia (65) 6356 3900

Austria +41 52 675 3777

Balkans, Israel, South Africa and other ISE Countries +41 52 675 3777

Belgium 07 81 60166

Brazil +55 (11) 40669400

Canada 1 (800) 661-5625

Central East Europe, Ukraine, and the Baltics +41 52 675 3777

Central Europe & Greece +41 52 675 3777

Denmark +45 80 88 1401

Finland +41 52 675 3777

France +33 (0) 1 69 86 81 81

Germany +49 (221) 94 77 400

Hong Kong (852) 2585-6688

India (91) 80-42922600

Italy +39 (02) 25086 1

Japan 81 (3) 6714-3010

Luxembourg +44 (0) 1344 392400

Mexico, Central/South America & Caribbean 52 (55) 54247900

Middle East, Asia, and North Africa +41 52 675 3777

The Netherlands 090 02 021797

Norway 800 16098

People's Republic of China 86 (10) 6235 1230

Poland +41 52 675 3777

Portugal 80 08 12370

Republic of Korea 82 (2) 6917-5000

Russia & CIS +7 (495) 7484900

South Africa +27 11 206 8360

Spain (+34) 901 988 054

Sweden 020 08 80371

Switzerland +41 52 675 3777

Taiwan 886 (2) 2722-9622

United Kingdom & Ireland +44 (0) 1344 392400

USA 1 (800) 426-2200

For other areas contact Tektronix, Inc at: 1 (503) 627-7111

Updated 30 October 2008

For Further Information. Tektronix maintains a comprehensive, constantly expanding collection of application notes, technical briefs and other resources to help engineers working on the cutting edge of technology. Please visit **www.tektronix.com**

15 Jul 2009 76W-22260-4

www.tektronix.com/awg5000